

https://dspace.org/

A model of the argon oxygen decarburization process for refining stainless steel and alloys

Burrow, Andrew Charles

2015-01-12
http://hdl.handle.net/10539/16476

Downloaded from a DSpace repository. https://dspace.org/

A MODEL OF THE ARGON OXYGEN DECARBURIZATION PROCESS FOR REFINING STAINLESS STEEL AT MIDDELBURG STEEL AND ALLOYS

Andrew Charles Burrow

Degree of Master of Science in Engineering by research only:

'A dissertation submitted to the Faculty of Engineering, University of the Witwatersrand, Johannesburg, in fulfilment of the requirements for the degree of Master of Science in Engineering.'

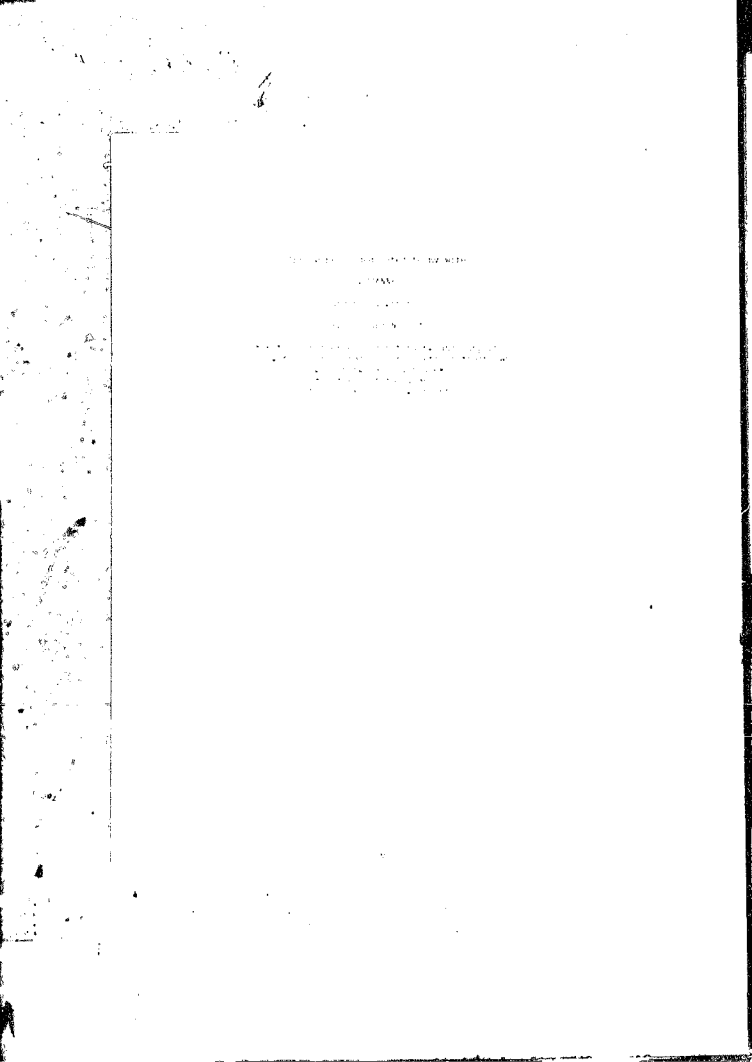
Middelburg, 1988

DECLARATION

I declare that this dissertation is my own, unaided work. It is being submitted for the Degree of Master of Science in Engineering in the University of the Witwatersrand, Johannesburg. It has not been submitted before for any degree or examination in any other University.

(Signature of candidate)

2nd day of November 1988



This work is dedicated to my wife

SUZANNE

and my daughters

JESSICA and NICOLA

for their patience, understanding and support
during those innumerable hours spent on their own
during evenings and over weekends
for the last two years
while this work was being undertaken

ACKNOWLEDGEMENTS

The support and assistance of the following are gratefully acknowledged, for without them this work would not have been possible:-

(i) Middelburg Steel and Alloys for permission to undertake and publish this study;

(ii) Middelburg Steel and Alloys for their encouragement and support in the provision of the computer and other facilities essential for the development of this work;

(iii) Middelburg Steel and Alloys for the opportunity of getting first hand experience of the AOD process and to use the production unit to obtain actual plant data in conjunction with C Pauw and U Meyn of MINTEK;

(iv) Messers C Pauw, U Meyn and Dr. I Barker of MINTEK for their discussions and advice. Also for supplying copies of some of the papers referred to in the literature survey;

(v) Prof. R P King for his advice and assistance in finding a suitable integrator routine.

CONTENTS

		Page
DECLARATION		ii
ABSTRACT		iii
DEDICATION		iv
ACKNOWLEDGEMENTS		v
CONTENTS		viii
LIST OF FIGURES		xi
LIST OF TABLES		xiii
NOMENCLATURE		N.1
1	ARGON OXYGEN DECARBURIZATION MODEL	1.1
1.1	Introduction	1.1
1.1.1	The Middelburg Steel and Alloys meltshop	1.1
1.1.2	Description of the AOD converter at Middelburg Steel and Alloys	1.1
1.2	Literature Survey	1.6
1.3	Outline of Model	1.9
1.3.1	Tuyere reaction zone model	1.9
1.3.2	Rising bubble reaction zone	1.10
1.3.3	Bulk slag and metal phase interface reaction zone	1.11
2	TUYERE ZONE REACTION MODEL	2.1
2.1	Qualitative Description of Model	2.1
2.2	Mathematical Description of Model	2.3
2.2.1	Bubble formation at the tuyeres	2.3
2.2.2	Termodynamic equilibrium at the metal/gas interface of the bubbles	2.4
2.2.3	Kinetics of oxide formation and other mass transfer processes in the bubbles	2.6
2.2.4	Numerical integration of the model	2.6
2.3	Results	2.9

		Page
3	MASS TRANSFER TO RISING BUBBLES IN TUYERE AND RISING BUBBLE REACTION ZONES	3.1
3.1	Introduction	3.1
3.2	Mathematical Description	3.2
4	RISING BUBBLE REACTION MODEL	4.1
4.1	Qualitative Description of Model	4.1
4.1.1	Purpose of model	4.1
4.1.2	Rising bubble reaction zone	4.1
4.1.3	Oxide particle formation	4.2
4.1.4	Passage of bubbles and oxide particles through the rising bubble reaction zone	4.2
4.1.5	Decarburization reaction at metal/gas interface of bubble	4.4
4.1.6	Mass transfer of carbon and oxygen through boundary layer surrounding bubbles	4.4
4.1.7	Dissociation of reducible oxides in oxide particles	4.5
4.1.8	Mass transfer of oxygen through boundary layer surrounding oxide particles	4.5
4.1.9	Coupling of oxygen mass transfer through oxide particle and bubble boundary layers	4.5
4.1.10	Mass transfer of nitrogen between bubbles and liquid metal	4.6
4.1.11	Reduction of oxide particles by silicon	4.6
4.1.12	Mass transfer of silicon through boundary layer surrounding oxide particles	4.6
4.1.13	Dissociation and reduction rates of individual oxides in oxide particles	4.7
4.2	Mathematical description of model	4.8
4.2.1	Calculation of equilibrium constants	4.8
4.2.2	Outline of procedure for calculating gas and oxide flowrates as functions of position	4.9
4.2.3	Calculation of variables relating to bubbles at a vertical distance h above the tuyeres	4.9
4.2.4	Calculation of variables relating to oxide particles at a vertical distance h above the tuyeres	4.11
4.2.5	Calculation of Gibb's free energy of reduction of metal oxides by carbon and silicon	4.13
4.2.6	Calculation of oxygen concentration in metal phase at metal/oxide interface	4.15
4.2.7	Calculation of silicon concentration in the metal phase at the metal/oxide interface	4.15

		Page
4.2.8	Calculation of the decarburization and desiliconization rates at the i'th level	4.16
4.2.9	Formulation of the differential equations describing the rate of change of the integrated vertical gas and oxide flowrates	4.16
4.3	Numerical integration between the level h and h+Δh above the tuyeres	4.18
4.4	Results	4.18
5	MODEL FOR THE ESTIMATION OF THE BATH DEPTH AT THE TUYERE LEVEL	5.1
5.1	Introduction	5.1
5.2	Calculation of Tuyere Depth and Associated Ferrostatic Pressure	5.6
5.2.1	Calculation of metal and slag phase densities and volumes	5.6
5.2.2	Calculation of metal volume below tuyere level	5.6
5.2.3	Calculation of the vertical distance between the tuyeres and the slag/metal interface	5.7
5.2.4	Calculation of the thickness of the slag layer	5.9
5.2.5	Calculation of the ferrostatic pressure at the tuyere level	5.10
6	MODEL FOR DETERMINING THE EQUIVALENT LINING THICKNESS AND HOT FACE SURFACE AREA OF THE REFRACTORY LINING	6.1
6.1	Introduction	6.1
6.2	Mathematical Description of Model	6.4
6.2.1	Equivalent lining thickness	6.4
6.2.2	Bottom section of vessel	6.5
6.2.3	Lower conical and cylindrical sections of vessel	6.5
6.2.4	Vessel dome	6.7
6.2.5	Total vessel lining	6.7

		Page
7	MODEL FOR THE UNSTEADY STATE HEAT FLOW THROUGH THE REFRACTORY LINING	7.1
7.1	Introduction	7.1
7.2	Mathematical Formulation of the Model	7.1
7.2.1	Numerical formulation of the unsteady state heat flow through the lining	7.1
7.2.2	Temperature dependence of refractory lining thermal diffusivity	7.4
7.2.3	Estimation of the heat flow rate between the vessel contents and the refractory lining	7.7
7.2.4	Estimation of the vessel shell temperature	7.8
7.3	Results	7.9
8	THE UNIFIED ACID PROCESS MODEL	8.1
8.1	Introduction	8.1
8.2	Mass Balances	8.3
8.2.1	Mass balances during the decarburization process	8.3
8.2.2	Mass balances associated with charging vessel additions	8.5
8.3	Heat Balance	8.6
8.3.1	Heat balance during the decarburization process	8.6
8.3.2	Heat balance associated with the charging of vessel additions	8.9
8.4	Numerical Solution of the Differential Mass and Energy Balances	8.11
8.4.1	Introduction	8.11
8.4.2	Initialization of variables at the start of the first process time step of a blowing stage	8.11
8.4.3	Numerical solution of the simultaneous differential equations defining the trajectories of the metal and slag heat content and composition	8.12
8.5	Results	8.12
8.5.1	Overall results	8.12
8.5.2	Temperature	8.16
8.5.3	Carbon	8.17

		Page
8.5.4	Silicon	8.19
8.5.5	Manganese	8.20
8.5.6	Chromium	8.20
8.5.7	Nickel, molybdenum and iron	8.21
8.5.8	Nitrogen	8.21
8.5.9	Oxygen	8.21
8.5.10	Computation time	8.21
9	CONCLUSIONS	9.1
9.1	Summary and Conclusions	9.1
9.2	Recommendations for Future Work	9.2
APPENDICES		
APPENDIX A	Derivation of the Decarburization Rate Equation used in the Rising Bubble Reaction Model	A.1
A.1	Introduction	A.1
A.2	Derivation of the decarburization rate equation	A.3
APPENDIX B	Derivation of the Equilibrium Constant used in the Decarburization Rate Equation	B.1
APPENDIX C	Calculation of Activity Coefficients	C.1
REFERENCES		R.1

LIST OF FIGURES

Figure		Page
2.1	Schematic representation of the tuyere reaction model	2.2
2.2	Typical tuyere reaction model data in respect of gas flowrates resulting from a 3:1 O_2:N_2 blowing ratio and an initial 15mm diameter bubble	2.10
2.3	Typical tuyere reaction model data in respect of oxide flowrates resulting from a 3:1 O_2:N_2 blowing ratio and an initial 15mm diameter bubble	2.11
2.4	Typical tuyere reaction model data in respect of gas flowrates resulting from a 1:1 O_2:N_2 blowing ratio and an initial 15mm diameter bubble	2.13
2.5	Typical tuyere reaction model data in respect of oxide flowrates resulting from a 1:1 O_2:N_2 blowing ratio and an initial 15mm diameter bubble	2.14
3.1	Rising velocity of single bubbles in water	3.3
4.1	Schematic representation of the rising bubble reaction zone	4.1
4.2	Schematic representation of a bubble, an oxide particle and the associated boundary layers and concentration gradients in the rising bubble reaction zone	4.3
4.3	Typical rising bubble reaction model data output in respect of gas flowrates resulting from a 3:1 O_2:N_2 blowing ratio and an initial 15mm diameter bubble at the tuyeres	4.20
4.4	Typical rising bubble reaction model data output in respect of oxide flowrates resulting from a 3:1 O_2:N_2 blowing ratio and an initial 15mm diameter bubble at the tuyeres	4.21
4.5	Typical rising bubble reaction model data output in respect of gas flowrates resulting from a 1:1 O_2:N_2 blowing ratio and an initial 15mm diameter bubble at the tuyeres	4.22
4.6	Typical rising bubble reaction model data output in respect of oxide flowrates resulting from a 1:1 O_2:N_2 blowing ratio and an initial 15mm diameter bubble at the tuyeres	4.23

Figure		Page
5.1	Vertical cross section through vessel shell and lining	5.2
6.1	Simplifying model of the dependence of lining thickness on heat number	6.2
6.2	Resistor analogue of heat flow through refractory lining	6.3
6.3	The n'th brick course of the vessel lining	6.5
7.1	Finite element model of temperature distribution and heat flow through through the refractory lining	7.1
7.2	Schematic subdivision of vessel lining into incremental distance increments for unsteady state heat flow calculations	7.4
7.3	Data sheet for Wulfrath SINDOFORM K fired, direct bonded, dolomite bricks	7.5
7.4	Temperature dependence of the thermal conductivity of dolomite bricks	7.6
7.5	Calculated temperature profile development in a new refractory lining	7.11
8.1	Comparison of computed composition and temperature trajectories with actual plant data for a 4:1 blowing step	8.13
8.2	Comparison of computed composition and temperature trajectories with actual plant data for a 1:1 blowing step	8.14
A1	Schematic representation of concentration gradients in the boundary layers at the metal/gas interface of a bubble and the metal/oxide interface of an oxide particle	A.2

LIST OF TABLES

Table		Page
3.1	Diffusivities of elements in liquid iron at 1650°C	3.1
5.1.1	New working lining thickness of the lower conical and cylindrical sections of the vessel	5.4
5.1.2	Final working lining thickness of the lower conical cylindrical sections of the vessel	5.5
8.1	Plant data for 4:1 blowing step of heat #79447	8.15
8.2	Plant data for 1:1 blowing step of heat #79447	8.16
C1	First order Henrian interaction parameters (ex Deb Roy et.al.)	C.1
C2	First order Henrian interaction parameters (ex Sigworth and Elliot)	C.2
C.3	Interaction parameters for Nitrogen in liquid iron	C.3

NOMENCLATURE

A	Surface area (m)
α_L	Thermal diffusivity of the lining.
A_{BUB}	Surface area (m²) of a bubble.
A_i	Temperature independent term for calculating the density of the i'th metal phase component as a linear function of temperature.
A_j	Temperature independent term for the standard free energy of formation for the j'th oxide M_xO_y.
A_j	Temperature independent term for the standard free energy of formation of a 1% solution of the j'th component M in liquid iron.
$A_{L,H}$	Total surface area of lining hot face (m²).
A_O	Temperature independent term for the standard free energy of formation of a 1% solution of oxygen in liquid iron.
A_{OX}	Surface area (m²) of an oxide particle.
$A_{OX,j}$	Temperature independent term for calculating the density of the j'th oxide M_xO_y as a linear function of temperature.
A_{Si}	Temperature independent term of the standard free energy of formation of a 1% solution of silicon in liquid iron.
A_{SiO2}	Temperature independent term of the standard free energy of formation of SiO_2.
$a_{i,j}$	Activity of component j in the metal phase at the metal/gas interface.
$a_{ox,j}$	Activity of the j'th oxide M_xO_y in the oxide mixture formed in bubbles in the tuyere reaction zone.
$a_{ox,j}$	Activity of the j'th oxide M_xO_y in the oxide phase at the metal/oxide interface of an oxide particle.
B_i	Temperature dependent term for calculating the density of the i'th metal phase component as a linear function of temperature.
B_j	Temperature dependent term of the standard free energy of formation of the j'th oxide M_xO_y.

NOMENCLATURE

A	Surface area (m).
α	Thermal diffusivity of the lining.
A_{BUB}	Surface area (m²) of a bubble.
A_i	Temperature independent term for calculating the density of the i'th metal phase component as a linear function of temperature.
A_j	Temperature independent term for the standard free energy of formation for the j'th oxide M_xO_y.
A_j	Temperature independent term for the standard free energy of formation of a 1% solution of the j'th component M in liquid iron.
$A_{L.IN}$	Total surface area of lining hot face (m²).
A_O	Temperature independent term for the standard free energy of formation of a 1% solution of oxygen in liquid iron.
A_{OX}	Surface area (m²) of an oxide particle.
$A_{OX,i}$	Temperature independent term for calculating the density of the j'th oxide M_xO_y as a linear function of temperature.
A_{Si}	Temperature independent term of the standard free energy of formation of a 1% solution of silicon in liquid iron.
A_{SiO2}	Temperature independent term of the standard free energy of formation of SiO_2.
$a_{i,j}$	Activity of component j in the metal phase at the metal/gas interface.
$a_{ox,i}$	Activity of the j'th oxide M_xO_y in the oxide mixture formed in bubbles in the tuyere reaction zone.
$a_{ox,j}$	Activity of the j'th oxide M_xO_y in the oxide phase at the metal/oxide interface of an oxide particle.
B_i	Temperature dependent term for calculating the density of the i'th metal phase component as a linear function of temperature.
B_j	Temperature dependent term of the standard free energy of formation of the j'th oxide M_xO_y.

B_j	Temperature dependent term of the standard free energy of formation of a 1% solution of the j'th component M in liquid iron.
BLT	Backup lining thickness (m).
B_o	Temperature dependent term of the standard free energy of formation of a 1% solution of oxygen in liquid iron.
$B_{ox,j}$	Temperature dependent term for calculating the density of the j'th oxide M_xO_y as a linear function of temperature.
B_{Si}	Temperature dependent term of the standard free energy of formation of a 1% solution of silicon in liquid iron.
B_{SiO2}	Temperature dependent term of the standard free energy of formation of SiO_2.
BT_j	Thickness (m) of the vessel working lining floor bricks for a new (j=1) and worn-out (j=2) lining.
$\%C_f$	Concentration (%) of carbon in the metal phase at the metal/gas interface of a bubble.
CB_1, CB_2	Temperature independent and dependent terms respectively for calculating the overall heat capacity of the liquid metal and slag as a linear function of temperature.
$C_{b,c}$	Carbon concentration (kgmol C/m³) in the bulk liquid metal.
$C_{f,c}$	Carbon concentration (kgmol C/m³) in the metal phase at the metal/gas interface of a bubble.
$C_{f,c}$	Carbon concentration (kgmol C/m³) in the metal phase in equilibrium with O and CO at the metal/gas interface of a bubble.
$C_{f,N}$	Nitrogen concentration (kgmol N/m³) in the metal phase at the metal/gas interface of a bubble.
$C_{f,O}$	Oxygen concentration (kgmol O/m³) in the metal phase at the metal/gas interface of a bubble.
$C_{f,O}$	Oxygen concentration (kgmol O/m³) in the metal phase in equilibrium with C and CO at the meta./gas interface of a bubble.
$C_{MET,c}$	Carbon concentration (kgmol C/m³) in the bulk liquid metal phase.

$C_{MET,N}$	Nitrogen concentration (kgmol N/m³) in the bulk liquid metal phase.
$C_{MET,O}$	Oxygen concentration (kgmol O/m³) in the bulk liquid metal phase associated with a rising bubble.
$C_{MET,Si}$	Silicon concentration (kgmol Si/m³) in the bulk liquid metal phase.
$C^{*}_{IM,j}$	Oxygen concentration (kgmol O/m³) in the metal phase (at the metal/oxide interface) in equilibrium with the j'th oxide M_xO_y in an oxide particle.
$C_{EX,O}$	Oxygen concentration (kgmol O/m³) in the metal phase (at the metal/oxide interface) in equilibrium with an oxide particle.
$C_{EX,Si}$	Silicon concentration (kgmol Si/m³) in the metal phase of the metal/oxide interface of an oxide particle.
C_P	Heat capacity or specific heat (kJ/kg/°K) of the lining.
$C_{j,X}$	Concentration (kgmol/m³) of element j at position X where:- X="IN" is the metal/gas interface of bubble X="BU" is the bulk liquid metal X="OX" is the metal/oxide interface of oxide particle
$\%C$	Carbon concentration (%) in the bulk liquid metal.
D_C	Diffusivity or coefficient of diffusion (m²/s) of carbon in liquid iron.
D_j	Diffusivity or coefficient of diffusion (m²/s) of the j'th element in liquid iron.
D_N	Diffusivity or coefficient of diffusion (m²/s) of nitrogen in liquid iron.
D_O	Diffusivity or coefficient of diffusion (m²/s) of oxygen in liquid iron.
D_{Si}	Diffusivity or coefficient of diffusion (m²/s) of silicon in liquid iron.
DH	Vertical height (m) of a layer of brickwork in the vessel lining.
DV_j	Volume (m³) of the "half disk" of metal enclosed by the j'th layer of bricks.
d_{BUB}	Diameter (m) of a bubble.

$d_{bub}(h)$	Diameter (m) of a bubble at a vertical distance h above the tuyeres.
$d_{bub}(t)$	Diameter (m) of a bubble of age t.
$d_{bub}(x)$	Diameter (m) of a bubble at a vertical distance x below the slag/metal interface.
$d_{bub}(0)$	Diameter (m) of a bubble initially formed at a tuyere.
dV_j	Volume (m^3) of the "half disk" of metal enclosed by the j'th layer of bricks of the AOD vessel lining.
$e_{j,k}$	First order parameter for the interaction of element k on element j in liquid iron.
$e_{N,j}$	First order parameter for the interaction of element j on nitrogen in liquid iron.
ΔF^o_j	Standard free energy of formation (kJ/kgmol M) of a 1% solution of the j'th element M in liquid iron.
f_j	Henrian activity coefficient of the j'th element in the metal phase.
H_j	Raoultian activity coefficient of the j'th element in the metal phase.
f_N	Activity coefficient for nitrogen dissolved in the liquid metal phase.
f_{Si}	Activity coefficient for silicon dissolved in the liquid metal phase.
G	Gravitational acceleration (m/s^2).
$\Delta G^o_{diss,j}$	Gibb's free energy (kJ/kgmol M_xO_y) for the for the dissociation of the j'th oxide M_xO_y at the surface of an oxide particle.
ΔG_C	Sum of the free energies for reducton by carbon.
ΔG_j	Free energy of formation (kJ/kgmol) of j'th oxide M_xO_y.
ΔG_{Si}	Sum of the free energies for reducton by silicon.
ΔG^o_j	Standard free energy of formation (kJ/kgmol) of the j'th oxide M_xO_y.
ΔG^o_j	Standard free energy of formation (kJ/kgmol) of the j'th oxide M_xO_y from a standard 1% solution of M in liquid iron.

$\Delta G_{MeOy,C}$	Gibb's free energy (kJ/kgmol C) for the reduction of an oxide M_xO_y by carbon according to the reaction:-
	$1/y\ M_xO_y + [C] \rightarrow CO + x/y\ [M]$
$\Delta G_{MeOy,Si}$	Gibb's free energy (kJ/kgmol Si) for the reduction of an oxide M_xO_y by silicon according to the reaction:-
	$2/y\ M_xO_y + [Si] \rightarrow SiO_2 + 2x/y\ [M]$
$\Delta G_{j,C}$	Gibb's free energy (kJ/kgmol C) for the for the reduction of th j'th oxide M_xO_y by carbon.
$G_{F,j}$	Flow rate (kgmol/s) of the j'th gas supplied to the tuyeres, where:-
	j=1 total gases j=2 oxygen j=3 nitrogen j=4 argon
$\Delta G_{j,Si}$	Gibb's free energy (kJ/kgmol Si) for the for the reduction of the j'th oxide M_xO_y by silicon.
H_{HEATH}	Heat content (kJ) of the liquid metal and slag in the vessel.
$HM_{1,j}$	Temperature independent term for calculating the sensible heat (kJ/kgmol/°K) of the j'th element in the liquid metal as a linear function of temperature.
$HM_{2,j}$	Temperature dependent term for calculating the sensible heat (kJ/kgmol/°K) of the j'th element in the liquid metal as a linear function of temperature.
$HO_{1,k}$	Temperature independent term for calculating the sensible heat (kJ/kgmol/°K) of the k'th oxide in the slag as a linear function of temperature.
$HO_{2,k}$	Temperature dependant term for calculating the sensible heat (kJ/kgmol/°K) of the k'th oxide in the slag as a linear function of temperature.
$\Delta H^{\circ}_{f}(T)$	Standard heat of formation (kJ/kgmol M_xO_y) of the k'th oxide as a function of temperature.
h	Vertical distance (m) of a bubble above the tuyeres.
h(t)	Vertical distance (m) of a bubble of age t above the tuyeres.
h_{SP}	Vertical height (m) of the segment of a sphere forming the bottom of the vessel.
J	Molar flux (kgmol/m²/s).

J_c Molar flux (kgmol ... of carbon.

J_{co} Molar flux (kgmol ...²/s) of carbon monoxide through the gas phase boundary layer at the metal/gas interface of a bubble.

J_j Molar flux (kgmol/m²/s) of the j'th element through the metal phase boundary layer surrounding a bubble or an oxide particle. Possible elements include the following:-

j=1	carbon	j=5	molybdenum
j=2	silicon	j=6	nickel
j=3	manganese	j=7	iron
j=4	chromium	j=13	nitrogen

J_N Molar flux (kgmol/m²/s) of nitrogen.

J_o Molar flux (kgmol/m²/s) of oxygen.

$J_{o,ox-dec}$ Oxygen flux (kgmol O/m²/s) associated with the (decarburization reaction induced) dissociation of an oxide, represented by M_xO_y, at an oxide particle surface.

$J_{Si,ox-d}$ Silicon flux (kgmol Si/m²/s) associated with the reduction of an oxide, represented by M_xO_y, at an oxide particle surface.

K^* Equilibrium constant for the reaction:-
[C] + [O] <=> CO

$K_{ox,j}$ Equilibrium constant for the dissociation of the j'th oxide at the metal/oxide interface of an oxide particle according to the reaction:-

$1/y\ M_xO_y$ <=> x/y [M] + [O]

K_{dc} Equilibrium constant for the decarburization reaction:-

%C] + [%O] <=> CO

t the metal/gas interface of a bubble.

K_j Equilibrium contant for the formation of the j'th oxide M_xO_y according to the reaction:-

x [M] + $y/2\ O_2$ <=> M_xO_y

K_N Equilibrium constant for the nitrogen dissolution reaction:-

$1/2\ N_2$ <=> [N]

$k_{BUB,C}$ Mass transfer coefficient (m/s) for carbon through the metal phase boundary layer surrounding a rising bubble.

$k_{BUB,k}$ Mass transfer coefficient (m/s) for the k'th element through the metal phase boundary layer surrounding a bubble. Possible elements are the same as for J, above.

$k_{BUB,N}$ Overall mass transfer coefficient (m/s) for nitrogen through the metal phase boundary layer and metal/gas interface surrounding a rising bubble.

$k_{BUB,O}$ Mass transfer coefficient (m/s) for oxygen through the metal phase boundary layer surrounding a rising bubble.

$k_{L,\lambda}$ Thermal conductivity (kJ/m/s/°K) of the refractory lining.

$k^{A}_{L,m}$ Average thermal conductivity (kJ/m/s/°K) of a refractory lining segment in direct contact with the liquid vessel contents.

k_N Overall mass transfer coefficient (m/s) for nitrogen through the metal phase boundary layer and metal/gas interface surrounding a bubble.

k_N^{x}
$k^{x}_{BUB,N}$ Mass transfer coefficient (m/s) for nitrogen through the metal phase boundary layer surrounding a rising bubble.

k_N^{x} Mass transfer coefficient (m/s) for nitrogen through the gas/metal interface, poisoned by S and O, surrounding a bubble.

$k_{OX,O}$ Mass transfer coefficient (m/s) for the diffusion of oxygen through the metal phase boundary layer surrounding an oxide particle.

$k_{OX,Si}$ Mass transfer coefficient (m/s) for the diffusion of silicon through the metal phase boundary layer surrounding an oxide particle.

k_R Rate constant for the reaction:-
[C] + [O] -> CO

$k_{X,j}$ Mass transfer coefficient (m/s) for the j'th element through the X'th metal phase boundary layer where:-

X="BUB" is the boundary layer surrounding a bubble
X="OX" is the boundary layer surrounding an oxide particle

LT Lining thickness (m) at a particular position.

M_j Atomic weight (kg/kgmol) of the j'th element in the metallic phase. Possible elements include the following:-

j=1	carbon	j=8	aluminium
j=2	silicon	j=9	titanium
j=3	manganese	j=10	copper
j=4	chromium	j=11	sulphur
j=5	molybdenum	j=12	phosphorus
j=6	nickel	j=13	nitrogen
j=7	iron	j=14	oxygen

M_N Atomic weight (kg/kgmol) of nitrogen.

$\%M_j$ concentration (%) of the j'th element in the metal bath

$\%M_{j,k}$ Concentration (%) of element k in the j'th alloying material charged.

$\%N^*_{j,k}$ Concentration (%) of oxide k in the j'th fluxing material charged.

$M_{OX,j}$ Molecular weights of the j'th oxide. Possible oxides lude the following:-

j=1	CO	j=6	NiO
j=2	SiO_2	j=7	FeO
j=3	MnO	j=8	Al_2O_3
j=4	Cr_2O_3	j=9	TiO_2
j=5	MoO_3	j=10	CaO

$M_{SLG,j}$ Molecular weight of the j'th slag forming compound. Possible compounds include those listed above (CO excluded) and the following:-

j=13	CaO
j=14	MgO
j=15	CaF_2

$m_{ALLOY,j}$ Mass (kg) of the j'th alloying material charged.

$m_{FLUX,j}$ Mass (kg) of the j'th j'th fluxing material charged.

$m_{MET,j}$ kg of the j'th element in the metal bath.

$m_{SLG,j}$ Mass (kg) of the j'th oxide M_jO_y in the slag.

$N_{MET,j}$ kgmol of the j'th element in the metal bath. For the j'th elements refer M_j above.

$N_{MET,Si}$ kgmol of silicon in the metal bath.

$N_{SLG,j}$ Quantity (kgmol) of the j'th oxide M_xO_y in the slag.

$N'_{Ar}(h)$ Flow rate (kgmol/s) of argon through an imaginary horizontal plane at a vertical distance h above the tuyeres.

$N'_{CO}(h)$ Flow rate (kgmol/s) of carbon monoxide through an imaginary horizontal plane at a vertical distance h above the tuyeres.

$N'_{GAS}(h)$ Total gas flowrate (kgmol/s) through an imaginary horizontal plane through the metal at an arbitrary vertical distance h above the level of the tuyeres.

$N'_{GAS,j}(h)$ Flow rate (kgmol/s) of the j'th gas type through an imaginary horizontal plane through the metal bath at a vertical distance h above the the tuyeres. Gas types are as follows:-

j=1	carbon monoxide
j=2	oxygen
j=3	nitrogen
j=4	argon

$N'_{N2}(h)$ Flow rate (kgmol/s) of nitrogen through an imaginary horizontal plane at a vertical distance h above the tuyeres.

$N'_{O2}(h)$ Flow rate (kgmol/s) of oxyge. through an imaginary horizontal plane at a vertical distance h above the tuyeres.

$N'_{OX}(h)$ Total oxide flowrate (kgmol/s) in or associated with bubbles at a vertical distance h above the tuyeres.

$N'_{OX,j}(h)$ Flow rate (kgmol/s) of the j'th oxide (forming in and rising in close association with bubbles) through an imaginary horizontal plane through the metal bath at an arbitrary vertical distance h above the level of the tuyeres. Possible oxide types are as follows:-

j=2	SiO_2	j=5	MoO_3
j=3	MnO	j=6	NiO
j=4	Cr_2O_3	j=7	FeO

N_a Avogadro's volume = 22.414 m^3/kgmol

%N Concentration (%) of nitrogen dissolved in the bulk liquid metal.

$\%N_i$ Equilibrium %N in the metal phase at the metal/gas interface of a bubble.

$\%N_e(h)$	Equilibrium %N in the metal phase at the metal/gas interface of a bubble at a vertical distance h above the tuyeres.
$\%N_i(t)$	Equilibrium %N in the metal phase at the metal/gas interface of a bubble of age t.
$\dot{n}_{bub}$	Rate of formation (number per sec) of bubbles at the tuyeres. Also the flowrates of bubbles and oxide particles through an imaginary horizontal plane through the metal bath at an arbitrary position above the tuyeres.
$\%O_i$	Concentration (%) of oxygen in the metal phase at the metal/gas interface of a bubble.
P_{Atm}	Atmospheric pressure. (kN/m^2)
P_{CO}	Partial pressure of CO in a bubble.
P_{CO_i}	Partial pressure of CO at the gas/metal interface of a bubble.
P(h), P(x)	Ferrostatic pressure (atm) at a vertical distance h above the tuyeres or depth x below the metal/slag interface
P_j	Partial pressure (atm) of the j'th gas in a bubble, where:- j=1 carbon monoxide j=2 oxygen j=3 nitrogen j=4 argon
P_{N_2}	Partial pressure (atm) of nitrogen in a bubble.
P_{O_2}	Partial pressure (atm) of oxygen in bubble in tuyere reaction zone.
P(t)	Ferrostatic pressure in a bubble of age t.
P_{Tuy}	Ferrostatic pressure (atm) at tuyere level.
P(x)	Ferrostatic pressure (atm) in a bubble at a depth x below the metal/slag interface.
ρ	Density (kg/m^3) of the liquid metal.
ρ'	Molar density ($kgmol/m^3$) of the liquid metal.
ρ_{Gas}	Density (kg/m^3) of the gas in a buble.

ρ_j Density (kg/m³) of the j'th metal phase element at 1650ºC. Possible elements include:-

j=1	carbon	j=6	nickel
j=2	silicon	j=7	iron
j=3	manganese	j=8	aluminium
j=4	chromium	j=9	titanium
j=5	molybdenum	j=10	copper

$\rho_{r.in}$ Density (kg/m³) of the refractory lining.

ρ_{ox} Density (kg/m³) of an oxide particle.

$\rho_{ox,i}$ Density (kg/m³) of the j'th oxide phase component. Possible compounds include those listed for $X_{ox,i}$ above.

ρ_{slg} Slag density (kg/m³)

$\rho_{slg,j}$ Density (kg/m³) of the j'th slag phase component. Possible compounds include those listed for $X_{slg,j}$ above.

π 3,141592654

Q Total volumetric flowrate (m³/s), at standard temperature and pressure, of gases being supplied to the tuyeres.

Q^* Volumetric flow rate (m³/s) of the gas mixture entering the bath at tuyere level pressure and bath temperature.

$q_{exgases}$ Rate of heat loss (kJ/s) via the hot gases leaving the vessel mouth.

$q_{r.in}$ Heat flow rate (kJ/s) between the refractory lining and the contents of the vessel.

q_{ox} Volumetric flowrate (m³/s) of oxide particles through an imaginary horizontal plane cutting the metal bath at an arbitrary position above the tuyeres.

q_R Rate of heat generation (kJ/s) by chemical reaction.

q_{rad} Rate of heat loss (kJ/s) via the radiation through the vessel mouth.

q_{tuyres} Rate of heat (kJ/s) input to the vessel via the gases entering the vessel through the tuyeres.

q_{ss} Heat flux (kJ/m²/s) from the refractory lining into the vessel shell.

q_{conv} Convective heat flux (kJ/m²/s) from the vessel shell.

q_{RAD}	Radiation heat flux (kJ/m²/s) from the vessel shell.
q_{OUT}	Heat flux (kJ/m²/s) out of the vessel shell to the surroundings.
R	Gas constant
$RT_{t,j}$	Temperature (°K) of refractory lining at position j and time t.
$RT_{2,j}$	Temperature (°K) of refractory lining at position j and time $t+\Delta t$.
$\dot{r}_C(h)$	Decarburization rate (kgmol C/m²) at a vertical distance h above the tuyeres in the metal bath.
$\dot{r}_{Si}(h)$	Desiliconization rate (kgmol Si/m²) at a vertical distance h above the tuyeres in the metal bath.
$r_{j,k}$	Inner radius (m) of the lining at brick layer j and radial position k degrees from the midpoint between #2 and #3 tuyeres.
r_{Ox}	Radius (m) of an oxide particle.
r_{BP}	Radius (m) of the segment of a sphere forming the base of the vessel.
T_{AIR}	Ambient temperature (°K) of the vessel surroundings.
T_B	Temperature (degrees Kelvin) of the metal bath.
$T_{t,Y}$	Temperature (°K) at time t and at distance Y from the hot face in the refractory lining.
T_{VS}	Temperature (°K) of the vessel shell.
t	Elapsed process time.
t	Age (s) of a bubble in the tuyere reaction zone.
t_e	Contact time (s) parameter of the Higbie Surface Renewal Model. For a bubble or spherical particle, this is the time taken for it to rise through a vertical distance of one diameter relative to the surrounding fluid.
$t_{e,BUB}(x)$	Higbie Surface Renewal Model contact time (s) parameter for a rising bubble at a depth x below the slag/metal interface.
$t_{e,OX}$	Higbie Surface Renewal model contact time (s) parameter for a rising oxide particle.
t_s	Duration (s) of a process time step.

μ	Viscocity (kg/m/s) of the liquid metal.
u_{bub}	Rising velocity (m/s) of a bubble.
$u_{bub}(h)$	Rising velocity (m/s) of a bubble vertical distance h above the tuyeres.
$u_{bub}(t)$	Rising velocity (m/s) of a bubble of age t.
V_a	Volume (m^3) of liquid metal above the tuyeres.
V_b	Volume (m^3) of liquid metal below the tuyeres.
$V_{bub}(h)$	Volume (m^3) of an individual bubble at a vertical distance h above the tuyeres.
$V_{bub}(t)$	Volume (m^3) of an individual bubble of age t.
VL_1	Number of heats completed to date with the current vessel lining (ie. age of vessel lining).
VL_2	Estimated number of heats that will be completed with the current vessel lining before it has to be replaced.
V_m	Volume (m^3) of the liquid metal in the AOD vessel.
VR	Inner radius (m) of the vessel lining at a particular position.
V_{slag}	Volume (m^3) of slag in the AOD vessel.
Vsp	Volume (m^3) of liquid metal in the segment of a sphere forming the bottom of the vessel.
W_o	Molar flowrate (kgmol O/s) of reducible oxygen in oxide particles through an imaginary horizontal plane cutting the metal bath at an arbitrary position above the tuyeres.
W_{ox}	Mass flowrate (kg/s) of oxide particles through an imaginary horizontal plane cutting the metal bath at an arbitrary position above the tuyeres.
$X_{i,j}$	Molar fraction of the j'th element in the metal phase at the gas/metal interface of a bubble.
$X_{BULK,j}$	Molar fraction of the j'th element in the bulk liquid metal.

$X_{Ox,j}(h)$ Molar fraction of the j'th oxide (j>1) in the mixture associated with bubbles at a vertical distance h above the tuyeres. Possible oxide types are as follows:-

j=2	SiO_2	j=5	MoO_3
j=3	MnO	j=6	NiO
j=4	Cr_2O_3	j=7	FeO

$X_{Sla,j}$ Molar fraction of the j'th oxide M_xO_y in the slag.

x Vertical distance (m) below the slag/metal interface.

$x_{m,s}$ Thickness (m) of slag layer floating on top of the metal in the vessel.

x_{Tuy} Vertical distance of the tuyeres below the slag/metal interface.

Y_{Liw} Equivalent lining thickness (m).

$z_{x,j}$ Constants defining the stoichiometry of the j'th oxide $z_{y,j}$ M_xO_y where $z_{x,j}$ is equivalent to x and $z_{y,j}$ is equivalent to y.

1 ARGON OXYGEN DECARBURIZATION PROCESS MODEL

1.1 Introduction

1.1.1 The Middelburg Steel and Alloys Meltshop

Middelburg Steel and Alloys (MS&A), the major producer of stainless steel in South Africa, operates an integrated steelworks at its Middelburg plant. The steelworks includes a meltshop which converts a variety of raw materials into liquid steel via a 50 ton 25MVA Demag electric arc melting furnace and a 55 ton Demag argon oxygen decarburization (AOD) refining vessel.

The Meltshop at MS&A typically produces between eight an eleven heats per day. The arc furnace normally taps out approximately 50 liquid tons of steel per heat at about 1620°C. The tap-out carbon content is generally in the range 1,3-2,2%.

The AOD refining operation drops the carbon content of the liquid steel down to the 0,020-0,050% range. In addition to carbon removal, the final chemistry of the steel is "fine tuned" by the addition of a variety of suitable alloying materials, reductants and fluxes during the process. This results in a mass increase and the tap-out mass of refined steel is typically 53-55 tons.

The liquid steel, following an argon stirring operation to homogenize the temperature in a transfer ladle, is continuously cast into slab. The slab serves as the feedstock for the rolling operation for the production of hot rolled plate and cold rolled sheet material.

A wide range of both austenitic and ferritic grades of stainless steel, including 3CR12 (developed by MS&A) are produced.

1.1.2 Description of the AOD converter and process used at MS&A

1.1.2.1 Basis of the process

The AOD process was originally developed by the Union Carbide Corporation during the 1960's. The process has been well documented (see section 1.2 for a summary of the relevant literature). It is based on the principle of diluting the carbon monoxide, produced by the decarburization reaction:-

$$[C] + [O] \Leftrightarrow CO \qquad (1.1)$$

with an inert gas such as argon or nitrogen.

This dilution of the carbon monoxide reaction product shifts the

equilibrium represented by equation 1.1 in the direction of carbon monoxide formation. This significantly improves the efficiency of carbon removal by oxygen in a situation of strong thermodynamic competition for oxygen by elements such as chromium and manganese. Chromium is typically present in concentrations ranging from approximately 11% to 24%, depending on the steel type being produced.

1.1.2.2 Vessel construction

The AOD reaction vessel consists of a refractory brick lined steel shell. The middle section is cylindrical. The base consists of a segment of a sphere. The lower and upper sections of the vessel are sections of a cone. There is an opening in the upper section to allow charging of liquid metal, the addition of alloying, fluxing and reducing materials and the escape of gaseous reaction products and inert gases.

The lining material for the vessel is direct bonded fired dolomite bricks. During the early days of AOD development chrome magnesite was the commonly used refractory material.

1.1.2.3 Tuyere construction

A mixture of oxygen and inert gas is introduced into the liquid metal via four tuyeres extending through the vessel shell and refractory lining. They are located near the bottom of the lower conical section of the vessel. Each tuyere consists of two pipes; a copper inner pipe supported inside a stainless steel outer pipe.

The annulus formed between the two pipes (known as the "shroud") is kept cool by blowing part of the inert gas requirement through it. The balance of the inert gas requirement and all the oxygen is blown through the central copper pipe (normally called the "tuyere").

1.1.2.4 Vessel rotation and gas supply

The vessel is supported in a ring that is in turn supported by two trunnion mounted bearings. The vessel and ring assembly may be rotated through 360° by a gearbox applying torque via a bull gear on one of the trunnions. This allows the vessel to be rotated, for example, from a horizontal position (used for "holding" operations, temperature measurement, sampling and tapping) into vertical and back-tilted positions (for metal charging, blowing and making vessel additions).

The trunion mounted on the opposite side of the of the ring from the gearbox incorporates a rotary valve assembly. This provides a continuous connection between the gas supply lines coming in from the gas flow control room and the manifolds distributing the various gases to the shrouds and the tuyeres.

Gas flow to the vessel is controlled via a network of pipes, flow control valves and associated instrumentation. This enables different inert gases to be selected and the flowrates of oxygen and inert gas to be individually controlled.

This is necessary to allow different ratios of oxygen and inert gas to be blown into the vessel, depending on carbon concentration and temperature. It is also possible to blow only an inert gas into the vessel for stirring purposes.

The configuration of pipes, valves and instrumentation varies from installation to installation, reflecting individual operator preferences and differences in inert gas availability.

1.1.2.5 Initial charging of the vessel

Hot metal from the electric arc furnace is charged through the mouth of the vessel from a ladle slung from an overhead crane. The metal typically contains 1,6-2,5 %C and 0,1-0,3 %Si. Concentrations of other elements such as Mn, Cr, Mo, Ni and Fe depend on the particular type of steel being produced.

Soft burnt lime (and dolomitic lime in the case of the MSBA operation) is added in sufficient quantity at the start of a heat to react with the silica that is formed during the decarburization process. This is necessary to protect the refractory lining from excessive attack by silica. The metal temperature after the lime addition at the commencement of the decarburization blow is typically 1480-1550°C.

1.1.2.6 Decarburization steps

Initially, while high carbon concentrations exist, high oxygen to inert gas ratios (4:1 and 3:1 being the most common) are used. Carbon removal efficiency, although improved by higher temperatures, begins to decline as the carbon concentration in the liquid metal decreases.

In order to maintain economically acceptable carbon removal efficiency and prevent undue chromium (and other metallics) oxidation, the ratio of oxygen to inert gas is progressively reduced in a stepwise fashion as the carbon concentration drops. Ratios that are typically used at MSBA are as follows:-

%C Range	Ratio O$_2$:Inert Gas
>1%	4:1 or 3:1
1,0-0,5%	4:1, 3:1 or 2:1
0,5-0,1%	1:1
0,1-0,05%	1:3
0,05-0,015%	1:3 or 1:6

The quantity of oxygen blown in each of these steps is determined using empirical formulae and tables based on actual operating data.

1.1.3.7 Temperature and composition control

From thermodynamic considerations alone it is desireable to operate the heats as at as high a temperature as possible to maximise impurity removal efficiency. Practical considerations of refractory lining wear dictate a maximum operating temperature of 1710-1720°C.

Since the process is strongly exothermic, it is necessary to add coolant to the vessel to prevent the temperature exceeding 1720°C. Ideally this is done with an automatic feed system where coolant feedrates can be controlled to maintain more or less constant temperatures once the 1670-1720°C operating range has been reached.

The rate of temperature rise in a particular ratio is currently predicted by the operator using empirical temperature rise factors. These factors are not very accurate and the need for an accurate prediction of the process temperature trajectory is a strong motivation for the development of a process model.

Many installations, including that at MSAA are restricted to batch charging of coolant. In operations such as these, the temperature follows a "sawtooth" trajectory once the 1670-1720°C operating range has been reached. Sufficient coolant is added every time the bath temperature reaches 1710-1720°C to drop it to 1670-1680°C. This is normally two to three times per heat.

Ideal coolants include low carbon content materials such as nickel, ferro-molybdenum and mild steel scrap. However, because of the difficulty of accurately controlling the chemistry of the hot metal tapped from the arc furnace (variability of composition and recovery of raw materials, particularly scrap), coolants may also include high carbon alloys such as charge chrome and high carbon ferro-manganese.

These high carbon materials are used during the decarburization stage of the process for reasons of economy. They are added for final chemistry control as well as for cooling the process. It should be emphasized however that chemistry control starts in the scrapyard with the control of incoming raw materials and the design of the arc furnace charge.

Soft burnt lime and dolomitic lime are also used as coolants although it is preferable to restrict their use for this purpose as far as possible. This is because extended exposure to the high process temperatures cause these materials to become "hard-burnt" and less reactive (in respect of being able to preferentially

react with SiO_2 to protect the dolomite lining from attack).

A heat typically requires between two and four coolant additions, depending on initial and final carbon concentrations.

1.1.2.8 Reduction step, slag basicity control and desulphurization

Decarburization is completed, depending on steel type, when the carbon level in the metal has been reduced to the 0,02-0,05 %C range. At this stage, in addition to the decarburized liquid metal and lime, the vessel contains a large quantity of oxides, principally Cr_2O_3, with lesser quantities of MnO and FeO. It is necessary to reduce these oxides, both to recover the metal content and to drop the oxygen content of the steel.

Ferro-silicon is the most commonly used reductant. It is added at the end of the decarburization stage of the process, together with any outstanding lime and dolomitic lime that may be required to achieve a slag with an acceptable basicity *ratio* ((%CaO+%MgO)/%SiO_2). Slag basicities of 1,5-2,2 are typical, depending on the operation.

A high slag basicity reduces erosion of the refractory lining by SiO_2 generated during the the reduction process. A high basicity is also advantageous for good sulphur removal, as is a post *reduction* level of >0,30 %Si in the metal. However excessively high (>2,0) basicities can cause problems such as difficulty in deslagging and slag build-up in ladles unless special precautions are taken. These include the use of fluorspar as a fluxing agent or the *application of slag-free tapping procedures.*

The reduction stage of the process is accomplished by stirring in the ferro-silicon and lime additions with argon for approximately five minutes. At this stage, the slag that *has been* generated is tapped off and a liquid metal sample is taken for final chemistry control.

While waiting for the analysis to be reported, a desulphurization mixture of lime and fluorspar may be charged and stirred in for about two minutes, both for sulphur removal and to absorb surplus heat. Where surplus heat is expected to be limited, the desulphurization mixture can be charged together with the reduction additions.

1.1.2.9 Final additions and tapping

It is normally necessary to make final adjustments to the liquid metal's chemistry at this stage. Additions of low carbon alloys (and high carbon alloys if upward adjustment of carbon is necessary) are made to the vessel prior to tapping. It may also be necessary to use final alloy and/or further desulphurization mixture additions as a means to lower the temperature of the liquid metal to the desired aim point.

After topping the vessel, the next heat is charged and the whole process is repeated.

1.2 Literature Survey

The AOD process was invented by the Union Carbide Corporation during the late fifties. This followed an investigation into the differences between the theoretical work of Richardson and the experimental work by Hilty and Crafts on the equilibrium ratios of chromium and carbon. It was found that significantly improved decarburization was achieved when argon was used as a coolant when attempting to perform isothermal experiments involving blowing oxygen onto the surface of molten chromium alloys.

Several years of research and development work culminated in the first patents for the AOD process being lodged in the USA in 1960. The first fullscale plant tests were conducted in conjunction with the Joslyn Steel company in 1960. However, it was not until 1968 that Joslyn was able to report their first successful 69 heats in the AOD vessel.

Since those pioneering days considerable work has been done on the AOD by numerous authors. The Union Carbide Corporation may have initiated the work on the development of mathematical models of the AOD process with the thermodynamic equilibrium model that they issued to their licensees as part of their technical knowhow package.

A number of viable models have been subsequently developed by a number of authors, the most important of which are briefly discussed below.

Asai and Szekely[14,15] proposed a mathematical model for describing the bath temperature and composition trajectories for the decarburization of stainless steel for processes operating on an industrial scale. The model is based on a set of component balances, written with the aid of driving force expressions, the appropriate equilibrium relationships, and a heat balance.

They apply the concept (originally proposed by Asai and Muchi[17,18,19]) that "during the oxygen blow the concentration of each alloying element in the bath may be calculated by establishing a balance between two driving forces, namely:-

(i) the driving force that will cause the system to tend towards thermodynamic equilibrium;

(ii) another driving force, due to oxygen supplied to the bath, which will tend to keep the system from reaching equilibrium."

R J Fruehan [16] developed a model of the AOD steelmaking process that predicts the rates of oxidation of chromium and carbon. The

model is based on the assumption that the oxygen (that is injected together with an inert gas such as argon at the tuyeres) primarily oxidises chromium in the tuyere reaction zone.

The Cr_2O_3 that is formed oxidises the carbon as it rises in the bath with the argon bubbles. In his model single effective values of interface carbon concentration and interface CO pressure are calculated by assuming that the concentration of chromium at the interface is the same as in the bulk. It is also assumed that the oxidation of carbon by Cr_2O_3 is the rate-controlling reaction and is controlled by the liquid phase mass transfer of carbon to the bubble surface.

T Deb Roy and D G C Robertson[9] developed a model applicable to both argon-oxygen (AOD) and argon-oxygen-steam (CLU) processes. The model predicts the variation of gas composition with height, and the rates of all the mass transfer processes occuring at a given height in the bath. The effect of gas phase resistance at the metal/gas interface of a bubble is taken into account and the model allows the effects of changes in pressure above the bath surface to be predicted.

In their model (as it applies to the AOD process) equilibria is assumed to exist at the metal/gas interface between solid Cr_2O_3, dissolved carbon, dissolved chromium and CO in the gas phase. It is assumed that initially dissolution of the oxide in the melt occurs at the oxide/metal interface. Then follows the reaction of dissolved carbon with dissolved oxygen to form CO at the metal/gas interface.

Their model is extended to cater for the multi-component systems typical of the commercial stainless steel refining environment. The model takes into account the non-isothermal conditions and the presence of Si, Mn, and Ni in the melt.

It is assumed that all the oxygen which enters the vessel as O_2 reacts to form Cr_2O_3, SiO_2 and MnO. A small amount of iron gets oxidised but is quickly reduced by carbon. The oxides are carried up by the gases and subsequently various amounts of the metals are reduced back into the melt by reduction of their oxides by carbon.

A heat balance is introduced to account for the non-isothermal behaviour of the bath.

Simulation of the system involves simultaneous solution of thermodynamic, kinetic and conservation equations at all positions in the bath.

I Matsuki et. al.[11] developed a model of the AOD process on which this work is largely based. Their model is very similar to the model described in the paper and UK patent application by T Tonghe et. al.[12,13]. The authors postulate that oxygen from the tuyeres reacts with metallic elements such as Si, Mn, Cr, or Fe in the bath to form oxides. The relative formation rates of these oxides is assumed to be proportional to the rate of diffusion of the

metallic elements through a boundary layer surrounding each bubble. The direct reaction with C is considered to be negligable.

The oxidized metals become suspended in the molten metal as fine particles. Decarburization proceeds as reduction of these particles by carbon. The relative rates of these reduction reactions are assumed to be proportional to their free energies. The unreduced metallic oxide particles enter the bulk slag phase floating on top of the liquid metal. The oxides in the slag are assumed to make no further contribution to decarburization.

In the model it is postulated that decarburization takes place via the following steps:-

(i) dissociation of the metallic oxides;

(ii) mass transfer of O from the oxide surface to the molten metal;

(iii) mass transfer of of O and C from the ten metal to the metal/gas interface of the bubbles;

(iv) decarburization reaction at the interface;

(v) mass transfer of gas from the interface to the bulk gas phase of the bubbles.

The model takes into account the effect of bath depth and applies to both high and low carbon ranges. In the high carbon range the decarburization rate is said to be controlled by oxygen mass transfer and in the low carbon ranges it is controlled by carbon mass transfer.

O G Paul[17] of MINTEK has recently developed a kinetic-equilibrium model of the AOD process as part of an overall process optimization and control package for the AOD operation at Middelburg Steel and Alloys. In the model it is assumed that there are three main reaction zones.

The primary reaction zone is where the gas is blown into the bath and it breaks up into equal sized bubbles. Chemical reaction between the oxygen in the gas and the meta. phase takes place at a high rate because of the high temperature and oxygen potential. It is assumed that the reacting species from the metal phase come from the layer of metal surrounding the bubble and not from the bulk liquid metal. It is assumed that the gas in the bubble comes into equilibrium with all the metal in this layer.

After equilibrium has been obtained, remaining metal from the metal layer is mixed back into the bulk metal phase in the secondary reaction zone. Slag and gas formed rise to the top of the bulk metal phase where the slag is taken up into the bulk slag phase and the gas escapes from the vessel mouth.

In the tertiary reaction zone thin layers of metal and slag at the

bulk slag/metal interface are considered to come to equilibrium. These layers are replaced with fresh ones at a given rate. Meanwhile material from the equilibrated ones are mixed back into the bulk metal and slag phases.

Equilibrium conditions are determined by first writing an expression for the total Gibbs free energy of the system (bubble, surrounding metal layer and reaction products) as a function of the moles of each compound in each phase in the equilibrium mixture. The set of the number moles of each compound present, which minimizes the Gibbs free energy function, is solved within the constraint of mass conservation. The solution to this problem is found by the use of the technique of undetermined Lagrange multipliers.

1 Application of Model

In this work an attempt has been made to apply the models of Ka[illegible], Ohno and Yamashita[illegible], with some modifications, to the AOD process at Hüttenwerke Krupp Stahl and Alloys. It is assumed that there are three distinct reaction zones, namely:-

i A [illegible] Reaction Zone;

ii A Bulk Slag/Metal Reaction Zone;

iii A Bulk Gas and Metal phase interface reaction zone.

i. Upper Reaction Zone

In this zone, a mixture of argon and inert gas enters, via the tuyeres, into the liquid metal, in the form of a [illegible] of a particular diameter.

As the [illegible] rises upwards relative to the surrounding liquid metal, a thermal metal phase boundary layer is established [illegible].

Assuming that a reaction can take place between elements such as C, Si, Mn and Fe dissolved in the metal phase at the metal/gas interface [illegible]. It is assumed that equilibrium is established at the interface between oxygen in the bubble, the reactive element in the metal phase and the corresponding oxide in the mixed oxide film that starts to form.

At the gas/metal interface, equilibrium is assumed to exist between CO and [illegible] in the bulk gas phase of the bubble and C dissolved in the metal phase at the metal/gas interface.

The model has been modified to allow for the oxidation of Fe and even Mn and Si as "tuning" options. However thermodynamic considerations suggest that if oxides of these elements are formed they are likely to be immediately reduced by more reactive

elements such as C, Si, Mn and Cr.

Because of the equilibrium conditions existing at the metal/gas interface, a concentration gradient of the reacting metal phase elements is established across the boundary layer surrounding each bubble. The relative formation rate of each oxide and CO is assumed to depend on the diffusion rate of the corresponding reacting metal phase element through the boundary layer.

The depletion of oxygen from the bubble proceeds at a very high rate because of the high temperature and high oxygen potential. A bubble is assumed to leave the tuyere reaction zone when its gaseous oxygen content becomes depleted.

It is assumed that equilibrium exists between nitrogen in the bulk gas phase of a bubble and nitrogen dissolved in the metal phase at the metal/gas interface. Thus a concentration gradient of nitrogen exists across the boundary layer surrounding a bubble. The depletion or accumulation rate of nitrogen in a bubble depends on its diffusion rate through the boundary layer.

1.3.2 Rising Bubble Reaction Zone

The Rising Bubble Reaction Zone is assumed to extend from the end of the Tuyere Reaction Zone to the slag/metal interface of the bulk slag phase floating on top of the liquid metal.

As a bubble enters the Rising Bubble Reaction Zone, the oxide mixture (ie. slag) contained within is assumed to disengage as a single spherical droplet. The bubble and its associated oxide droplet continue to rise up in close association with one another in a plume of liquid metal and other entrained bubbles and oxide droplets.

Boundary layers of stagnant liquid metal are assumed to surround each bubble and droplet as they float upwards relative to the liquid metal in the rising plume.

Carbon and oxygen dissolved in the metal phase react at the metal/gas interface to form CO in the gas phase. It is assumed that equilibrium exists, at the gas/metal interface of a bubble, between the following:-

(i) CO in the bulk gas phase;

(ii) C and O dissolved in the metal phase at the interface.

Diffusion of C and O takes place through the boundary layer due to the respective concentration gradients existing between the bulk liquid metal and the metal phase at the interface.

The decarburization or CO formation rate in a bubble depends on the mass transfer of C and O through the boundary layer surrounding it.

It is assumed that equilibrium exists, at the metal/oxide interface of an oxide droplet, between the following:-

(i) oxygen dissolved in the metal phase at the interface;

(ii) oxide with a high oxygen potential (eg. Cr_2O_3) at the oxide particle surface. As a simplifying assumption it is assumed that the surface concentration of the oxide is the same as its bulk concentration in the particle;

(iii) element (eg. Cr) dissolved in the metal phase at the interface. *As a simplifying assumption it is assumed* that the interfacial concentration of the element is the same as its concentration in the bulk liquid metal.

Oxygen is removed from the liquid metal of the rising plume by the decarburisation reaction taking place in a bubble. Thus, in addition to that in the boundary layer surrounding a bubble, an oxygen concentration gradient exists in the metal phase boundary layer surrounding an oxide droplet. Because of the lower oxygen potential in the bulk liquid metal (with respect to that existing at the oxide/metal interface), oxides at the particle surface dissociate.

The dissociation or reduction rate of the particle is dependent on oxygen mass transfer through the boundary layer surrounding it.

2.3.3 *Bulk Slag and Metal Phase Interface Reaction Zone*

Although the existence of this reaction zone is recognized, it has not been included in the model at this stage. In the model in its present form it is assumed that any metal oxides captured by the bulk slag phase no longer participate in any further reactions.

2. TUYERE ZONE REACTION MODEL

2.1 Qualitative Description of Model

It is postulated that as the mixture of oxygen and inert gas is blown through the tuyeres into the liquid metal, bubbles are formed. It is assumed that, once formed, they neither coalesce nor subdivide. Oxygen in these bubbles immediately reacts with C, Si, Mn, Cr, and Fe at the gas/metal interface. Oxides such as CO, SiO_2, MnO, Cr_2O_3 and FeO are produced.

In reality, elements such as Mo and Ni probably also react with oxygen to form oxides. However, because the free energies of formation of these oxides are substantially less negative than those discussed above, they are probably immediately reduced by elements having a much higher affinity for oxygen. The model does allow for the participation of these elements as an option for tuning the overall AOD model.

In line with other authors[1,2,3] it is assumed that the rate of formation of these oxides (and hence the composition of the oxide mixture leaving the tuyere reaction zone) is dependent on the rate of mass transport of the oxide forming elements through the metal phase to the gas/metal interface of the bubbles.

Thus, in the formulation of the model, it is assumed that mass transfer takes place as a result of diffusion of the reacting species in the metal phase through a metal phase boundary layer surrounding each bubble. The driving force for this diffusion process is the concentration gradient of each diffusing element that exists between the bulk liquid metal phase and the gas/metal interface of a bubble. The concentration of a reacting element at this interface is determined by the thermodynamic equilibrium assumed to exist between it, its equivalent oxide and oxygen in the bubble.

Since the thickness of this boundary layer is not known, the Higbie Surface Renewal Model[4,5] is used to estimate the mass transfer coefficients for the various reacting elements.

In addition to the reactions between oxygen and metal phase elements, the tuyere reaction model allows for the mass transfer of nitrogen through the metal phase boundary layer surrounding a bubble. This is because nitrogen is one of the inert gases used in the AOD process for reasons of economics.

Nitrogen is fairly soluble in liquid iron and its alloys[6]. This is in contrast to argon which appears, from lack of references to the contrary in the literature, to be virtually insoluble for all practical purposes.

The mass transfer rate of nitrogen is also assumed to be diffusion

controlled. The *driving force* for diffusion is a concentration gradient through the boundary layer between the bulk liqid metal and the gas/metal interface of the bubble. Nitrogen dissolved in the metal phase at the gas/metal interface is assumed to be in thermodynamic equilibrium with the partial pressure of nitrogen in the bubble.

It is documented in the literature[1,2] that surface active elements such as oxygen and sulphur reduce the mass transfer rate of nitrogen across the gas/metal interface. The overall nitrogen mass transfer coefficient is derived by combining the Higbie Surface *Renewal* Model mass transfer coefficient for the boundary layer with the mass transfer coefficient for the layer rich in surface-active agents.

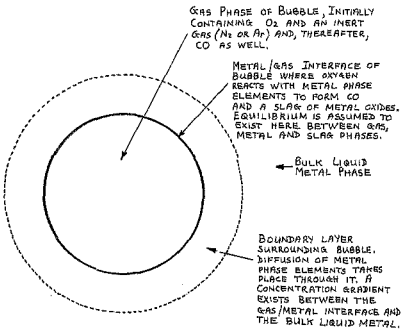


Figure 2.1: Schematic representation of the Tuyere Reaction Model

2.2 Mathematical Description of the Model

2.2.1 Bubble Formation at the Tuyeres

As the mixture of oxygen and inert gas leaves the tuyeres and enters the liquid metal, it is assumed to heat up virtually instantaneously to the temperature of the bath and to form discrete bubbles. The diameter $d_{bub}(0)$ of the bubbles that are initially formed is one of the parameters of the ACD model that may be varied for the purpose of "tuning" it to fit observed plant data.

The rate of bubble formation n_{bub} is given by:-

$$n_{bub} = Q^*/V_{bub}(0) \qquad (2.1)$$

where the volume $V_{bub}(0)$ of an individual bubble of diameter $d_{bub}(0)$ is given by:-

$$V_{bub}(0) = (\pi/6)*d_{bub}(0)^3 \qquad (2.2)$$

and the volumetric flow rate Q^* of the gas mixture entering the bath at tuyere level pressure P_{TUY} and bath temperature T_B is given by:-

$$Q^* = Q*T_B/(273.15*P_{TUY}) \qquad (2.3)$$

Note that Q is the total volumetric flow rate of gases being supplied to the tuyeres at standard temperature and pressure.

The initial flowrate of the j'th gas (where j>1) in the bubbles formed at the tuyeres is given by:-

$$N'_{mol,j}(0) = G_{r,j} \qquad (2.4)$$

where $G_{r,j}$ is the flowrate (kgmol/sec) of the j'th gas supplied to the tuyeres.

It is assumed that the initial flowrate of carbon monoxide $N'_{CO}(0)$ ($=N'_{mol,1}(0)$) is zero.

The ferrostatic pressure P_{TUY} (atm) at the tuyere level in the bath is given by:-

$$P_{TUY} = (P_{ATM}+(\rho*x_{TUY}+\rho_{M,S}*x_{M,S})*G)/101325 \qquad (2.5.1)$$

The calculation of x_{TUY}, the depth of the tuyeres below the slag/metal interface and $x_{M,S}$, the thickness of the slag layer is described in chapter 5. The calculation of the metal and slag densities ρ and $\rho_{M,S}$ is also discussed in chapter 5.

For a bubble of age t at an arbitrary distance h(t) above the tuyeres, the ferrostatic pressure P(t) is given by:-

$$P(t) = (P_{atm}+(\rho f*(x_{Tuy}-h(t))+\rho_{M.e}*x_{M.e})*g)/101325 \qquad (2.5.2)$$

2.2.2 Thermodynamic Equilibrium at the Metal/Gas Interface of the Bubbles

As each oxygen containing bubble moves from the tuyeres into the liquid metal, oxides and carbon monoxide begin to form at the gas/metal interface according to the following reactions:-

$$x\,[M] + y/2\ O_2 \Leftrightarrow M_xO_y \qquad (2.6)$$

$$[C] + y/2\ O_2 \Leftrightarrow CO \qquad (2.7)$$

In the case of nitrogen, dissolution (or evolution) takes place at the gas/metal interface:-

$$1/2\ N_2 \Leftrightarrow [N] \qquad (2.8)$$

It is assumed that thermodynamic equilibrium exists between oxygen and carbon monoxide in the bulk gas phase of the bubble, metal oxides in the oxide mixture forming at the gas/metal interface and carbon and other metallic components present in the metal phase at the gas/metal interface.

Thus, in the case of the formation of the j'th oxide M_xO_y, the equilibrium constant K_j is given by:-

$$K_j = a_{M_xO_y}(t)/((a_{T.j}(t)*\%x_{T.j})^x*(P_{CO}(t)*\%(z_{T.j}/2))) \qquad (2.9)$$

Similarly, it is assumed that thermodynamic equilibrium exists between nitrogen gas in the bubble and dissolved nitrogen in the metal phase at the metal/gas interface.

Thus, the the equilibrium constant K_n for the nitrogen dissolution reaction, represented by equation 2.8, is given by:-

$$K_n = \%N(t)*f_N/(P_{N2}(t))^{1/2} \qquad (2.10)$$

where $\%N(t)$ is the concentration (%) of nitrogen in the metal phase at the gas/metal interface and f_N is the activity coefficient.

The equilibrium constant K_j is calculated from the free energy of formation of the respective oxides:-

$$K_j = Exp(-\Delta G_j/(R*T_b)) \qquad (2.11)$$

In the case of nitrogen dissolution, the equilibrium constant K_n is calculated from the standard free energy of formation of a 1% solution of nitrogen in liquid iron (ref. 7):-

$$K_m = \exp(-(3596+23.69T_b)/(RT_b)) \qquad (2.12)$$

For elements in the metal phase displaying Raoultian behaviour, the standard free energy of formation ΔG°_j of the j'th oxide M_xO_y is given by:-

$$\Delta G^\circ_j = A_j + B_j T \qquad (2.13.1)$$

Values for the co-efficients A_j and B_j are taken from reference 7.

For elements in the metal phase displaying Henrian behaviour (ie. 1% solution standard state), the standard free energy of formation ΔG°_j of the j'th oxide M_xO_y is given by:-

$$\Delta G^\circ_j = A_j - \underline{A}_j x_{M,j} + (B_j - \underline{B}_j x_{M,j})T = \Delta G^\circ_j - x_{M,j}\underline{\Delta F}^\circ_j \qquad (2.13.2)$$

Values for the co-efficients $\underline{A}_j$ and $\underline{B}_j$ (used for calculating the standard free energy $\underline{\Delta F}^\circ_j$ of a 1% solution of the j'th element in liquid iron) are taken from reference 7.

Initially the activity of each oxide that starts to appear in a newly formed bubble is assumed to equal one (this excludes CO for which j=1 in the subscript numbering system being used). However, as the oxidation reactions proceed, it is assumed that an oxide mixture forms at the gas/metal interface. The activity of each oxide in this mixture is assumed to be equal its molar fraction.

Thus the activity $a_{ox,j}(t)$ of the j'th oxide MxOy (for j>1) is given by (assuming an ideal solution):-

$$a_{ox,j}(t) = X_{ox,j}(t) = N'_{ox,j}(t)/\sum_{k=2}^{n} N'_{ox,k}(t) \qquad (2.14)$$

Initially the partial pressure $P_{co}(0)$ of carbon *monoxide* in a newly formed bubble is assumed to be equal to zero. As the formation of carbon monoxide proceeds, $P_{co}(t)$ is given by the product of the ferrostatic pressure and the molar fraction of carbon monoxide in the gas mixture in the bubble:-

$$P_{co}(t) = P(t)*N'_{co}(t)/N'_{gas}(t) \qquad (2.15)$$

Initially the partial pressures of oxygen and nitrogen in a newly formed bubble are given by the product of the ferrostatic pressure at the tuyeres and the molar fractions of these gases in the bubble:-

$$P_{o2}(0) = P_{tuy}*N'_{o2}(0)/N'_{gas}(0) \qquad (2.16)$$

$$P_{n2}(0) = P_{tuy}*N'_{n2}(0)/N'_{gas}(0) \qquad (2.17)$$

As oxygen is depleted from the gas phase of the bubble, its partial pressure $P_{o2}(t)$ is given by the product of the molar fraction of oxygen in the gas and the ferrostatic pressure:-

$$P_{N2}(t) = P(t)*N'_{N2}(t)/N'_{GAS}(t) \qquad (2.18)$$

In the case of nitrogen, depletion or accumulation can take place in a bubble. Its partial pressure $P_{N2}(t)$ is similarly given by:-

$$P_{N2}(t) = P(t)*N'_{N2}(t)/N'_{GAS}(t) \qquad (2.19)$$

Concentrations of each element in the bulk liquid metal are given by the product of the metal molar density ρ' and the molar fraction of the element.

The concentration of each element in the metal phase at the gas/metal interface is calculated from the equilibrium conditions discussed above.

It can be shown that the molar fraction $X_{I,j}(t)$ of the j'th element (displaying Henrian behaviour) in the metal phase at the metal/gas interface is given by:-

$$X_{I,j}(t) = (a_{I,j}(t)/f_j)*\rho/(M_j*100*\rho') \qquad (2.20.1)$$

In the case of elements displaying Raoultian behaviour:-

$$X_{I,j}(t) = a_{I,j}(t) \qquad (2.20.2)$$

In both cases:-

$$a_{I,j}(t) = (X_{BM,j}(t)/(K_j*P_{GS}(t)**(z_{I,j}/2)))**(1/z_{I,j}) \qquad (2.21)$$

In the case of nitrogen, $\%N_I(t)$, the equilibrium concentration (%) in the metal phase at the metal/gas interface, is given by:-

$$\%N_I(t) = K_N*(P_{N2}(t))^{1/2}/f_N \qquad (2.22)$$

2.2.3 Kinetics of Oxide Formation and other Mass Transfer Processes in the Bubbles

The rate at which carbon monoxide and the various metallic oxides form is assumed to depend on the rates at which carbon and the other metallic phase elements diffuse through the metallic phase boundary layer surrounding a bubble. A concentration gradient of each diffusing element is assumed to exist between the bulk liquid metal and the gas/metal interface.

Thus the molar flux $J_k(t)$ of the k'th element through the boundary layer is given by:-

$$J_k(t) = k_{DIFF,k}(t)*\rho'*(X_{MET,k}-X_{I,k}(t)) \qquad (2.23)$$

The calculation of the mass transfer coefficient $k_{DIFF,k}(t)$ is discussed separately in chapter 3.

It is thus implicitly assumed that mass transfer rather than interfacial reaction rates is the overall rate controlling factor.

This assumption is made on the basis of the high temperatures existing in the AOD process and is in line with similar assumptions by other authors[1,2,3].

It is also assumed that the mass transfer rates of CO, O_2 and N_2 through a gas phase boundary layer at the gas-metal interface are sufficiently high (in comparison to the mass transfer rates of the reacting elements through the metal phase boundary layer) that they can be ignored.

It is assumed that no hold-up of bubbles occurs in any horizontal plane in the metal bath at or above the tuyere level. Furthermore it is assumed that bubbles do not coalesce or subdivide. The bubbles that form at the tuyeres rise up through the tuyere reaction zone. As they rise the oxidation reactions discussed above proceed until the oxygen content has been virtually depleted. Therefore it is apparent that there must be an associated accumulation of oxides and carbon monoxide in the bubbles as they rise through the tuyere reaction zone.

A bubble will rise through an incremental vertical distance dh in the incremental time dt. Thus the instantaneous rising velocity $u_{BUB}(h)$ of a bubble at a particular position in the tuyere reaction zone is given by:-

$$u_{BUB}(h) = dh/dt = -dx/dt \qquad (2.24)$$

Note that h is the vertical distance between the tuyeres and a bubble and x is the distance between a bubble and the slag/metal interface.

The calculation of the rising velocity $u_{BUB}(h)$ is discussed in chapter 3.

The rate of increase of the integrated vertical flowrate of the j'th oxide (including CO) is given by:-

$$d(N'_{ox,j}(h))/dh = (1/u_{BUB}(h))x k_{BUB,j}(h) x n_{BUB} x A_{BUB}(h) x \rho'\%(X_{MET,j}-X_{i,j}(h))/z_{z,i} \qquad (2.25.1)$$

This can be expressed in terms of the tuyere reaction time t (ie. the time that it takes for oxygen depletion of a bubble in the tuyere reaction zone):-

$$d(N'_{ox,j}(t))/dt = k_{BUB,j}(t) x n_{BUB} x A_{BUB}(t) x \rho'\%(X_{MET,j}-X_{i,j}(t))/z_{z,i} \qquad (2.25.2)$$

The rate of decrease of the integrated vertical flowrate of oxygen is given by a mass balance expressed as follows:-

$$d(N'_{O2}(h))/dh = -\sum_{j=1}^{x}[(d(N'_{ox,j}(h))/dh) x z_{y,j}/2] \qquad (2.26.1)$$

Similarly, in terms of the tuyere reaction time t:-

$$d(N'_{O2}(t))/dt = \sum_{j=1}^{n} [(d(N'_{O2,j}(t))/dt)*z_{T,j}/2] \qquad (2.26.2)$$

The rate of change of the integrated vertical flowrate of nitrogen is given by:-

$$d(N'_{N2}(h))/dh = (1/u_{bve}(h))*k_m(h)*n_{bve}*A_{bve}(h)*p_g*(\%\bar{N}-\%\bar{N}_i(h))/(M_w*200) \quad (2.27.1)$$

Similarly, in terms of the tuyere reaction time t:-

$$dN'_{N2}/dt = k_m(t)*n_{bve}*A_{bve}(t)*p_g*(\%\bar{N}-\%\bar{N}_i(t))/(M_w*200) \qquad (2.27.2)$$

The calculation of the mass transfer coefficients ($k_{bve,j}(t)$) and the bubble coefficients (f_i and f_s) are dealt with in chapter 3 and appendix respectively.

2.2.4 Numerical Integration of the Model

The solution of the set of simultaneous differential equations represented by 2.24, 2.25.2, 2.26.2 and 2.27.2 is achieved by the use of a numerical Runge-Kutta or Bulirsch-Stoer integration method[4] with automatic step length control.

The integration is performed over successive equal length time (ie. incremental bubble age) intervals. At the end of each interval the oxygen content of the bubbles is checked. Unless the criterion for oxygen depletion has been met, the integration continues over the next time interval.

The criterion for the termination of integration (and a bubble leaving the tuyere reaction zone) is when the oxygen content is less than or equal to some very small arbitrary percentage (eg. 0,001%) of the initial content when the bubble was formed.

It is assumed that the quantity of free oxygen remaining in a bubble leaving the tuyere reaction zone is so small that it can be approximated to zero. The converse of this is that all the oxygen inside a bubble when it was formed leaves the tuyere reaction zone in the form of CO and other oxides. This is a reasonable assumption as thermodynamic equilibrium calculations[7] show that the partial pressure of oxygen in equilibrium with oxides such as Cr_2O_3 at the temperatures applicable to the AOD process is very low indeed.

On leaving the tuyere reaction zone, the oxides that were formed inside a bubble are assumed to disengage themselves from it as a spherical particle or droplet. Thus it is assumed that each bubble gives birth to a single oxide particle. These bubbles and oxide particles are then assumed to rise up, in close association with one another in a plume, through the rising bubble reaction zone discussed in chapter 4.

2.3 Results

Typical calculated oxide and gas flowrates in the bubbles as a function of bubble age are presented in Figures 2.2 to 2.5.

In Figures 2.2 and 2.3 the gas and oxide flowrates in the tuyere reaction zone, as a function of bubble age, are shown. In the simulation, an initial 15mm bubble diameter was used and the liquid metal composition is representative of a typical 304 type steel as initially charged into the AOD vessel. The carbon concentration and temperature are representative of the conditions at the start of an initial 3:1 blow (ie. $45m^3O_2min^{-1}:15m^3N_2min^{-1}$).

In the simulation, Ni and Fe have been allowed to be participating elements in addition to C, Si, Mn and Cr.

It can be seen that the tuyere reaction reaches completion extremely rapidly with the free oxygen content of a bubble being depleted within about $8\times10^{-4}s$.

The approximately linear flowrate trajectories suggest that the computational overhead of the tuyere reaction model integration could be significantly reduced. This could be achieved by assuming that the flowrates of the various oxides at the end of the tuyere reaction zone are proportional to the flowrates at the start and applying conservation of mass in respect of oxygen.

The rate of change of the nitrogen flowrate is negligable and could be ignored.

The rate of increase of the CO flowrate suggests that significant decarburization takes place in the tuyere reaction zone, particularly with high carbon levels in the bath.

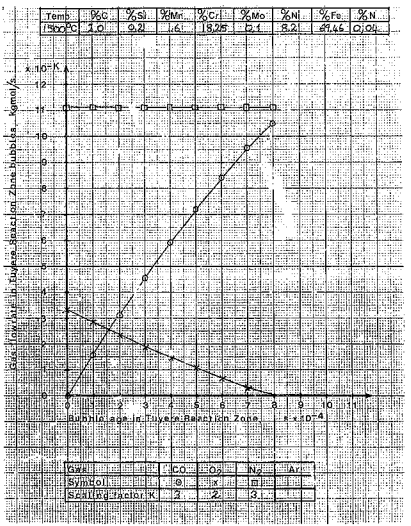


Figure 2.2: Typical Tuyere Reaction Model data in respect of gas flowrates resulting from a 3:1 O_2:N_2 blowing ratio and an initial 15mm diameter bubble

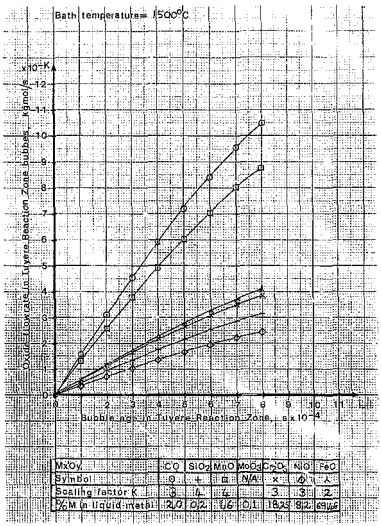


Figure 2.3: Typical Tuyere Reaction Model data in respect of oxide flowrates resulting from a 3:1 O_2:N_2 blowing ratio and an initial 15mm diameter bubble

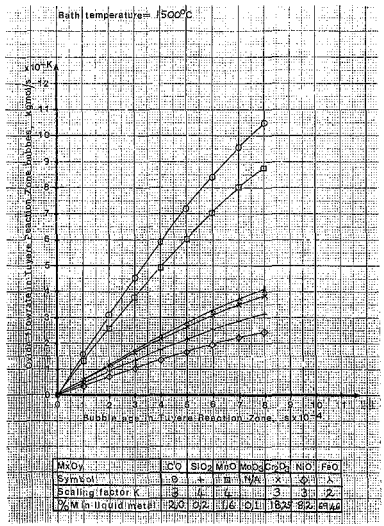


Figure 2.3: Typical Tuyere Reaction Model data in respect of oxide flowrates resulting from a 3:1 O_2:N_2 blowing ratio and an initial 15mm diameter bubble

In figures 2.4 and 2.5 bath conditions at the start of a 1:1 blow (ie. $30m^3O_2min^{-1}:30m^3N_2min^{-1}$) were simulated. Again an arbitrary 15mm initial bubble diameter was selected.

The plateaus evident between 5 and 6×10^{-4}s are purely a function of the integrator integrating over successive 1×10^{-4}'s intervals (as specified by the user) before the next test for oxygen depletion of the bubbles is performed. Thus oxygen depletion was achieved in just over 5×10^{-4}s.

The reduction in the time for free oxygen depletion to occur is largely a function of the reduced initial oxygen flowrate. The temperature dependence of the diffusivities of individual elements has not been taken into account at the present stage of the model development.

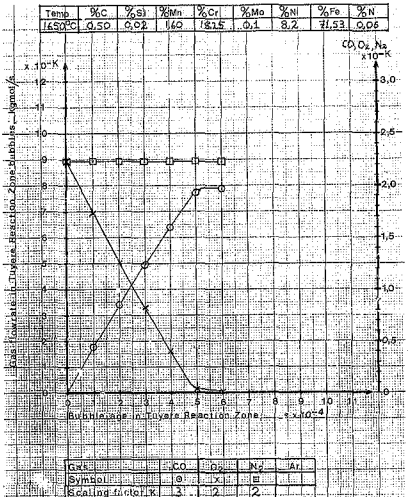


Figure 2.4: Typical Tuyere Reaction Model data in respect of gas flowrates resulting from a 1:1 O_2:N_2 blowing ratio and an initial 15mm diameter bubble

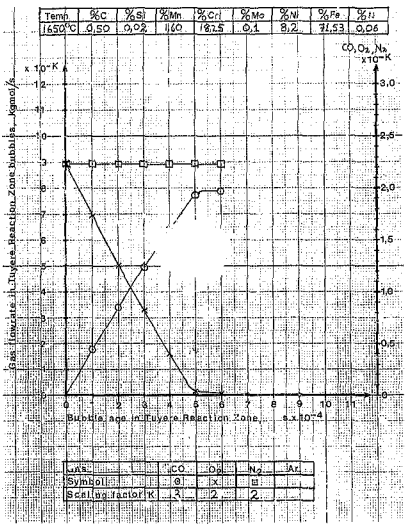


Figure 2.4: Typical Tuyere Reaction Model data in respect of gas flowrates resulting from a 1:1 O_2:N_2 blowing ratio and an initial 15mm diameter bubble

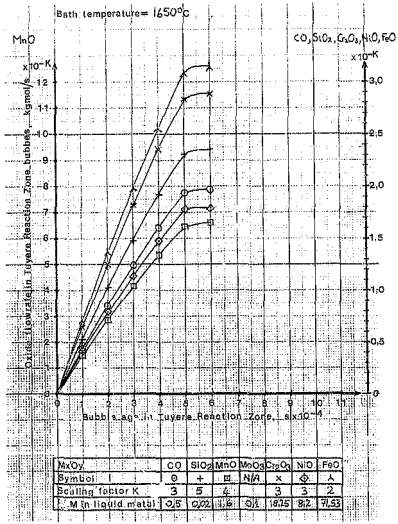


Figure 2.5: Typical Tuyere Reaction Model data in respect of oxide flowrates resulting from a 1:1 O_2:E, blowing ratio and an initial 15mm diameter bubble

3 MASS TRANSFER TO RISING BUBBLES IN TUYERE AND RISING BUBBLE REACTION ZONES

3.1 Introduction

As was discussed in chapter 2, the rate of mass transfer to and from a bubble is assumed to depend on the diffusion of the reacting elements through a metal phase boundary layer surrounding it. The driving force for this diffusion is a concentration gradient that exists across the boundary layer.

Since the thickness of this boundary layer is not known, it is necessary to use models such as the Higbie Surface Renewal Model[8] or other semi-empirical and empirical correlations in order to estimate approximate mass transfer coefficients for the reacting elements.

One of the important variables that is needed to estimate the mass transfer coefficients is the rising velocity of a bubble, which in turn is a function of its diameter. This is discussed in more detail in the next section.

In the case of the mass transfer of nitrogen it was pointed out in chapter 2 that the presence of surface active elements such as oxygen and sulphur in the liquid metal have to be taken into consideration. In the literature[9,2] it is documented that these elements reduce the mass transfer rate of nitrogen across the gas/metal interface of a bubble.

Other variables that are needed for the estimation of mass transfer coefficients are the diffusivities of the respective elements in the liquid metal. There appears to be a paucity of diffusivity data in the literature relating to the multicomponent systems encountered in the stainless steel making environment. Therefore, as an approximation, the diffusivities in pure liquid iron at 1650°C are used (see table 3.1).

Element	Diffusivity (m^2/s)	Element	Diffusivity (m^2/s)	Element	Diffusivity (m^2/s)
C	4,13E-8	Ni	#,32E-8	S	#,59E-8
Si	2,01E-8	Fe	1,12E-8	P	1,00E-8
Mn	#,94E-8	Ti	#,59E-8	N	#,79E-8
Cr	#,58E-8	Al	##,59E-8	O	#,52E-8
Mo	##,59E-8	Cu	##,59E-8		

Estimate - no available data

Table 3.1: Diffusivities of elements in liquid iron at 1650°C

The data presented in table 3.1 is taken from reference 1 or estimated from Fig 13.17 in reference 14. The Arrhenius type temperature dependence of diffusivities is not taken into account in the model although it would be a simple matter to do so if required at a later stage

3.2 Mathematical Description

The Higbie Surface Renewal Model is used to estimate the mass transfer coefficients. In this model, as it applies to a rising bubble, *it is postulated that a fluid element representing* the composition of the bulk liquid metal comes in contact with the gas/metal interface of a bubble for a certain time period. During this contact time unsteady state diffusion occurs between the fluid element and the gas/metal interface. At the end of this time period, the fluid element *is left behind and is replaced by a* new fluid element from the bulk liquid metal as the bubble floats upwards.

For a bubble at depth x below the slag/metal interface it can be shown[4] that the mass transfer coefficient $k_{mtb,k}(x)$ for the k'th diffusing element is given by:-

$$k_{mtb,k}(x) = 2*(D_x/(\Pi*t_{e,mtb}(x)))^{1/2} \qquad (3.1)$$

where the parameter $t_{e,mtb}(x)$ is the contact time.

For a bubble of diameter $d_{mtb}(x)$ (at a depth x below the slag/metal interface), rising at a velocity $u_{mtb}(x)$, the contact time can be approximated as:-

$$t_{e,mtb}(x) = d_{mtb}(x)/u_{mtb}(x) \qquad (3.2)$$

However, both the diameter and the rising velocity are functions of the *ferrostatic pressure*, the temperature and the quantity of gas in the bubble.

The ferrostatic pressure P(x) (in atmospheres) in a bubble at a depth x below the metal/slag interface is given by:-

$$P(x) = (P_{atm}*(p_{atm}*x+p_{mtm}*x_{slg})*G)/101325 \qquad (3.3)$$

The quantity of gas in a bubble is given by the molar gas flowrate divided by the bubble formation rate (since it assumed that bubbles do not coalesce or subdivide). Therefore, the diameter $d_{mtb}(x)$ of a bubble (as a function of the ferrostatic pressure P(x), the total molar gas flowrate $N'_{mtb}(x)$ and the bubble formation rate r_{mtb}) is given by:-

$$d_{mtb}(x) = (6*N'_{mtb}(x)*R*T_b/(\Pi*n_{mtb}*273.15*P(x)))^{1/3} \qquad (3.4)$$

As an approximation, it is assumed that models for single rising bubbles may be applied to determine the rising velocity.

It is documented in the literature that the behaviour of single rising bubbles can be classified into four regions:-

(i) Very small bubbles with diameters less than about 2mm behave as rigid spheres obeying Stoke's law and rise with a terminal velocity given by:-

$$u_{bm} = G(\rho - \rho_{mix})gd_{mm}^2/(18\mu) \qquad (3.5.1)$$

Since $\rho \gg \rho_{mix}$, equation 3.5.1 may be approximated as:-

$$u_{bm} = G\rho g d_{mm}^2/(18\mu) \qquad (3.5.2)$$

(ii) Intermediate sized bubbles where bubbles are still spherical and rise in a rectilinear path. The equivalent diameter of these bubbles is approximately 2-4mm. However, their rising velocity may be as much as 50% greater than that predicted by equation 3.5.2 because of gas circulation inside the bubble that results in the movement of the liquid interface and a reduction of the drag force.

(iii) Spheroidal and ellipsoidal bubbles that rise in a spiral path. The equivalent diameter of these bubbles is approximately in the range 5-9mm.

(iv) Spherical cap bubbles of equivalent diameter greater than approximately 10mm. An equation describing the rising velocity u_{bm} of such bubbles was derived by Davies and Taylor, where:-

$$u_{bm} = 1.02(0.5gd_{mm}/2)^{1/2} \qquad (3.6)$$

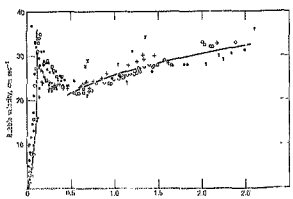


Figure 3.1. Rising velocity of single bubbles in water

From Figure 3.1 (reproduced from Fig 19.2.5 in reference 6), the Stoke's equation 3.5.2 is assumed to apply for bubbles with a diameter up to 1mm. For bubbles of equivalent diameter greater than 10mm, the Davies and Taylor equation 3.5.1 is assumed to apply. For bubble diameters in the range 1-10mm, the rising velocity is determined by linear interpolation:-

$$u_{bub} = (d_{bub}-0,001)*((Y2-Y1)/(0,01-0,001))+Y1 \qquad (3.7)$$

where:-

$$Y1 = G*\rho*0,001^2/(18*\mu) \qquad (3.5.1)$$

and:-

$$Y2 = 1,02*(G*0,01/2)^{1/2} \qquad (3.5.2)$$

The mass transfer coefficient $k_{bub,i}(x)$ for a bubble at a depth x below the metal/slag interface is given by combining equations 3.1 and 3.2:-

$$k_{bub,i}(x) = 2*(D_i*u_{bub}(x)/(\Pi*d_{bub}(x)))^{1/2} \qquad (3.9)$$

In the case of nitrogen, the boundary layer mass transfer coefficient is given by:-

$$k'_n(x) = 2*(D_n \quad (x)/(\Pi*d_{bub}(x)))^{1/2} \qquad (3.10)$$

The mass transfer coefficient for the gas/metal interface poisoned by *S* and *O* is given by the empirical correlation[2]:-

$$k'_n = -6,27E-4+8,34E-7*(457-562*Ln([\%O]+0,0783*[\%S]^{1/2})) \qquad (3.11)$$

It is assumed, for lack of evidence to the contrary in the reference, that [%O] and [%S] are the concentrations of oxygen and sulphur in the bulk liquid metal.

The overall nitrogen mass transfer coefficient $k_n(x)$ is given by:-

$$k_n(x) = 1/(1/k'_n(x)+1/k*_n) \qquad (3.12)$$

4 RISING BUBBLE REACTION MODEL

4.1 Qualitative Description of Model

4.1.1 Purpose of model

The purpose of the rising bubble reaction model is to determine the flowrates of CO, N_2 and metal oxides M_xO_y leaving the metal bath. These variables are subsequently used in the the overall heat and mass balances needed to calculate the temperature and composition trajectories of the metal and slag in the AOD vessel.

4.1.2 Rising bubbly reaction zone

The rising bubble reaction zone is considered to be the plume of bubbles, associated liquid metal and oxide particles rising up through the liquid metal bath. It extends from the point in the liquid metal where a bubble leaves the tuyere reaction zone to where it intersects the slag/metal interface. The departure point from the tuyere reaction zone is an abitrary position where the oxygen content of the bubble has become depleted to a negligible quantity.

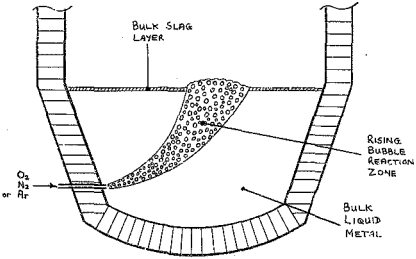


Figure 4.1: Schematic representation of the Rising Bubble Reaction Zone.

4.1.3 Oxide particle formation

As a bubble leaves the tuyere reaction zone, the metal oxide mixture that has formed within disengages into the surrounding liquid metal phase as a spherical particle. A single oxide particle is assumed to form per bubble. Subsequently each particle neither subdivides nor coalesces with others.

4.1.4 Passage of bubbles and oxide particles through the rising bubble reaction zone

As bubbles and oxide particles float up through the rising bubble reaction zone, carbon and oxygen dissolved in the liquid metal react at the metal/gas interface of the bubbles to form carbon monoxide:-

$$[C] + [O] \Leftrightarrow CO \qquad (4.1)$$

This results in an accumulation of CO in the bubbles and a lowering of the oxygen (and carbon) potential of the liquid metal. As the oxygen potential of the liquid metal is lowered, metal oxides in the oxide particles dissociate to re-establish it:-

$$M_xO_y \Leftrightarrow x[M] + y[O] \qquad (4.2)$$

Thus oxygen for the decarburization reaction is indirectly provided by the dissociation of metal oxides in the oxide particles.

There is a simultaneous depletion of reducible oxides in the oxide particles due to their reduction by silicon dissolved in the liquid metal:-

$$[Si] + 2/y\ M_xO_y \Leftrightarrow SiO_2 + 2x/y\ [M] \qquad (4.3)$$

This results in an accumulation of SiO_2 in the particles.

Nitrogen, being soluble in the liquid metal, may accumulate in or be depleted from the bubbles, depending for example, on whether argon or nitrogen is being used as the inert gas:-

$$N_2 \Leftrightarrow 2[N] \qquad (4.4)$$

The model takes into account the the change in bubble size associated with the decrease in ferrostatic pressure and the changes in the gas composition as the bubble floats upwards. The associated effects on metal/gas interface equilibria and bubble boundary layer mass transfer rates are also considered.

The change in oxide particle size, associated with oxide reduction and SiO_2 accumulation, is accounted for, as are the associated effects on boundary layer mass transfer rates.

The oxide particles that reach the slag/metal interface at the top

of the metal bath are captured by the slag phase. The gas content of the bubbles passes through the slag layer without further reaction and ultimately escapes to the atmosphere via the vessel mouth.

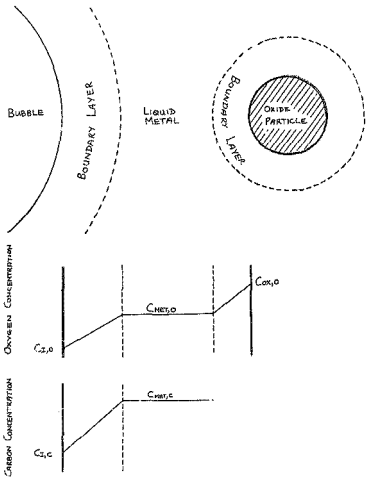


Figure 4.2: Schematic representation of a bubble, an oxide particle and the associated boundary layers and concentration gradients in the Rising Bubble Reaction Zone.

4.1.5 Decarburization reaction at metal/gas interface of bubble

There is no reference to CO being soluble in liquid iron in the literature surveyed. It is assumed[1,2,3] that carbon and oxygen diffuse through the metal phase boundary layer surrounding a bubble as it rises upwards through the rising bubble reaction zone. They react at the metal/gas interface to form carbon monoxide according to the decarburization reaction:-

$$[C] + [O] \Leftrightarrow CO \qquad (4.1)$$

It is assumed[1,2,3] that equilibrium exists between carbon and oxygen dissolved in the metal phase at the metal/gas interface and carbon monoxide in the gas phase.

It is assumed that mass transfer of CO through the gas phase boundary layer at the gas/metal interface is not rate determining. Thus, as a simplifying approximation, it is assumed that the partial pressure of CO at the interface equals that in the bulk gas phase of the bubble.

The partial pressure of CO in a bubble is a function of the gas composition and the vertical distance above the tuyeres (ie. the ferrostatic pressure).

4.1.6 Mass transfer of carbon and oxygen through boundary layer surrounding bubbles

The concentration gradients of carbon and oxygen between the bulk liquid metal (in the plume of rising bubbles, liquid metal and oxide particles) and the metal/gas interface is the driving force for the diffusion of these elements through the metal phase boundary layer surrounding a bubble. Refer to figure 4.2 and figure A1 in appendix A.

The fluxes of carbon and oxygen through the boundary layer are given by:-

$$J_c = k_{mtl,c} * (C_{met,c} - C_{i,c}) \qquad (4.5)$$

$$J_o = k_{mtl,o} * (C_{met,o} - C_{i,o}) \qquad (4.6)$$

The mass transfer coefficients for carbon and oxygen are estimated using the Higbie Surface Renewal Model discussed in chapters 2 and 3:-

$$k_{mtl,c} = 2 * (D_c / (\Pi * t_{e,bub}))^{1/2} \qquad (4.7)$$

$$k_{mtl,o} = 2 * (D_o / (\Pi * t_{e,bub}))^{1/2} \qquad (4.8)$$

4.1.7 Dissociation of reducible oxides in oxide particles

The source of oxygen for the decarburization reaction is the dissociation (ie. reduction) of metal oxides (MnO, Cr_2O_3, FeO, etc.) at the surface of the oxide particles:-

$$M_xO_y \leftrightharpoons x[M] + y[O] \qquad (4.2)$$

It is assumed that equilibrium exists between oxygen (O) and the metal element (M) in the metal phase at the oxide/metal interface and the oxide M_xO_y in the particle surface. Thus it is assumed that this dissociation reaction is not rate controlling.

4.1.8 Mass transfer of oxygen through boundary layer surrounding oxide particles

A metal phase boundary layer is also assumed to exist around an oxide particle as it floats up through the liquid metal. Oxygen diffuses from the oxide particle surface, through the boundary layer to the bulk metal phase. The oxygen concentration gradient between the metal/oxide interface and the bulk liquid metal provides the driving force for this diffusion process.

The flux of oxygen through the boundary layer is given by:-

$$J_o = k_{o,m}\rho(C_{o,s}-C_{o,r,m}) \qquad (4.9)$$

The oxygen mass transfer coefficient is estimated using the Higbie Surface Renewal Model:-

$$k_{o,m} = 2\pi(D_o/(TT\pi t_{s,m}))^{1/2} \qquad (4.10)$$

4.1.9 Coupling of oxygen mass transfer through oxide particle and bubble boundary layers

During the early stages of the model development the oxygen diffusion processes through the oxide particle and bubble boundary layers were not coupled. The oxygen concentration in the bulk liquid metal was assumed to be uniform throughout the bath at any time. The time dependence of this concentration was dependent on an oxygen mass balance. However this led to serious instability problems with the numerical integration procedure used at the time (prior to the much later adoption of more sophisticated integration techniques[19]).

In an attempt to overcome this problem, the mass transfer of oxygen through the oxide particle boundary layer was directly coupled to that through the bubble boundary layer. The physical implication of this simplifying assumption is that an oxide particle (although disengaged from its corresponding bubble) rises up, together with liquid metal, in "close association" with a bubble. It also implies that the oxygen concentration in the bulk liquid metal associated with the rising plume of bubbles and oxide

particles varies with vertical position. This rather artificial approach to solving what was essentially a numerical analysis problem is recognized as a weakness in the model in its present form.

In the model the decarburization rate is a function of the mass transfer rates of oxygen and carbon through the bubble boundary layer and oxygen through the oxide particle boundary layer.

4.1.10 Mass transfer of nitrogen between bubbles and liquid metal

Nitrogen mass transfer also takes place between the bubble and the bulk liquid metal. It is assumed that equilibrium exists between nitrogen dissolved in the metal phase and nitrogen in the gas phase at the metal/gas interface:-

$$N_2 \ (=) \ 2[N] \qquad (4.4)$$

The concentration gradient of nitrogen between the bulk liquid metal and the metal/gas interface provides the driving force for diffusion through the bubble boundary layer. As discussed in chapters 2 & 3, the mass transfer rate of nitrogen is reduced by the presence of surface active elements such as sulphur and oxygen in the liquid metal.

The molar flux of nitrogen through the boundary layer is given by:-

$$J_N = K_{BUB,N}(C_{MET,N}-C_{i,N}) \qquad (4.11)$$

The nitrogen mass transfer coefficient is estimated using the Higbie Surface Renewal Model:-

$$K_{BUB,N} = 2*(D_N/(\Pi t_{e,BUB}))^{1/2} \qquad (4.12)$$

4.1.11 Reduction of oxide particles by silicon

The independent reduction of the oxide particles by silicon is allowed for in addition to the indirect reduction by carbon discussed in 4.1.6 and 4.1.7 above. The following equilibrium is assumed to exist at the metal/oxide interface:-

$$[Si] \quad 2/y \ M_xO_y \ (=) \ SiO_2 + 2x/y \ [M] \qquad (4.3)$$

4.1.... Mass transfer of silicon through boundary layer surrounding oxide particles

The rates of the reactions represented by equation (4.3) are assumed to depend on the diffusion of silicon through the metal phase boundary layer surrounding an oxide particle. The concentration gradient of silicon between the bulk liquid metal and the metal/oxide interface provides the driving force for this diffusion.

Thus the molar flux of silicon to the oxide particle surface is given by:-

$$J_{Si} = k_{m,Si} * (C_{met,Si} - C_{Si,s}) \qquad (4.13)$$

The silicon mass transfer coefficient is estimated using the Higbie Surface Renewal Model:-

$$k_{m,Si} = 2 * (D_{Si} / (\pi t_{s,ox}))^{1/2} \qquad (4.14)$$

4.1.13 Dissociation and reduction rates of individual oxides in oxide particles

For each of the overall carbon reduction reactions represented by:-

$$1/y\ M_xO_y + (C) \rightarrow CO + x/y\ [M] \qquad (4.15)$$

the individual oxygen flux originating from the dissociation of the oxide represented by M_xO_y is assumed[4.3] to be in proportion to the magnitude of the Gibb's free energy of the respective reduction reaction. Therefore, for example, the oxygen fluxes $J_{O,mxoy}$ for the dissociation of MnO, Cr_2O_3 and FeO are given by:-

$$J_{O,MnO} = J_O * \Delta G_{rmo,c} / \Sigma \Delta G_{rmoy,c} \qquad (4.16)$$

$$J_{O,Cr2O3} = J_O * \Delta G_{rCr2O3,c} / \Sigma \Delta G_{rmoy,c} \qquad (4.17)$$

$$J_{O,FeO} = J_O * \Delta G_{rFeO,c} / \Sigma \Delta G_{rmoy,c} \qquad (4.18)$$

Although not specifically indicated, the model can also allow for other oxides such as MoO_3 and NiO.

The total oxygen flux J_O is the sum of the individual oxygen fluxes:-

$$J_O = \sum_{x=0}^{n} J_{O,mxoy} \qquad (4.19)$$

Similarly, the individual fluxes of silicon to reduce each of the oxides represented by M_xO_y according to the reaction:-

$$2/y\ M_xO_y + [Si] \rightarrow SiO_2 + 2x/y\ [M] \qquad (4.20)$$

are assumed to be in proportion to the magnitude to the Gibb's free energy of the respective reduction reactions. Therefore, for example, the silicon fluxes $J_{Si,mxoy}$ for the reduction of MnO, Cr_2O_3 and FeO are given by:

$$J_{Si,MnO} = J_{Si} * \Delta G_{rmo,c} / \Sigma \Delta G_{rmoy,c} \qquad (4.21)$$

$$J_{Si,Cr2O3} = J_{Si} * \Delta G_{rCr2O3,c} / \Sigma \Delta G_{rmoy,c} \qquad (4.22)$$

$$J_{Si,Fe} = J_{Si} * \Delta G_{Fe,Si} / \sum \Delta G_{Me/Si} \quad (4.23)$$

The total silicon flux J_{Si} is the sum of the individual fluxes:-

$$J_{Si} = \sum_{i=0}^{n} J_{Si,MeOy} \quad (4.24)$$

In the model, reduction is allowed to take place if the free energy is negative. A simplification is made by not allowing a (reverse) reaction to take place if its free energy is positive or zero.

The fluxes of oxygen and silicon associated with the dissociation and reduction of individual oxides are used to calculate the resulting changes in the vertical oxide flowrates.

4.2 Mathematical Description of Model

4.2.1 Calculation of equilibrium constants

It is assumed that, during the time that a bubble and its associated oxide particle travels through the rising bubble reaction zone, the temperature of the bath remains constant. Therefore the equilibrium constants (functions of temperature) that are subsequently used repeatedly in the model are calculated at the outset.

The equilibrium constant K_{CO} for the decarburization reaction at the metal/gas bubble interface:-

$$[\%C] + [\%O] \Leftrightarrow CO \quad (4.25)$$

can be derived from basic thermodynamic principles and data[7] and is given by:-

$$K_{CO} = p^2/(\exp((16150+43.05*T_B)/(R*T_B))*(f_C*f_O*1.92E6)) \quad (4.26)$$

For elements displaying Henrian behaviour, the equilibrium constants $K_{Ox,i}$, for the dissociation reactions of their oxides at the metal/oxide interface:-

$$1/y\ M_xO_y \Leftrightarrow x/y\ [\%M] + [\%O] \quad (4.27.1)$$

are given by:-

$$K_{Ox,i} = \exp(-\Delta G^{\circ}_{Ox,i}/(R*T_B))$$

$$= \exp(-(-A_i/z_{v,i} + \Delta_0 + B_i*z_{v,i}/z_{v,i} + T_B*(-B_i/z_{v,i} + \Sigma_0 + \Sigma_i z_{v,i}/z_{v,i}))/(R*T_B)) \quad (4.28.1)$$

In the case of oxides of elements displaying Raoultian behaviour:-

$1/y\ M_xO_y$ (-) x/y [M] + [%O] (4.27.2)

we have:-

$K_{DISS.} = \text{Exp}(-\Delta G^{\circ}_{DISS.}/(R*T_s))$
$= \text{Exp}(-(-A_1/z_{v,1}+A_2+T_s*(-B_1/z_{v,1}+B_2))/(R*T_s))$ (4.28.2)

For the dissolution reaction of nitrogen at the metal/gas interface:-

$1/2N_2$ <=> [%N] (4.29)

the equilibrium constant K_N is given by:-

$K_N = \text{Exp}((-3568-23.89*T_s)/(R*T_s))$ (4.30)

4.2.2 Outline of procedure for calculating gas and oxide flowrates as functions of position

As bubbles float up through the rising bubble reaction zone, variables such as their diameter, surface area, gas content, gas partial pressures, rising velocity, fluxes of diffusing elements, etc. change continuously as indirect functions of distance below the slag/metal interface. This also applies to the oxide particles. These variables are used in the formulation of the simultaneous first order differential equations that describe the rate of change (with respect to bubble height above the tuyeres) of the integrated vertical gas and oxide flowrates.

As an approximation, the metal bath (from the end of the tuyere reaction zone to the slag/metal interface) is divided into a number of uniformly spaced imaginary horizontal planes or levels. The differential equations are numerically integrated from one level to the next using a Runge-Kutta or Bulirsch-Stoer method with automatic step length control.

As an approximation it is assumed that the temperature, composition and density of the bulk liquid metal are independent of vertical position in the bath. This excludes the localised oxygen content of the liquid metal associated with the bubble plume (because of the coupling discussed in 4.1.9 above).

4.2.3 Calculation of variables relating to bubbles at a vertical distance h above the tuyeres

The vertical distance x of the bubbles below the slag/metal interface is given by:-

$x = x_{mw} - h$ (4.31)

where x_{mw} is the depth of the tuyeres below the slag/metal

interface and h is the vertical distance between a bubble and the tuyeres.

The total gas flow rate $N'_{GAS}(h)$ through the plane distance h above the tuyeres is:-

$$N'_{GAS}(h) = N'_{CO}(h)+N'_{N2}(h)+N'_{Ar}(h) \qquad (4.32)$$

Note that the oxygen flowrate $N'_{O2}(h)$ is negligible and is assumed to be zero.

The ferrostatic pressure P(h) is given by:-

$$P(h) = (P_{ATM}+(\rho_{X(O)}\times(x_{(O)}-h)+\rho_{H_2O}\times x_{H_2O}))/101325 \qquad (4.33)$$

The diameter $d_{BUB}(h)$ of a bubble is given by:-

$$d_{BUB}(h) = (6\times N'_{GAS}(h)\times R_u\times T_o/(\Pi\times n_{GAS}\times 273,15\times P(h)))^{1/3} \qquad (4.34)$$

The surface area $A_{BUB}(h)$ of a bubble is given by:-

$$A_{BUB}(h) = \Pi\times d_{BUB}(h)^2 \qquad (4.35)$$

The partial pressure $P_i(h)$ of the j'th gas in the bubbles is given by:-

$$P_i(h) = P(h)\times N'_{GAS,i}(h)/N'_{GAS}(h) \qquad (4.36)$$

The rising velocity of bubbles has been discussed in some detail in chapter 3. For small bubbles (diameter less than 1mm) the rising velocity $u_{BUB}(h)$ is given by:-

$$u_{BUB}(h) = G\times(\rho-\rho_{GAS})\times d_{BUB}(h)^2/(18\times\mu) \qquad (4.37.1)$$

For large bubbles (diameter greater than 10mm) the rising velocity is given by:-

$$u_{BUB}(h) = 1,02\times(G\times d_{BUB}(h)/2)^{1/2} \qquad (4.37.2)$$

For intermediate sized bubbles (diameter from 1 to 10mm) the rising velocity is given by:-

$$u_{BUB}(h) = (d_{BUB}(h)-0,001)\times((Y2-Y1)/(0,01-0,001))+Y1 \qquad (4.37.3)$$

where:-

$$Y1 = G\times\rho\times 0,001^2/(18\times\mu) \qquad (4.38.1)$$

and:-

$$Y2 = 1,02\times(G\times 0,01/2)^{1/2} \qquad (4.38.2)$$

The estimation of mass transfer coefficients for the diffusion of carbon, oxygen and nitrogen through the phase boundary layer surrounding a bubble has been discussed in chapter 3.

The mass transfer coefficients $k_{sub,c}(h)$ for carbon and oxygen $k_{sub,o}(h)$ are given by:-

$$k_{sub,c}(h) = 2*(D_c*u_{sub}(h)/(TT*d_{sub}(h)))^{1/2} \quad (4.39.1)$$

$$k_{sub,o}(h) = 2*(D_o*u_{sub}(h)/(TT*d_{sub}(h)))^{1/2} \quad (4.39.1)$$

The mass transfer coefficient $k_{sub,n}(h)$ for nitrogen is given by:-

$$k_{sub,n}(h) = 1/(1/k^*_{sub,n}(h)+1/k^*_n) \quad (4.40)$$

where:-

$$k^*_{sub,n}(h) = 2*(D_n*u_{sub}(h)/(TT*d_{sub}(h)))^{1/2} \quad (4.41.1)$$

and:-

$$k^*_n = -6,27E-4+6,34E-7*(457-562*Ln(\%\underline{O}+0,0763*\%\underline{O}^{1/2})) \quad (4.41.2)$$

The equilibrium nitrogen % concentration $\%\underline{N}_i(h)$ dissolved in the metal phase at the metal/gas interface of the bubbles is given by:-

$$\%\underline{N}_i(h) = K_n*P_{N2}(h)^{1/2}/f_n \quad (4.42)$$

The equilibrium concentrations of carbon and oxygen dissolved in the metal phase at the metal/gas interface are taken into account in the derivation of the decarburization rate equation discussed in appendix A.

4.2.4 Calculation of variables relating to oxide particles at a vertical distance h above the tuyeres

The total molar flowrate of oxides $N'_{ox}(h)$ is given by:-

$$N'_{ox}(h) = \sum_{j=2}^{n} N'_{ox,j}(h) \quad (4.43)$$

The molar fraction $X_{ox,j}(h)$ of the j'th oxide M_xO_y in the oxide particles is given by:-

$$X_{ox,j}(h) = N'_{ox,j}(h)/N'_{ox}(h) \quad (4.44)$$

The volumetric flowrate $Q_{ox}(h)$ of oxide particles is given by:-

$$Q_{ox}(h) = \sum_{j=2}^{n} (N'_{ox,j}(h)*M_{ox,j}/\rho_{ox,j}) \quad (4.45)$$

Note that the assumption is made that the volume change associated with mixing pure oxides is negligible.

The mass flow rate $W_{ox}(h)$ of oxide particles is:-

$$W_{ox}(h) = \sum_{i=2}^{7} (N'_{ox,i}(h) * M_{ox,i}) \qquad (4.46)$$

The molar flowrate $N'_{ox}(h)$ of reducible oxygen in the oxide particles (ie. oxygen combined with Mn, Cr, Mo, Ni and Fe) is given by:-

$$N'_{ox}(h) = \sum_{i=2}^{5} (N'_{ox,i}(h) * z_{v,i}) \qquad (4.47)$$

This variable is used to test whether the rising bubble reaction model can proceed to the next level or whether premature termination is necessary because all the reducible oxides in the oxide particles have been exhausted.

The density $\rho_{ox}(h)$ of the oxide particles is:-

$$\rho_{ox}(h) = W_{ox}(h)/Q_{ox}(h) \qquad (4.48)$$

The radius $r_{ox}(h)$ of an oxide particle is:-

$$r_{ox}(h) = (3*Q_{ox}(h)/(4*\pi*n_{max}))^{1/3} \qquad (4.49)$$

The surface area $A_{ox}(h)$ of an oxide particle is:-

$$A_{ox}(h) = 4*\pi*r_{ox}(h)^2 \qquad (4.50)$$

The oxide particles are assumed to behave as rigid spheres. They rise with a velocity (relative to the bulk liquid metal in the plume of rising bubbles) that can be calculated with Stoke's law. The mass transfer coefficients (for oxygen and silicon diffusing through the metal phase boundary layer surrounding an oxide particle) is derived by combining Stoke's Law and the Higbie model.

Thus the mass transfer coefficient $k_{ox,o}(h)$ for oxygen is:-

$$k_{ox,o}(h) = (1,387*D_o*r_{ox}(h)*(\rho-\rho_{ox}(h))/\mu)^{1/2} \qquad (4.51)$$

and for silicon the mass transfer coefficient $k_{ox,si}(h)$ is:-

$$k_{ox,si}(h) = (1,387*D_{si}*r_{ox}(h)*(\rho-\rho_{ox}(h))/\mu)^{1/2} \qquad (4.52)$$

4.2.5 Calculation of Gibb's free energy of reduction of metal oxides by carbon and silicon

4.2.5.1 Carbon reduction of metal oxides

For the carbon reduction of oxide M_xO_y (for elements displaying Raoultian behaviour) according to the reaction:-

$$1/y\ M_xO_y + [\%C] \rightarrow x/y\ [M] + CO \qquad (4.53.1)$$

the Gibb's free energy $\Delta G_{f,c}(h)$ is given by:-

$$\Delta G_{f,c}(h) \approx (-A_f - B_f * T_a)/z_{y,f} - 133391 - 45,971 * T_a + R * T_a * Ln((X_{MET,f} * * z_{y,f}/X_{ox,f}(h)) * * (1/z_{y,f}) * \phi_c(h)) \qquad (4.54.1)$$

where:-

$$\phi_c(h) = P_{co}(h)/(\%C f_c) \qquad (4.55)$$

In the case of the carbon reduction of oxides of elements displaying Henrian behaviour:-

$$1/y\ M_xO_y + [\%C] \rightarrow x/y\ [\%M] + CO \qquad (4.53.2)$$

the Gibb's free energy is given by:-

$$\Delta G_{f,c}(h) \approx (-A_f - B_f * T_a)/z_{y,f} - 133391 - 45,971 * T_a + (\underline{A}_f + \underline{B}_f * T_a) * (z_{y,f}/z_{y,f}) + R * T_a * Ln(\Psi_c(h)) \qquad (4.54.2)$$

where:-

$$\Psi_c(h) = ((\%M_x f_f) * * z_{M,f}/X_{ox,f}(h)) * * (1/z_{y,f}) * \phi_c(h) \qquad (4.56)$$

and $\phi_c(h)$ is given by (4.55) above.

4.2.5.2 Silicon reduction of metal oxides

For the silicon reduction of oxide M_xO_y of elements displaying Raoultian behaviour:-

$$[\%Si] + 2/y\ M_xO_y \rightarrow 2x/y\ [M] + SiO_2 \qquad (4.57.1)$$

the Gibb's free energy $\Delta G_{f,si}(h)$ is given by:-

$$\Delta G_{f,si}(h) = A_{SiO2} - 2 * A_f/z_{y,f} - \underline{A}_{Si} + L * * (B_{SiO2} - 2 * B_f/z_{y,f} - \underline{B}_{Si}) + R * T_a * Ln(\phi_{Si}(h)) \qquad (4.58.1)$$

where $\phi_{Si}(h)$ is:-

$$\phi_{Si}(h) = (X_{MET,f} * * z_{M,f}/X_{ox,f}(h)) * * (2/z_{y,f}) * X_{ox,SiO2}(h)/(\%Si * f_{Si}) \qquad (4.59.1)$$

For the silicon reduction of oxides of elements displaying Henrian behaviour:-

$$[\%Si] + 2/y M_xO_y \rightarrow 2x/y[\%M] + SiO_2 \qquad (4.57.2)$$

the Gibb's free energy is:-

$$\Delta G_{i,Si}(h) = A_{Si,SiO_2} + 2/z_{y,i} * (-A_i + z_{x,i} * \underline{A}_i) - \underline{A}_{Si} + T_k * (B_{Si,SiO_2} + 2/z_{y,i} * (-B_i + z_{x,i} * \underline{B}_i) - \underline{B}_{Si}) + RT_k * Ln(\Psi_{Si}(h)) \qquad (4.58.2)$$

where $\Psi_{Si}(h)$ is:-

$$\Psi_{Si}(h) = ((\%\underline{M}_i)^{z_{x,i}}/X_{Ox,i}(h))^{(2/z_{y,i})} * X_{Ox,SiO_2}(h)/(\%\underline{Si})^{z_{Si}} \qquad (4.59.2)$$

4.2.5.3 Combined reduction of metal oxides

A simplifying assumption is made in the model[1,2] that only those reactions with negative free energies may proceed (ie. the reduction of metal oxides in oxide particles is considered, for the purposes of the model, to be irreversible).

Thus, if:-

$$\Delta G_{i,C}(h) > 0 \qquad (4.60.1)$$

then:-

$$\Delta G_{i,C}(h) = 0 \qquad (4.60.2)$$

Similarly, if:-

$$\Delta G_{i,Si}(h) > 0 \qquad (4.61.1)$$

then:-

$$\Delta G_{i,Si}(h) = 0 \qquad (4.61.2)$$

Thus, the sum of the free energies for reduction by carbon is:-

$$\Delta G_C(h) = \sum_{i=3}^{n} \Delta G_{i,C}(h) \qquad (4.62)$$

and for silicon it is:-

$$\Delta G_{Si}(h) = \sum_{i=3}^{n} \Delta G_{i,Si}(h) \qquad (4.63)$$

4.2.6 Calculation of oxygen concentration in metal phase at metal/oxide interface

As a simplifying approximation, it is assumed that the oxygen concentration $C_{O,I}(h)$ in the metal phase at the metal/oxide interface is determined by the reaction:-

$$M_xO_y \Leftrightarrow x[M] + y[O] \qquad (4.2)$$

that gives the highest oxygen concentration. This is determined by calculating the oxygen concentration in the metal for each reaction and selecting the highest. Strictly speaking this means that all other reduction reactions are going in reverse, but as a simplifying assumption this has been abitrarily prevented in the previous section.

It is also assumed that the concentration of each element M at the interface is approximately equal to its concentration in the bulk liquid metal. The activity of each oxide is assumed to be equal to its molar fraction $X_{Ox,j}(h)$.

Thus $C_{Ox,I}(h)$ is given by:-

$$C_{Ox,I}(h) = Max(C^{\circ}_{Ox,j}(h)) \qquad (4.64)$$

where, for elements displaying Raoultian behaviour:-

$$C^{\circ}_{Ox,j}(h) = K_{Ox,j} * (\rho/(f_O * 1600)) * (X_{Ox,j}(h)/(X_{Met,j} * z_{x,j})) * (1/z_{y,j}) \qquad (4.65.1)$$

For elements displaying Henrian behaviour:-

$$C^{\circ}_{Ox,j}(h) = K_{Ox,j} * (\rho/(f_O * 1600)) * (X_{Ox,j}(h)/(\%\underline{M}_j * z_{x,j})) * (1/z_{y,j}) \qquad (4.65.2)$$

4.2.7 Calculation of silicon concentration in the metal phase at the metal/oxide interface

The concentration of silicon in the metal at the metal/oxide interface of an oxide particle at a distance h above the tuyeres is determined by the reaction:-

$$[Si] + 2[O] \Leftrightarrow SiO_2 \qquad (4.66)$$

The oxygen concentration $C_{Ox,I}(h)$ is as calculated in the preceeding section. The SiO_2 activity in the oxide is assumed to be equal to its molar fraction $X_{Si,Ox}(h)$. From the equilibrium constant of the reaction represented by 4.66 it can be shown that the molar concentration of silicon at the interface is given by:-

$$C_{Si,I}(h) = X_{Si,Ox}(h) * p^2 / [Exp((594128 - 212,67 * T_s)/(8,3 * T_s)) * 7,19104E9 * (C_{Ox,I}(h) * f_O)^2] \qquad (4.67)$$

4.2.8 Calculation of the decarburization and desiliconization rates at a distance h above the tuyeres

For coupled oxygen fluxes in the oxide and bubble boundary layers, the decarburization rate $\dot{r}_C(h)$ at a vertical distance h above the tuyeres is given by:-

$$\dot{r}_C(h) = (-B-(B^{**}2-4*A*C)^{**}(1/2))/(2*A) \qquad (4.68)$$

where:-

$$A = (1/(u_{BUB}*A_{BUB}(h)))^{**}2)+k_{BUB,O}(h)/(u_{BUB}^{**}2*A_{BUB}(h)*A_{OX}(h)*k_{MT,O}(h)) \quad (4.69.1)$$

and:-

$$B = -((K_{BUB,C}(h)*C_{MT,C}+K_{BUB,O}(h)*C_{CO,O}(h)) / (u_{BUB}*A_{BUB}(h))+k_{BUB,C}(h)*K_{BUB,O}(h)*C_{MT,C}/(u_{BUB}*A_{BX}(h)*k_{MT,O}(h)) \quad (4.69.2)$$

and:-

$$C = K_{BUB,C}(h)*k_{BUB,C}(h)*(C_{MT,C}*C_{CO,O}(h)-P_{CO}(h)*K_{CO}) \qquad (4.69.3)$$

The derivations of equations 4.68 and 4.69 are presented in appendix A.

The desiliconisation rate at a height h above the tuyeres is given by:-

$$\dot{r}_{Si}(h) = u_{BUB}*A_{BX}(h)*k_{MT,Si}(h)*(W_{MT,Si}/V_M-C_{CO,Si}(h)) \qquad (4.70)$$

4.2.9 Formulation of the differential equations describing the rate of change of the integrated vertical gas and oxide flowrates

The rate of change of the integrated vertical flowrate of CO flowrate at a distance h above the tuyeres is given by:-

$$d(N'_{CO}(h))/dh = \dot{r}_C(h)/u_{BUB}(h) \qquad (4.71)$$

Therefore, the CO flowrate at a height h+Δh above the tuyeres is given by:-

$$N'_{CO}(h+\Delta h) = N'_{CO}(h)+\int_h^{h+\Delta h} (\dot{r}_C(h)/u_{BUB}(h))dh \qquad (4.72)$$

The rate of change of the SiO_2 flowrate is given by:-

$$d(N_{SiO2}(h))/dh = \dot{r}_{Si}(h)/u_{BUB}(h) \qquad (4.73)$$

Similarly, the SiO_2 flowrate at a position $h+\Delta h$ above the tuyeres is given by:-

$$N_{SiO2}(h+\Delta h) = N_{SiO2}(h)+\int_{h}^{h+\Delta h}(Z_{Si}(h)/u_{SOG}(h))dh \qquad (4.74)$$

The rate of change of the j'th oxide M_xO_y flowrate is given by:-

$$d(N'_{Ox,j}(h))/dh = (Y_{O,j}(h)+Y_{Si,j}(h))/u_{SOG}(h) \qquad (4.75)$$

where $j = 3, 4, \ldots$ and:-

$$Y_{O,j}(h) = -\tfrac{1}{2}*(h)*\Delta G_{j,c}(h)/(\Delta G_c(h)*z_{v,j}) \qquad (4.76)$$

and:-

$$Y_{Si,j}(h) = -\tfrac{1}{2}*(h)*2*\Delta G_{j,m}(h)/(\Delta G_{Si}(h)*z_{v,j}) \qquad (4.77)$$

Therefore the flowrate of the j'th oxide M_xO_y at a height $h+\Delta h$ above the tuyeres is given by:-

$$N'_{Ox,j}(h+\Delta h) = N'_{Ox,j}(h)+\int_{h}^{h+\Delta h}((Y_{O,j}(h)+Y_{Si,j}(h))/u_{SOG}(h))dh \qquad (4.78)$$

The rate of change of the nitrogen flowrate is given by:-

$$d(N'_{N2}(h))/dh = J_{N2}(h)/u_{SOG}(h) \qquad (4.79)$$

where $J_{N2}(h)$ is given by:-

$$J_{N2}(h) = -k_{SOG,N}(h)*n_{SOG}*A_{SOG}(h)*p*(\%\overline{N}_2(h)-\%\overline{N})/(M_N*200) \qquad (4.80)$$

Therefore, the nitrogen flowrate at a distance $h+\Delta h$ above the tuyeres is given by:-

$$N'_{N2}(h+\Delta h) = N'_{N2}(h)+\int_{h}^{h+\Delta h}(J_{N2}(h)/u_{SOG}(h))dh \qquad (4.81)$$

The bubble depth below the slag/metal interface at a vertical height $h+\Delta h$ above the tuyeres is simply:-

$$x = x_{rcv}-(h+\Delta h) \qquad (4.82)$$

4.3 Numerical integration between the level h and h+Δh above the tuyeres

The relevant equations presented in section 4.2.8 above (ie. equations 4.72, 4.74, 4.78 and 4.81) are simultaneously integrated through successive vertical distances dh using a Runge-Kutta or Bulirsch-Stoer method* incorporating automatic step length control. The procedure terminates when x=0 (as given by equation 4.82 above).

4.4 Results

The results of typical simulations are presented in figures 4.3 to 4.6.

In figure 4.3 and 4.4 the flowrates of gases and oxides in the Rising Bubble Reaction Zone are presented as functions of vertical distance above the tuyeres. The bath chemistry and temperature are typical of those at the commencement of the initial 3:1 blow of a 304 type austenitic steel. In this simulation Ni and Fe were allowed to be participating elements in addition to C, Si, Mn, and Cr. The initial bubble diameter at the tuyeres (at the start of the tuyere reaction zone) was an arbitrary 15mm.

It can be seen from figure 4.3 that decarburization is extremely rapid during the first 100mm that a bubble rises. Thereafter decarburization is almost negligible. From figure 4.4 it is evident that this very high decarburization rate corresponds with very high reduction rates of particularly the NiO and FeO and, to a lesser extent, the Cr_2O_3 initially in the bubbles leaving the tuyere reaction zone. This can be attributed to the high oxygen potentials associated with particularly the former two oxides.

In general very high decarburization efficiencies (93-94%) are predicted by the model when Ni and Fe (and Mo) are allowed to participate. Significantly lower decarburization efficiencies are evident when only Si, Mn and Cr_2O_3 are allowed to participate. The model might well be improved if it were to be re-formulated to allow reduction of NiO, MoO_3 and FeO by Cr and Mn in addition to C and Si.

Desiliconization can be seen to continue well beyond the position in the bath where decarburization has ceased. This is accompanied by further reduction of MnO and Cr_2O_3.

From figure 4.5 it can be seen that nitrogen goes into solution from approximately 100mm to 400mm above the tuyeres. This is because, in this region, the partial pressure of nitrogen in the bubbles is higher than that representing equilibrium with nitrogen dissolved in the bath. Thereafter, as the ferrostatic pressure reduces with increased height above the tuyeres, nitrogen starts to come out of solution. This is evident from the increase in nitrogen flowrate from 400mm to 1100mm above the tuyeres.

The initial increase in the nitrogen flowrate from 0mm to 100mm above the tuyeres is difficult to explain and may represent a degree of instability in the integrator associated with the choice of initial step length and precision in a region characterized by very rapidly changing gas composition in the bubbles (ie. very high initial decarburization rate). A more typical nitrogen flowrate vs. height trajectory is illustrated in figure 4.5.

In figures 4.5 and 4.6 the flowrates of gases and oxides in the Rising Bubble Reaction Zone are again presented as functions of vertical distance above the tuyeres. The bath chemistry and temperature are typical of those at the commencement of a 1:1 (ie. $30m^3O_2min^{-1}:30m^3N_2min^{-1}$) blow of a 304 type austenitic steel.

In this simulation, Ni and Fe were allowed to be participating elements, in addition to C, Si, Mn, and Cr. The initial bubble diameter at the tuyeres (at the start of the tuyere reaction zone) was an arbitrary 15mm.

Similar trends are evident as in figures 4.3 and 4.4. There is initially a very rapid increase in the CO flowrate associated with the reduction of FeO, NiO and Cr_2O_3.

Nitrogen rapidly goes into solution in the first 300mm above the tuyeres. This is because the partial pressure of nitrogen in the bubbles is greater than that in equilibrium with the nitrogen concentration in the bulk liquid metal. Thereafter it starts to come out of solution again to some extent as the ferrostatic pressure reduces with increased bubble height above the tuyeres.

In the case of the oxides, rapid initial reduction of NiO, FeO and Cr_2O_3 by carbon is evident. Reduction of oxides by Si is also in evidence with the increase in the SiO_2 flowrate.

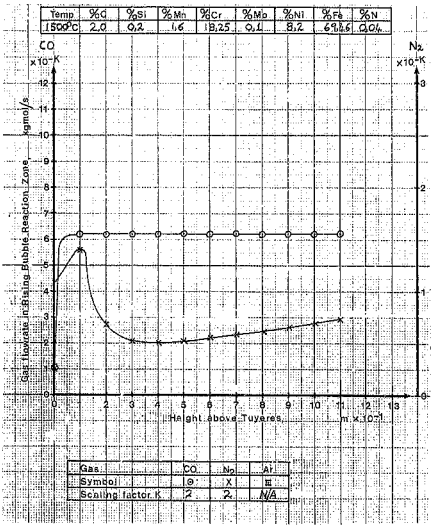


Figure 4.3: Typical Rising Bubble Reaction Model data output in respect of gas flowrates resulting from a 3:1 O_2:N_2 blowing ratio and an initial 10mm diameter bubble at the tuyeres.

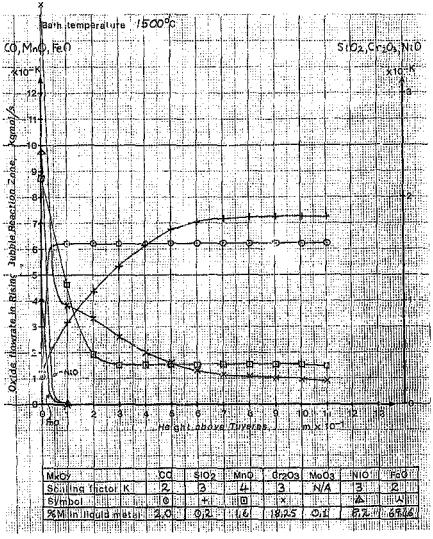


Figure 4.4: Typical Rising Bubble Reaction Model data output in respect of oxide flowrates resulting from a 5:1 O_2:N_2 blowing ratio and an initial 15mm diameter bubble at the tuyeres.

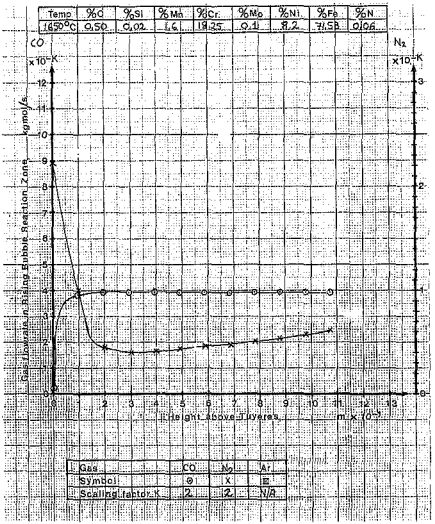


Figure 4.5: Typical Rising Bubble Reaction Model data output in respect of gas flowrates resulting from a 1:1 O_2:N_2 blowing ratio and an initial 15mm diameter bubble at the tuyeres.

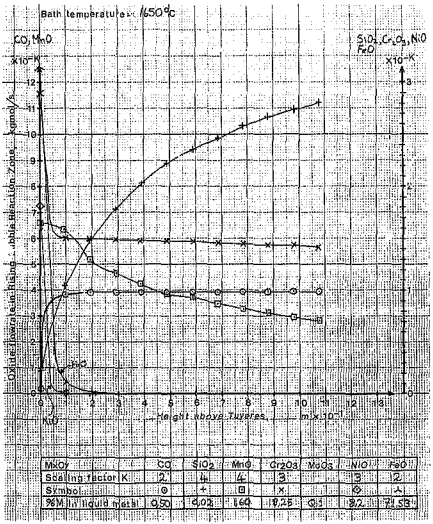


Figure 4.6 Typical Rising Bubble Reaction Model data output in respect of oxide flowrates resulting from a 1:1 O_2:N_2 blowing ratio and an initial 15mm diameter bubble at the tuyeres.

5 MODEL FOR THE ESTIMATION OF THE BATH DEPTH AT THE TUYERE LEVEL

5.1 Introduction

A cross sectional view of the AOD vessel shell and its lining is presented in figure 5.1.

The lining thickness varies according to both position (some areas are, by design, significantly thicker than others) and its age (measured in terms of heats processed). Thus the metal depth at the tuyere level (and hence ferrostatic pressure) has to be calculated numerically on a heat for heat basis. This is also so because variable metal and slag volumes have to be taken into account. These change from heat to heat and from the start to the end of a heat.

In the model it is assumed that:-

(i) the lining thickness decreases linearly according to the number of heats processed (ie. lining's age);

(ii) the lining wear pattern is the same on either side of a vertical plane cutting the vessel in half between the #2 and #3 tuyeres (refer figure 6.3 in chapter 6).

Referring to Fig 5.1 it is evident that the vessel consists of four distinct zones:-

(i) the base consisting of the segment of a sphere;

(ii) a lower conical section;

(iii) a cylindrical *middle section*;

(iv) an upper conical section referred to as the dome.

From operating experience it is known that most of the lining wear takes place in items (i), (ii) and (iii) above. Lining wear in the dome is negligible in comparison and can be ignored. This is because the level of the bath never extends into the dome except when the vessel is tilted into the horizontal position.

The new and old working lining thickness of the base is given by BT_1 and BT_2 respectively, where:-

BT_1 = 350mm and BT_2 = 200 mm.

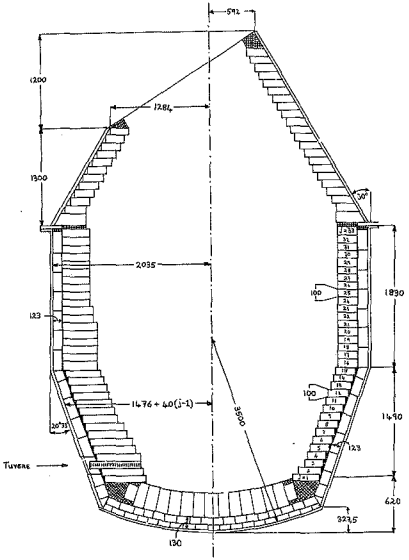


Figure 5.1: Vertical cross section through vessel shell and lining

Lining thickness data for items (ii) and (iii) is presented in Tables 5.1.1 (new lining) and 5.1.2 (worn out lining). For computational purposes in the model, this data is stored in a three dimensional matrix $LT_{i,j,k}$ where i, j and k are interpreted as follows:-

i = 1 or 2 where 1 denotes the new working lining thickness; and 2 " " old " " "

j = 1,2,...,33 where j is the brick layer number;

k = 1,2,...,7 where k is the radial position, in 30° increments from 0° to 180°, relative to the midpoint between #2 and #3 tuyeres.

The new working lining thickness data is the actual thickness of the brickwork of a newly installed lining. This excludes the backup lining whose thickness remains constant and which is taken into account separately.

The old lining data is an average of the actual thickness measurements, taken[12] during lining breakout and rebuilding operations, for a large number of linings installed to date. The backup lining thickness is excluded.

The lining thickness data for the lower conical and cylindrical sections is summarized in Tables 5.1.1 and 5.1.2 on the following pages.

The lining thickness of the upper conical section or dome is assumed to remain more or less constant throughout the lifetime of a lining. Although this is taken into account in the model for heat flow through the lining (see chapter 7), the dome is not considered in the tuyere depth model. This is because the vessel is never filled to the extent that the surface of the slag layer is above the top of the cylindrical section when the vessel is in the vertical blowing position.

Layer #	Radial Position in Degrees						
	0	30	60	90	120	150	180
	Working Lining Thickness in Millimetres						
1	550	550	550	550	350	350	350
2	550	550	550	550	350	350	350
3	550	550	550	550	350	350	350
4	550	550	550	550	350	350	350
5	550	550	550	550	350	350	350
6	550	550	550	550	350	350	350
7	500	500	500	500	350	350	350
8	500	500	500	500	350	350	350
9	450	450	450	450	350	350	350
10	450	450	450	450	350	350	350
11	450	450	450	450	350	350	350
12	450	450	450	450	350	350	350
13	450	450	450	450	350	350	350
14	450	450	450	450	350	350	350
15	450	450	450	450	350	350	350
16	450	450	450	450	350	350	350
17	450	450	450	450	350	350	350
18	450	450	450	450	350	350	350
19	450	450	450	450	350	350	350
20	450	450	450	450	350	350	350
21	450	450	450	450	350	350	350
22	400	400	400	400	300	300	300
23	400	400	400	400	300	300	300
24	350	350	350	350	250	250	250
25	350	350	350	350	250	250	250
26	350	350	350	350	250	250	250
27	350	350	350	350	250	250	250
28	350	350	350	350	250	250	250
29	350	350	350	350	250	250	250
30	350	350	350	350	250	250	250
31	350	350	350	350	250	250	250
32	350	350	350	350	250	250	250
33	350	350	350	350	250	250	250

TABLE 5.1.1: New working lining thickness of the lower conical and cylindrical sections of the vessel

Layer #	Radial Position in Degrees						
	0	30	60	90	120	150	180
	Working Lining Thickness in Millimetres						
1	240	243	234	215	130	140	150
2	240	243	234	215	130	140	150
3	200	197	193	190	120	120	100
4	200	199	189	170	120	120	100
5	150	134	132	105	95	100	90
6	150	137	126	125	95	100	90
7	140	92	76	90	85	80	80
8	140	93	73	80	85	80	80
9	100	83	54	75	65	65	40
10	100	64	52	65	65	65	40
11	90	54	41	50	55	55	40
12	70	32	25	50	55	30	30
13	70	33	24	45	55	30	30
14	70	42	33	45	50	35	30
15	90	63	51	55	65	95	130
16	90	61	56	75	65	95	130
17	90	90	90	90	85	105	130
18	140	113	100	100	105	125	150
19	140	117	105	105	105	125	150
20	150	124	109	105	115	130	160
21	150	132	119	110	115	115	100
22	150	138	121	100	95	90	100
23	150	134	114	90	80	75	90
24	150	139	118	85	65	65	90
25	160	154	132	95	60	65	100
26	160	169	154	115	50	65	120
27	160	182	170	125	50	65	130
28	170	192	180	135	60	75	140
29	180	193	193	180	70	85	150
30	170	152	186	180	80	95	160
31	160	94	186	195	75	95	160
32	150	121	141	210	125	115	160
33	160	131	151	220	135	125	160

TABLE 5.1.2: Final working lining thickness of the lower conical and cylindrical sections of the vessel.

5.2 Calculation of Tuyere Depth and Associated Ferrostatic Pressure

5.2.1 Calculation of metal and slag phase densities and volumes

In order to calculate the tuyere depth and associated ferrostatic pressure, the volumes of liquid slag and metal corresponding to the known masses of these phases are required. Density data for the slag and metal compositions typically present in the AOD process does not appear to be available in the literature for the temperature range 1450-1750°C. However, density data is available[3] for the i'th pure metal and the j'th pure oxide as a linear function of temperature T:-

$$\rho_i(T) = A_i + B_i*T \qquad (5.1.1)$$

$$\rho_{ox,j}(T) = A_{ox,j} + B_{ox,j}*T \qquad (5.1.2)$$

where A_i, $A_{ox,j}$, B_i and $B_{ox,j}$ are constants.

The model in its present form uses the individual densities ρ_i and $\rho_{ox,j}$ for each component at 1650°C to calculate metal and slag volumes:-

$$V_m = \sum_{i=1}^{n} (m_{met,i}/\rho_i) \qquad (5.2.1)$$

$$V_{sl} = \sum_{j=1}^{k} (m_{sl,j}/\rho_{sl,j}) \qquad (5.2.2)$$

It is assumed, as an approximation, that there is no change in volume with mixing.

The temperature dependence of density could be built into the model at a later stage without any difficulty if this was considered to be necessary.

5.2.2 Calculation of metal volume below tuyere level

The metal volume V_B below the tuyere level is given by:-

$$V_B = V_{SP}+2*(\sum_{i=1}^{3} dV_i)+dV_3 \qquad (5.3)$$

Note that the tuyeres are located in the middle of brick layer #3.

V_{SP} is the volume of the segment of a sphere forming the bottom of the vessel and is given by:-

$$V_{SP} = (\Pi/3)*h_{SP}^2*(3*r_{SP}-h_{SP}) \qquad (5.4)$$

r_{sp} and h_{sp} are the radius and height of the segment of a sphere and are given by:-

$$r_{sp} = 3,5-(0,13*X) \qquad (5.5)$$

$$h_{sp} = 0,62-(0,13*X) \qquad (5.6)$$

where X is the brick thickness of the vessel floor and is given by:-

$$X = BT_1-(BT_1-BT_2)*VL_1/VL_2 \qquad (5.7)$$

BT_1 and BT_2 are the thicknesses of the vessel working lining floor bricks for a new and worn-out lining respectively.

VL_1 and VL_2 are the vessel lining age (heats completed to date) and estimated lining lifespan (heats completed by the time the lining is replaced) respectively.

dV_j is the volume of the "half disk" of metal of thickness DH=0,1m (ie. the vertical height of each layer of bricks) enclosed by the j'th layer of bricks. dV_j is estimated using Simpson's Rule to integrate, at 30° intervals, from 0° to 180° and is given by:-

$$dV_j = 0,5*TT*(30/180)*DH*(1/3)*(r_{j,0}^2+2*(r_{j,60}^2+r_{j,120}^2) +4*(r_{j,30}^2+r_{j,90}^2+r_{j,150}^2)+r_{j,180}^2)$$

$$= DH*TT/36*(r_{j,0}^2+2*(r_{j,60}^2+r_{j,120}^2)+4*(r_{j,30}^2+r_{j,90}^2+r_{j,150}^2)+r_{j,180}^2) \qquad (5.8)$$

where $r_{j,k}$ is the inner radius of the lining at brick layer j and radial position k degrees from the midpoint between #2 and #3 tuyeres. It is given by:-

$$r_{j,k} = 1,476+0,04*(j-1)-(LT_{1,j,k}-VL_1*(LT_{1,j,k}-LT_{2,j,k})/VL_2)*0,126) \qquad (5.9)$$

Note that equation 5.9 holds only for the lower conical section where $0<j<16$.

5.2.3 Calculation of the vertical distance between the tuyeres and the slag/metal interface

The metal volume V_m above the tuyeres is given by:

$$V_m = V_n-V_s \qquad (5.10)$$

assuming that the vessel is in a vertical position and no gas is being blown.

The vertical distance between the tuyeres and the slag/metal interface is iteratively calculated by establishing at which brick layer number n the following condition first applies:-

$$V_A \leq (dV_s+2*\sum_{j=4}^{n} dV_j) \qquad (5.11)$$

For $4 \leq j \leq 15$ equation 5.1.10 applies.

For $j>15$:-

$$r_{j,k} = 2,035-((LT_{1,1,k}-(LT_{1,1,k}-LT_{2,j,k})*VL_j/VL_2)+0,138) \qquad (5.12)$$

Equation 5.8 still applies for determining dV_j.

If:-

$$V_A < (dV_s+2*\sum_{j=4}^{n} dV_j) \qquad (5.13.2)$$

then the slag/metal interface is at some intermediate position up the side of the n'th brick layer.

The distance x_{TUY} between the slag/metal interface and the tuyeres is given by one of the following:-

if:-

$$V_A = (dV_s+2*\sum_{j=4}^{n} dV_j) \qquad (5.13.1)$$

then:-

$$x_{TUY} = 0,05+(n-4)*0,10 \qquad (5.14.1)$$

or if:-

$$V_A < (dV_s+2*\sum_{j=4}^{n} dV_j) \qquad (5.13.2)$$

then:-

$$x_{TUY} = 0,05+(n-4)*0,10+dh \qquad (5.14.2)$$

where:-

$$dh = 0,1*(1-(dV_s+2*\sum_{j=4}^{n} dV_j-V_A)/(2*dV_n)) \qquad (5.15)$$

5.2.4 Calculation of the thickness of the slag layer

The thickness of the slag layer x_{SLG} is calculated as follows. If the slag volume:-

$$V_{SLG} \leq 2*dV_n*(0,1-dh)/0,1 \qquad (5.16.1)$$

then:-

$$x_{SLG} = 0,1*V_{SLG}/(2*dV_n) \qquad (5.17.1)$$

where $2*dV_n$ is the volume element bounded by the n'th brick layer that contains the slag/metal interface.

However, if:-

$$V_{SLG} > 2*dV_n*(0,1-dh)/0,1 \qquad (5.16.2)$$

then

$$x_{SLG} = (0,1-dh)*2*dV_n/0,1+0,1*(p-n-1)+dh_{SLG} \qquad (5.17.2)$$

where p is the brick layer number of the volume element containing the top surface of the slag layer. "p" is calculated iteratively by establishing at which brick layer number the following condition first applies:-

$$V_{SLG} \leq (0,1-dh)*dV_n/0,1+2*\sum_{j=n+1}^{p} dV_j \qquad (5.18)$$

For $4 \leq j \leq 15$ equation 5.9 applies.

For $j > 15$ equation 5.12 applies.

Equation 5.8 applies for the calculation of dV_j.

If $V_{SLG} = 2*dV_n*(0,1-dh)/0,1+2*\sum_{j=n+1}^{p} dV_j \qquad (5.19)$

then $dh_{SLG} = 0 \qquad (5.20)$

If $V_{SLG} < 2*dV_n*(0,1-dh)/0,1 \qquad (5.21)$

then:-

$$dh_{SLG} = 0,1*(1-(2*dV_n*(0,1-dh)/0,1+2*\sum_{j=n+1}^{p} dV_j-V_{SLG})/(2*dV_n)) \qquad (5.22)$$

5.2.5 Calculation of the ferrostatic pressure at the tuyere level

Having calculated the distance $x_{f,w}$ between the slag/metal interface and the tuyeres and the thickness $x_{sl,s}$ of the slag layer, the ferrostatic pressure P_{twy} (in atmospheres) at tuyere level can be calculated:-

$$P_{twy} = (P_{atm}+G*(\rho_{f,s}*x_{twy}+\rho_{sl,s}*x_{sl,s}))/101325 \qquad (5.23)$$

where:-

P_{atm} = atmospheric pressure (N/m²)

G = acceleration due to gravity (m/s²)

The density ρ of the metal phase is given by:-

$$\rho = (\sum_{j=1}^{n} m_{HST,j})/(\sum_{j=1}^{n} (m_{HST,j}/\rho_j)) \qquad (5.24)$$

and the density of the slag phase $\rho_{sl,s}$ is given by:-

$$\rho_{sl,s} = (\sum_{i=2}^{k} m_{sl,s,i})/(\sum_{i=2}^{k} (m_{sl,s,i}/\rho_{sl,s,i})) \qquad (5.25)$$

6 MODEL FOR DETERMINING THE EQUIVALENT LINING THICKNESS AND HOT FACE SURFACE AREA OF THE REFRACTORY LINING

6.1 *Introduction*

For heat balance calculations the vessel lining thickness is an important variable, as is the surface area of the lining in direct or radiant heat contact with the slag and metal.

However, lining thickness is a function of both position in the vessel and the number of heats that have been made to date. Strictly speaking, lining thickness at any particular position decreases at various rates (depending on factors such as the stage in the process, recent thermal history of the lining, slag chemistry, localized temperature, velocity gradients of the bath, to name but a few) throughout the heat.

Quantification of the rate of lining thickness decrease is a complex problem and, for simplicity, the following assumptions are made in the model in its present form:-

(i) the lining thickness remains constant for the duration of a heat;

(ii) the lining thickness decreases stepwise in constant decrements from heat to heat during the course of its life.

These assumptions are graphically illustrated in Fig. 6.1. The model could be refined to make lining thickness a continuous function of "cumulative metal contact time". However,it is felt that the uncertain benefits to be gained would be heavily outweighed by a greatly increased price in terms of computational time.

The model structure is of such a nature that it is theoretically possible to individually calculate heat flow through a large number of discrete volume elements of the lining (to take into account variation in thickness with position in the vessel) covering the entire lining surface. However, this option has not been adopted because of the increased complexity and computational time. It is also considered unlikely that any great benefit would be obtained (in terms of accuracy).

As an approximation, heat flow through the lining is modelled as if the lining was a parallel sided plate of equivalent thickness Y_{lin} and hot face surface area A_{lin}. This is based on a simplifying assumption that the inside and outside surface temperatures of the vessel lining and shell are uniform over the respective surfaces.

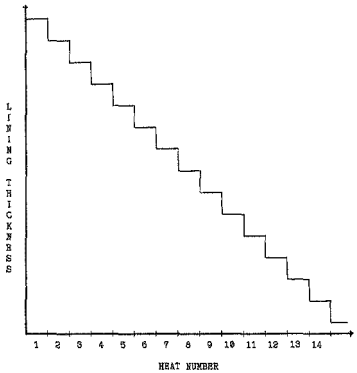


Figure 6.1: Simplifying model of the dependence of lining thickness on heat number

This assumption is obviously not strictly true, particularly for the outside surface of the vessel where relatively high localized temperatures (compared to other areas) can be expected. For example, where:-

(i) the lining is comparatively thin;

(ii) the heat transfer rate from the vessel shell to the surroundings is comparatively low for one or other reason (eg. a build-up of slag encrustations).

It also does not take into account that convective heat transfer takes place from the liquid metal and slag to the "wetted" areas of the lining. In the vessel dome however, heat transfer by

radiation and gas convection could be expected to be the dominating mechanisms. Thus it could be expected that the refractory surface temperature in direct contact with the liquid phases may be marginally higher than that in contact with the gas phase.

Nevertheless, any inaccuracies due to these simplifications can be dealt with using suitable empirically determined correction factors if subsequently found to be necessary. This also applies to the inherent simplifications associated with the equivalent lining thickness concept to be developed in the following section.

In calculating the "equivalent lining thickness" X_{LM}, the well known analogy is made of thermal resistance with the equivalent resistance of a number of resistors connected in parallel. This is illustrated in Figure 6.2 below, together with the following explanation which is included for sake of completeness.

Each resistor is equivalent to a discrete volume element of the vessel lining. Each resistor's resistance is analogous to the resistance to heat flow through the refractory brickwork associated with the corresponding volume element. The resistance to heat flow is approximately proportional to the thickness of the refractory and inversely proportional to the cross sectional area perpendicular to the direction of heat flow. The voltage drop across the resistor network is equivalent to the temperature difference between the inner "hot face" (in contact with the liquid metal) and outer surface of the refractory lining (in contact with the vessel shell).

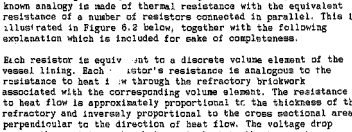


Figure 6.2: Resistance analogue of heat flow through refractory lining

6.2 Mathematical Description of the Model

6.2.1 Equivalent lining thickness

Considering the preceding discussion, the overall heat transfer rate Q through the lining is analogous to the total current I through the resistor network.

Therefore:-

$I \propto 1/R_{TOT} \quad (6.1)$

is analogous to:-

$Q \propto A_{LIN}/Y_{LIN} \quad (6.2)$

where:-

A_{LIN} = Total surface area of the lining hot face.

Y_{LIN} = Equivalent lining thickness.

R_{TOT} = Equivalent resistance of the parallel resistor network.

NOW:-

$$1/R_{TOT} = \sum_{i=1}^{n} (1/R_i) \quad (6.3)$$

Similarly:-

$$(\int dA)/Y_{LIN} = \int (1/LT)\,dA \quad (6.4)$$

$$\Rightarrow Y_{LIN} = \int dA / \int (1/LT)\,dA \quad (6.5)$$

where:-

LT = Lining thickness at a particular position.

dA = Hot face surface area of lining at a particular position.

Equation 6.5 is expanded to incorporate the four main sections of the vessel (see chapter 5), namely:-

(i) the bottom (bot);

(ii) the lower conical section (con);

(iii) the middle cylindrical section (cyl);

(iv) the upper conical section or dome (dom).

Thus:-

$$V_{LIN} = (\int dA)_{BOT} + (\int dA)_{CON} + (\int dA)_{CYL} + (\int dA)_{DOM}$$
$$/(\int (1/LT)dA)_{BOT} + (\int (1/LT)dA)_{CON} + (\int (1/LT)dA)_{CYL} + (\int (1/LT)dA)_{DOM} \quad (6.6)$$

6.2.2 Bottom section of vessel

For the bottom section:-

$$(dA)_{BOT} = 2*TT*(3,5-BLT-Y)\times(0,14+BT_1-Y) \quad (6.7)$$
(= area of segment of a sphere)

where:-

$$Y = BT_1-(BT_1-BT_2)*VL_1/VL_2 \quad (6.8)$$
(= thickness of bottom lining excluding backup lining)

and BT_1 and BT_2 are the thicknesses of the bottom lining (excluding backup lining) at the beginning and end of the lining's life.

BLT = 0,13m = backup lining thickness.

$$(\int (1/LT)dA)_{BOT} = (\int dA)_{BOT}/(Y+BLT) \quad (6.9)$$

6.2.3 Lower conical and cylindrical sections of vessel

For the lower conical and cylindrical sections a numerical (Simpson's Rule) integration technique is used. Refer Figure 6.3.

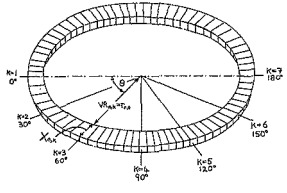


Figure 6.3: The n'th brick course of the vessel lining

Consider the n'th brick course in the lining where $1 \leq n \leq 33$. The surface area of this brick course in contact with the contents of the vessel is approximated by:-

$$dA = 2\pi \int_0^{\pi} (dx \times r_{n,\theta}) d\theta \qquad (6.10)$$

Therefore:-

$$\left(\int dA\right)_{con} + \left(\int dA\right)_{cyl} = 2\pi dx \sum_{n=1}^{33} \left(\int_0^{\pi} r_{n,\theta} d\theta \right) \qquad (6.11)$$

where:-

$$\int_0^{\pi} r_{n,\theta} d\theta = \theta/3 \times (VR_{n,1} + 4 \times (VR_{n,2} + VR_{n,4} + VR_{n,6}) + 2 \times (VR_{n,3} + VR_{n,5}) + VR_{n,7}) \qquad (6.12)$$

Similarly:-

$$\left(\int (1/LT) dA\right)_{con} + \left(\int (1/LT) dA\right)_{cyl} = 2\pi dx \sum_{i=1}^{33} \left(\int_0^{\pi} (r_{n,\theta}/LT_{n,\theta}) d\theta \right) \qquad (6.13)$$

where:-

$$\int_0^{\pi} (r_{n,\theta}/LT_{n,\theta}) d\theta = \theta/3 \times (VR_{n,1}/Y_{n,1} + 4 \times (VR_{n,2}/Y_{n,2} + VR_{n,4}/Y_{n,4} + VR_{n,6}/Y_{n,6}) + 2 \times (VR_{n,3}/Y_{n,3} + VR_{n,5}/Y_{n,5}) + VR_{n,7}/Y_{n,7}) \qquad (6.14)$$

Note that $VR_{n,k}$ is the inner radius and $Y_{n,k}$ is the thickness of the lining (working lining plus backup lining) at brick layer n and radial position k. Thus:-

$$VR_{n,k} = r_{i,n} \qquad (6.15)$$

where:-

θ = TT×(k-1)×30/180 = (k-1)×TT/6 radians (6.16)

For $1 \leq n \leq 15$ (ie. lower conical section):-

$$VR_{n,k} = 1.476 + 0.04 \times n - Y_{n,k} \qquad (6.17.1)$$

where $Y_{n,k}$ is the lining thickness (including backup lining) at brick layer n and radial position k:-

$$Y_{n,k} = LT_{1,n,k} + 0.138 - (LT_{1,n,k} - LT_{2,n,k}) \times VL_1/VL_2 \qquad (6.18)$$

Note that $LT_{1,n,k}$ and $LT_{2,n,k}$ are the thicknesses of a new and worn out working lining at brick layer n and radial position k. Refer to chapter 5.

For $16 \leq n \leq 33$ (ie. cylindrical section):-

$$VR_{n,k} = 2,635 - Y_{n,k} \qquad (6.17.2)$$

where $Y_{n,k}$ is given by equation 6.18 above.

6.2.4 Vessel dome

In the case of the dome it assumed that the lining thickness remains more or less constant throughout the life of the lining. Furthermore, lining thickness in this section is uniform irrespective of position.

Thus it can be shown from the geometry of the vessel dome and its lining that:-

$$(\int dA)_{DOM} = TT*((0,475+1,745)*2,54-(0,475+0,75)*1,5/2) \qquad (6.19)$$

and:-

$$(\int (1/LT)dA)_{DOM} = (\int dA)_{DOM}/0,26 \qquad (6.20)$$

6.2.5 Total vessel lining

The total lining "hot face" surface area A_{LIN} is given by by combining equations 6.7, 6.11 and 6.19:-

$$A_{LIN} = (\int dA)_{HOT}+(\int dA)_{CON}+(\int dA)_{CYL}+(\int dA)_{DOM} \qquad (6.21)$$

The equivalent lining thickness Y_{LIN} is given by combining equations 6.21, 6.9, 6.13, and 6.20:-

$$Y_{LIN} = A_{LIN}/((\int (1/LT)dA)_{HOT}+(\int (1/LT)dA)_{CON} + (\int (1/LT)dA)_{CYL}+(\int (1/LT)dA)_{DOM}) \qquad (6.22)$$

In the model, A_{LIN} and Y_{LIN} are calculated at the start of each new heat.

7 MODEL FOR THE UNSTEADY STATE HEAT FLOW THROUGH THE REFRACTORY LINING

7.1 Introduction

As a simplifying approximation the vessel lining is modelled as a parallel sided plate of equivalent thickness $Y_{L.EQ}$ and surface area $A_{L.EQ}$. The calculation of $Y_{L.EQ}$ and $A_{L.EQ}$ is discussed in detail in chapter 6.

In order to calculate the heat flux between the contents of the vessel and the lining, it is necessary to calculate the temperature distribution through the lining. Knowing the temperature distribution, the temperature gradient of the incremental thickness of lining in direct contact with the contents of the vessel can be used to estimate the heat flux through the metal/lining interface.

The equation for unsteady state heat flow through the lining is solved numerically for each process time step.

7.2 Mathematical Formulation of the Model

7.2.1 Numerical formulation of the unsteady state heat flow through the lining

Consider figure 7.1 below:-

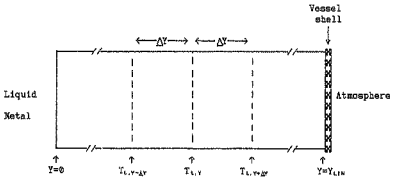


Figure 7.1: Finite element model of temperature distribution and heat flow through the refractory lining

In figure 7.1, $T_{t,Y}$ is the temperature of the lining at position Y from the metal/refractory interface at time t since the start of a heat.

For $0 \leq Y \leq Y_{LIN}$ the equation of unsteady state heat flow is given by:-

$$\alpha \times d^2T/dY^2 = dT/dt \qquad (7.1)$$

α is the thermal diffusivity of the lining and is given by:-

$$\alpha = k_{LIN}/(C_p \times \rho_{LIN}) \qquad (7.2)$$

where:-

k_{LIN} = thermal conductivity of lining;

ρ_{LIN} = density of lining;

C_p = heat capacity (specific heat) of lining.

The last three variables are functions of temperature and the development of an empirical equation for $\alpha = f(T)$ is presented in section 7.2.2.

The boundary conditions for the differential equation 7.1 are:-

(i) $T_{0,Y} = f(Y)$ at $t = 0$ for $0 \leq Y \leq Y_{LIN}$ (7.3)

Before initially charging the first heat into a newly lined vessel, for example, a linear temperature gradient is assumed to exist.

(ii) $T_{t,Y_{LIN}} = T_W(t)$ for $\sum_{j=1}^{n} t_{B,j} \leq t < \sum_{j=1}^{n+1} t_{B,j}$ and $Y = Y_{LIN}$ (7.4)

where n refers to the n'th process time step (of duration $t_{B,n}$) since the creation of the initial linear temperature gradient.

$T_W(t)$, the shell temperature, is calculated from a heat balance taking into account heat flux from the lining and heat flux out to the atmosphere. This is discussed later in section 7.2.4.

(iii) $T_{t,0} = T_B(t)$ for $\sum_{j=1}^{n} t_{B,j} \leq t < \sum_{j=1}^{n+1} t_{B,j}$ and $Y = 0$ (7.5)

where $T_B(t)$ is the temperature of the liquid metal and slag in the vessel.

It can be shown (Ref.5, p191), by applying Taylor's series expansions, that the differential terms can be expressed as:-

$$d^2T/dY^2 = (T_{t,Y+\Delta Y} - 2*T_{t,Y} + T_{t,Y-\Delta Y})/\Delta Y^2 \qquad (7.6)$$

and:-

$$dT/dt = (T_{t+\Delta t,Y} - T_{t,Y})/\Delta t \qquad (7.7)$$

Substituting equations 7.6 and 7.7 into 7.1:-

$$\alpha * (T_{t,Y+\Delta Y} - 2*T_{t,Y} + T_{t,Y-\Delta Y})/\Delta Y^2 = (T_{t+\Delta t,Y} - T_{t,Y})/\Delta t \qquad (7.8)$$

Thus:-

$$T_{t+\Delta t,Y} - T_{t,Y} = \alpha * (T_{t,Y+\Delta Y} - 2*T_{t,Y} + T_{t,Y-\Delta Y}) * \Delta t/\Delta Y^2 \qquad (7.9.1)$$

In the model, the refractory lining temperature profile is stored in a matrix RT. Thus equation 7.9.1 can be re-written in terms of RT:-

$$RT_{2,j} = RT_{1,j} + \alpha * (RT_{1,j-1} - 2*RT_{1,j} + RT_{1,j+1}) * t_s/\Delta Y^2 \qquad (7.9.2)$$

where:-

$RT_{1,j}$ = temperature of lining at position j (ie. a distance (j-1)*dY) from the metal/refractory interface at time t;

$RT_{2,j}$ = temperature of lining at position j at time $t+\Delta t$;

α = thermal diffusivity of lining at position j at start of a process time step;

t_s = Δt = duration of process time step;

ΔY = distance between position j and j+1.

Note that:-

$$\Delta Y = Y_{LIN}/(n-1) \qquad (7.10)$$

for n-1 equal distance increments between the hot face of the lining and the vessel shell. Refer to figure 7.2.

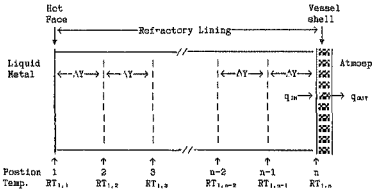


Figure 7.2: Schematic subdivision of vessel lining into incremental distance elements for unsteady state heat flow calculations. Lining temperatures at the start of a process time step and heat fluxes in and out of the vessel shell are shown

7.2.2 Temperature dependence of refractory lining thermal diffusivity

For the determination of the temperature dependence of the thermal diffusivity of the refractory lining, refer to figure 7.3 (from data sheet for Wulfrath dolomite bricks SINDORDREM K, fired, direct bonded).

From the plot of % thermal expansion as a function of temperature, the following equation can be derived for the density of the lining as a function of temperature:-

$$\rho_{LIN}(T) = 2775/(0,9954+1,3E-5T)^3 \qquad (7.11)$$

The plot of thermal conductivity versus temperature was re-plotted on an expanded temperature scale ranging from 273°K to 2073°K. See figure 4. An assumption was made that at 273°K the thermal conductivity is $\approx 3,38\times10^{-3}$ kJ/m/s/°K and that at 2073°K it is $\approx 2,42\times10^{-2}$ kJ/m/s/°K. The missing data points were graphically interpolated using a "Flexicurve". A best fit cubic equation was determined using the standard least squares regression technique.

Thus, $k_{LIN}(T)$ the thermal conductivity of the lining, as a function of temperature (in degrees Kelvin), is approximated by:-

$$k_{LIN}(T) = 3,314E-3+1,351E-6T-2,267E-9T^2+6,083E-13T^3 \quad kJ/m/s/T \qquad (7.12)$$

Dolomite bricks SINDOFORM® K, fired, direct bonded

Chemical composition (pitch free basis)

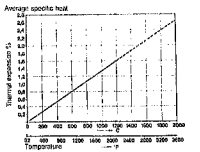
MgO	%	> 96
CaO	%	< 01
SiO_2	%	< 1.5
$Al_2O_3 + Mn_2O_3$	%	< 1.0
Fe_2O_3	%	< 1.0

Physical properties
(Values in brackets refer to unimpregnated material)

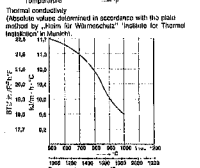
Quality impregnated* / unimpregnated	12101 (11101)	12103 (11103)	12104 —
Bulk density g/cm³	2.86-2.85 (2.70-2.85)	2.75-2.85 (2.6-2.7)	2.7-2.8
lb/ft³	178 to 184 (169 to 178)	172 to 178 (162 to 169)	169 to 175 —
Total porosity % by volume	(17-21)	(20-24)	(24-27)
Cold crushing strength N/mm² psi	> 35 > 5075	> 25 > 3630	> 10 > 1450
Permeability mPa	(5-30)	(70-80)	(400)
Refractoriness-underload 0.196 N/mm² (28.4 psi) t_0 °C	> 1700 (> 3452°F)	> 1700 (> 3092°F)	> 1700 (> 3092°F)
$t_{0.5}$ °C	> 1690 (> 3452°F)	> 1700 (> 3452°F)	> 1700 (> 3452°F)
Thermal shock resistance (950°C/1.2 bar) Number of cycles quenched with air	< 10	> 20	> 60

*Impregnation material < 6 %

The physical properties are the normal values of samples taken from lots of production. They may in the are additionally influenced by the other shapes.



Thermal conductivity
(Absolute values determined in accordance with the plate method by „Institut für Wärmetechnik" Institute for Thermal Insulation in Munich).



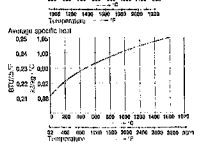


Figure 7.3: Data sheet for Wulfrath SINDOFORM K fired, direct bonded, dolomite bricks

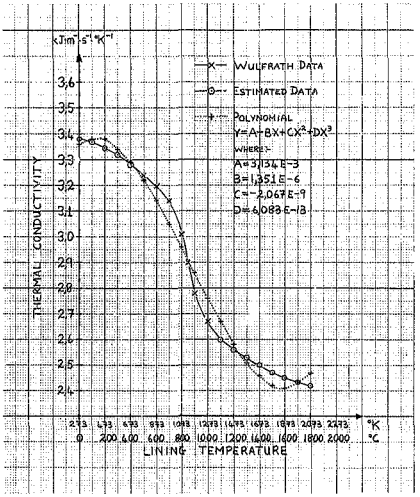


Figure V.4: Temperature dependence of the thermal conductivity of dolomite bricks

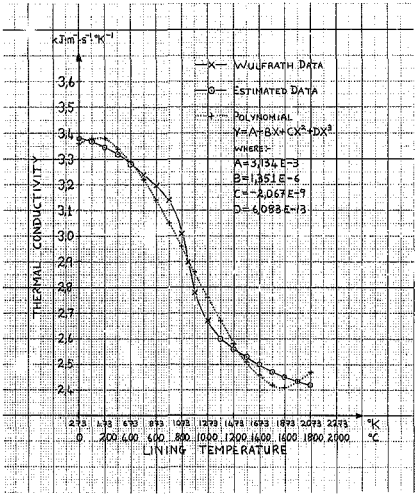


Figure V.4: Temperature dependence of the thermal conductivity of dolomite bricks

The temperature dependence of the specific heat (or heat capacity) of the lining was determined by fitting a logarithmic function to the third graph of figure 3 using the least squares technique. Thus Cp is given by:-

$$Cp = 0,437+0,060*LnT \quad kJ/kg/°K \qquad (7.13)$$

By combining equations 7.11, 7.12 and 7.13, an approximation of the thermal diffusivity of the lining as a function of temperature is given by:-

$$\downarrow(T) = (3,314E-3+1,351E-6*T-2,069E-9*T+6,083E-13*T^3)$$
$$/((2775/(0,9964+1,3E-5*T)^3)*(0,437+0,06*LnT)) \qquad (7.14)$$

Estimation of the heat flow rate between the vessel contents and the refractory lining

In order to estimate the heat flux from the liquid metal into the refractory lining, the incremental thickness of lining in contact with the liquid metal is considered. Referring to figure 7.2, this corresponds to the segment between position 1 and 2. For the duration of an incremental process time step Δt, it is assumed that there is an approximately linear temperature gradient between these two points. Furthermore, it is assumed that the net heat accumulation (or loss) rate within this incremental thickness of lining is so small in comparison with the heat flow rate through it that the former can be ignored.

The average thermal conductivity K'_{LIN} of the segment is calculated using equation 7.12 and the mean RT_{AV} of the temperatures $RT_{1,1}$ and $RT_{1,2}$:-

$$K'_{LIN} = 3,314E-3+1,351E-6*RT_{AV}$$
$$-2,069E-9*RT_{AV}^2+6,083E-13*RT_{AV}^3 \quad kJ/m/s/°K \qquad (7.15)$$

where:-

$$RT_{AV} = (RT_{1,1}+RT_{1,2})/2 \qquad (7.16)$$

Note that:-

$$RT_{1,1} = T_B(t) \qquad (7.17)$$

where $T_B(t)$ is the temperature of the liquid metal and slag in the vessel at time t.

The heat flow rate $Q_{LIN}(t)$ between the lining and vessel contents is given by:-

$$Q_{LIN}(t) = A_{LIN}*K'_{LIN}*(T_B(t)-RT_{1,2})/\Delta Y \quad kJ/s \qquad (7.18)$$

where A_{LIN} is the "hot face" surface area of the lining as calculated in chapter 6.

7.2.4 Estimation of the vessel shell temperature

Referring to figure 7.2, the heat flux $q_{lm}(t)$ from the lining into the steel shell of the vessel is approximately given by:-

$$q_{lm}(t) = (RT_{l,n-1}-T_{vs}(t))*k^{t}_{lin}/\Delta Y \qquad (7.19)$$

where:-

$q_{lm}(t)$ = heat flux into vessel shell (kJ/m²/s);

$RT_{l,n-1}$ = temperature of the refractory lining at a distance ΔY from the metal shell/refractory interface at the start of the k'th process time step;

n-1 = number of distance increments through the refractory lining used in the numerical solution of equation 7.1 as given by 7.9.2;

$T_{vs}(\ )$ = temperature of the vessel shell at the start of the k'th process time step;

k^{t}_{lin} = thermal conductivity of lining (evaluated at the mean temperature between positions n-1 and n).

The heat flux out of the vessel shell is the sum of the convective heat flux $q_{conv}(t)$ and the radiation heat flux $q_{rad}(t)$.

The heat transfer coefficient $h_{conv}(t)$ for convective heat transfer is estimated assuming turbulent flow past a vertical plate (Ref.5, p239):-

$$h_{conv}(t) = 1,9E-3*(T_{vs}(t)-T_{atm})^{0,25} \qquad (7.20)$$

where $T_{vs}(t)$ and T_{atm} are the vessel shell and ambient temperatures (°K) respectively. The convective heat flux $q_{conv}(t)$ is given by:-

$$q_{conv}(t) = (T_{vs}(t)-T_{atm})*h_{conv}(t) \qquad (7.21)$$

Therefore:-

$$q_{conv}(t) = (T_{vs}(t)-T_{atm})^{1,25}*1,9E-3 \quad kJ.m^{-2}.s^{-1} \qquad (7.22)$$

The radiant heat flux $q_{rad}(t)$ is given by:-

$$q_{rad}(t) = (T_{vs}(t)^{4}-T_{atm}^{4})*5,732E-11*(0,91+9E-5*T_{vs}(t)) \qquad (7.23)$$

where the term $(0,91+9E-5*T_{vs}(t))$ is the emissivity of mild steel plate as a function of temperature (Ref.5, p.65).

Therefore, the total heat flux $q_{tot}(t)$ out of the vessel shell is given by:-

$$q_{tot}(t) = q_{conv}(t)+q_{rad}(t)$$

$$= (T_{vs}(t)-T_{atm})^{1.25}*1,9E-3 + (T_{vs}(t)^4-T_{atm}^4)*5,732E-11*(0,91*9E-5*T_{vs}(t)) \qquad (7.24)$$

The rise in temperature of the shell per process time step t_s is given by:-

$$\Delta T = t_s*(q_{in}(t)-q_{out}(t))/(Y_{vs}*\rho_s*C_{p,s}) \qquad (7.25)$$

where:-

Y_{vs} = thickness (m) of the vessel shell

ρ_s = density (kg/m³) of steel plate

$C_{p,s}$ = specific heat (kJ/kg/°K) of steel plate

Therefore the shell temperature at time $t+\Delta t$ is given by:-

$$T_{vs}(t+\Delta t) = T_{vs}(t)+t_s*(q_{in}(t)-q_{out}(t))/(Y_{vs}*\rho_s*C_{p,s}) \qquad (7.26)$$

7.3 Results

The calculated development of a temperature profile with time in a new AOD vessel lining is shown in figure 7.5. below. A dimensionless distance of 0 represents the vessel shell and 1 represents the refractory "hot face" exposed to the vessel contents.

The initial boundary conditions were as follows:-

(i) Shell temperature: 150°C

(ii) Refractory "hot face" temperature: 1000°C

(iii) A linear temperature gradient was assumed to exist between (i) and (ii) above.

This is a rough approximation of the temperature distribution that might exist in the refractory lining of a newly lined vessel immediately before charging the first heat.

It represents an extreme case of unsteady state heat flow through the refractory lining and is easy to represent graphically because of the wide range of "hot face" temperatures.

At t=0 the hot face temperature was raised to 1480°C by charging a standard 50 000 Kg 304 type charge. Blowing commenced immediately with a 3:1 O_2:N_2 ratio (ie. 45m³O₂/min':15m³O₂/min'). The time associated with charging prior to commencing the blow was ignored

Therefore, the total heat flux $q_{ovr}(t)$ out of the vessel shell is given by:-

$$q_{ovr}(t) = q_{mow}(t)+q_{mo}(t)$$

$$= (T_{vr}(t)-T_{amb})*1,9E-3 + (T_{vr}(t)^4-T_{amb}^4)*5,732E-11*(0,91+9E-5*T_{vr}(t)) \quad (7.24)$$

The rise in temperature of the shell per process time step t_s is given by:-

$$\Delta T = t_s*(q_{in}(t)-q_{ovr}(t))/(Y_{vs}*\rho_{s,s}*C_{p,s}) \quad (7.25)$$

where:-

Y_{vs} = thickness (m) of the vessel shell

$\rho_{s,s}$ = density (kg/m³) of steel plate

$C_{p,s}$ = specific heat (kJ/kg/°K) of steel plate

Therefore the shell temperature at time $t+\Delta t$ is given by:-

$$T_{vs}(t+\Delta t) = T_{vs}(t)+t_s*(q_{ins}(t)-q_{ovr}(t))/(Y_{vs}*\rho_{s,s}*C_{p,s}) \quad (7.26)$$

7.3 Results

The calculated development of a temperature profile with time in a new AOD vessel lining is shown in figure 7.5. below. A dimensionless distance of 0 represents the vessel shell and 1 represents the refractory "hot face" exposed to the vessel contents.

The initial boundary conditions were as follows:-

(i) Shell temperature: 150°C

(ii) Refractory "hot face" temperature: 1650°C

(iii) A linear temperature gradient was assumed to exist between (i) and (ii) above.

This is a rough approximation of the temperature distribution that might exist in the refractory lining of a newly lined vessel immediately before charging the first heat.

It represents an extreme case of unsteady state heat flow through the refractory lining and is easy to represent graphically because of the wide range of "hot face" temperatures.

At t=0 the hot face temperature was raised to 1680°C by charging a standard 50 000 Kg 304 type charge. Blowing commenced immediately with a 3:1 O_2:N_2 ratio (i.e. 45m³O₂min⁻¹:15m³O₂min⁻¹). The time associated with charging prior to commencing the blow was ignored

in the simulation.

The temperature distribution in the lining was then calculated at fifteen second intervals as the bath temperature rose from 1480°C to 1753°C over a sixteen minute period. The bath temperature at various times is indicated for a dimensionless distance equal to one.

For sake of clarity, the temperature distribution is shown at t=1,4,8,12 and 16 minutes. Also shown is the linear temperature gradient immediately before charging (ie.t<0).

The development of the temperature profile on the "hot face" side of the lining follows an expected pattern. The calculated temperatures unfortunately cannot be verified on a plant scale because temperature measuring equipment has not been installed in a lining.

The developing profile on the vessel shell side of the lining is interesting as it suggests that the initial shell temperature of 150°C was set too low. Heat is accumulating in the vessel shell because the heat input rate (conduction from the outer surface of the refractory lining) exceeds the rate of heat loss to the surroundings (radiation and convection).

The unsteady state heat transfer model has in general been found to be stable provided that, in extreme cases as above, the integration time step length is not too long (ie. >20s). Longer time step lengths can be tolerated once a nearly steady state temperature profile has been established.

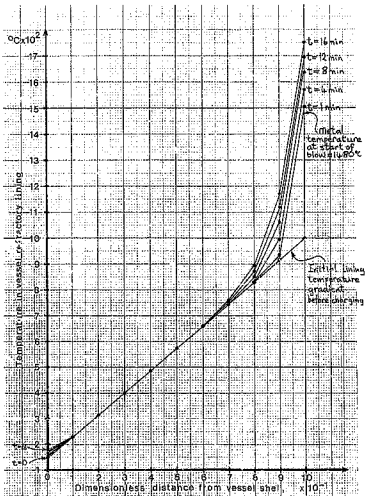


Figure 7.5: Calculated temperature profile development in a new refractory lining.

8 THE UNIFIED AOD PROCESS MODEL

8.1 Introduction

The AOD process consists of a number of distinct stages or phases:-

(i) decarburization of the liquid metal when a mixture of oxygen and an inert gas are simultaneously blown into the vessel;

(ii) charging of alloying materials and/or fluxes for temperature and chemistry control of the metal and slag;

(iii) stirring of the liquid metal and slag when only an inert gas is blown into the vessel. Stirring is normally of short duration and is associated with rotating the vessel in and out of the blowing position or for stirring in alloys and fluxes. Under certain circumstances (such as when there are high concentrations of dissolved oxygen in the liquid metal and metal oxides in the slag) decarburization of the liquid metal may still proceed;

(iv) charging and stirring in of ferro-silicon or other suitable reducing agents (normally in conjunction with fluxes for slag chemistry control) for reducing the accumulated metal oxides in the slag at the end of the decarburization phase;

(v) waiting periods (eg. for sampling, temperature measurement, de-slagging, tapping or plant delays) when the the vessel is turned on its side and stagnant conditions exist in the bath. Waiting periods may also include times when the vessel is empty.

As discussed in the preceeding chapters, decarburization is achieved by injecting a mixture of oxygen and inert gas into the liquid metal via the tuyeres. Bubbles are formed and start to rise up through the metal bath.

Initially, in the tuyere reaction zone model, gaseous oxygen reacts with various metallic phase elements to form an oxide mixture at the metal/gas interface of each bubble. Some carbon monoxide is also formed. The rate of formation of each oxide is dependent on the rate of diffusion of the corresponding element through the boundary layer surrounding each bubble. Each bubble is rapidly depleted of its oxygen content. Simultaneously, there is mass transfer of nitrogen in or out of each bubble. The mass transfer rate of nitrogen is also dependent on its diffusion rate through the boundary layer.

In the case where only an inert gas is being blown (eg. during backtilting of the vessel to charge additions or stirring in of additions), the tuyere reaction zone model does not apply.

Bubbles leaving the tuyere reaction zone are essentially depleted of gaseous oxygen. The oxide mixture disengages from the bubbles to form droplets in the liquid metal. These droplets and bubbles rise up, in close association with one another in a plume, through the rising bubble reaction zone.

As the bubbles rise up through the rising bubble reaction zone, carbon and oxygen dissolved in the bulk liquid metal diffuse through the boundary layer surrounding each bubble. They react at the metal/gas interface of the bubbles to form carbon monoxide.

Oxygen is removed from the liquid metal by the decarburization reaction. However, there is a simultaneous input of oxygen into the liquid metal from the dissociation of metal oxides contained in the oxide particles (and slag).

Simultaneously, metal oxides in the oxide droplets dissociate to replenish the oxygen removed by the decarburization reaction.

Silicon, being a strong reducing agent, diffuses from the bulk metal phase to the surface of the oxide particles and reduces some of the oxides present to f

In the case where only a[illegible] being blown in at the tuyeres the oxide partic[illegible] formed. Oxygen for the decarburization reaction is [illegible] from the bulk liquid metal, causing the dissolved oxygen concentration to fall off accordingly.

Nitrogen also continues to diffuse in or out of the bubbles, depending on the partial pressure of nitrogen in the bubbles at a particular depth and the nitrogen content of the bulk liquid metal.

Oxide particles that reach the metal/slag interface are assumed to be captured by the slag layer floating on the metal surface. Although not taken into account at present, there are a number of reactions at the slag/metal interface that could be considered. These include the following possibilities:-

(i) dissociation of metal oxides to augment the supply of dissolved oxygen in the metal as it is depleted by the decarburization reaction;

(ii) reduction of metal oxides by silicon dissolved in the liquid metal;

(iii) reduction of thermodynamically less stable metal oxides (eg. FeO, MnO, Mn_3O_4) in the slag by more reactive elements in the liquid metal (eg. Cr, Mn).

The nett formation of metal oxides (eg. Cr$_2$O$_3$) in their accumulation in the slag layer and a depletion of the corresponding elements in the liquid metal. Similarly, the formation of [illegible] which eliminates

escapes from the vessel mouth) results in a corresponding depletion of carbon in the liquid metal. Nitrogen may also accumulate or be removed from the liquid metal. These changes are taken into account in the model by means of differential mass balances for the metal and slag phases.

The original model included an oxygen balance that took into account the oxygen concentration in the bulk liquid metal phase. Subsequently a simpler oxygen balance was implemented that directly coupled the oxygen transfer between oxide particles and bubbles. As previously discussed, this was a rather artificial solution to what was essentially a numerical analysis problem (ie. to avoid computational difficulties associated with the numerical solution of "stiff" simultaneous differential equations). It was achieved, as discussed in chapter 4, by coupling the decarburization reaction and the oxide particle dissociation reactions.

However, with the need to take slag/metal reactions and/or stirring with inert gases into account becoming more evident, an oxygen balance that takes into account the oxygen concentration in the bulk liquid metal phase will have to be re-introduced. This is feasible now that suitable numerical routines[4,5] are available for solving "stiff" simultaneous differential equations.

The formation of metal oxides and CO, while oxygen is being injected, are highly exothermic processes. Simultaneously there is substantial heat loss from the metal/slag system via radiation, conduction and heat in the exhaust gases. The accumulation of heat in the system causes the temperature to rise continuously during the decarburization process. The change of the heat content of the metal and slag is taken into account by means of a generalized differential heat balance. The differential heat balance can also be applied to inert gas stirring situations.

The effect that charging alloying materials and fluxes has on bath chemistry and temperature is taken into account with suitable mass and heat balances.

8.2 Mass Balances

8.2.1 Mass balances during gas decarburization process

The net formation rate of the i-th oxide M_iO_j is the rate at which it accumulates in the slag layer floating on the surface of the liquid metal. This is the same as the rate at which the oxide M_iO_j leaves the rising bubble reaction zone and enters the slag layer floating on the surface of the liquid metal (less the loss-back rate of the oxide in the slag to the zone where slag/metal reaction is taken into consideration). Thus:

$$\frac{dN_{M_iO_j}}{dt} = N_{M_iO_j}(t) \qquad (8.1)$$

where:-

$N_{SLG,n}(t)$ is the quantity (kgmol) of the n'th oxide M_xO_y in the slag;

$N'_{OX,n}(t)$ is the integrated flow rate of the n'th oxide M_xO_y leaving the rising bubble reaction zone (less the reduction rate of M_xO_y in the slag, if this is taken into account).

Therefore, the quantity of the n'th oxide M_xO_y in the slag at time $t+\Delta t$ is given by:-

$$N_{SLG,n}(t+\Delta t) = N_{SLG,n}(t)+\int_{t}^{t+\Delta t} N'_{OX,n}dt \qquad (8.2)$$

The depletion rates of the metal phase elements are stoichiometrically proportional to the corresponding oxide formation rates. Thus:-

$$dN_{MET,n}(t)/dt = -x_{x,n}xN'_{OX,n}(t) \qquad (8.3)$$

where:-

$N_{MET,n}(t)$ is the quantity (kgmol) of the n'th element M in the liquid metal;

$x_{x,n}$ is equivalent to x in the n'th oxide M_xO_y.

Therefore, the quantity of the n'th element in the liquid metal at time $t+\Delta t$ is given by:-

$$N_{MET,n}(t+\Delta t) = N_{MET,n}(t)-x_{x,n}x\int_{t}^{t+\Delta t} N'_{OX,n}.t)dt \qquad (8.4)$$

The carbon depletion rate of the liquid metal is equal to the flow rate of carbon monoxide in the bubbles leaving the rising bubble reaction zone (and leaving the vessel). Thus:-

$$dN_{MET,C}(t)/dt = -N'_{CO}(t) \qquad (8.5)$$

where:-

$N_{MET,C}(t)$ is the quantity of carbon (kgmol) in the liquid metal;

$N'_{CO}(t)$ is the flow rate (kgmol/s) of carbon monoxide leaving the vessel.

Therefore, the quantity of carbon in the liquid metal at time $t+\Delta t$ is given by:-

$$N_{MET,C}(t+\Delta t) = N_{MET,C}(t) - \int_{t}^{t+\Delta t} N'_{CO}(t)dt \qquad (8.6)$$

The depletion rate of nitrogen in the liquid metal is proportional to the difference between the flowrate of nitrogen in the bubbles leaving the rising bubble reaction zone (ie. leaving the vessel) and the flowrate of nitrogen to the tuyeres.

Thus:-

$$dN_{MET,N}(t)/dt = -2*(N'_{N2}(t) - G_{F,N2}) \qquad (8.7)$$

where:-

$N_{MET,N}(t)$ is the quantity (kgmol N) of nitrogen dissolved in the liquid metal;

$N'_{N2}(t)$ is the flowrate (kgmol N_2/s) of nitrogen leaving the vessel;

$G_{F,N2}$ is the flowrate (kgmol N_2/s) of nitrogen entering the vessel via the tuyeres.

Therefore, the quantity of dissolved nitrogen in the liquid metal at time $t+\Delta t$ is given by:-

$$N_{MET,N}(t+\Delta t) = N_{MET,N}(t) - \int_{t}^{t+\Delta t} (N'_{N2}(t) - G_{F,N2})dt \qquad (8.8)$$

8.2.2 Mass balances associated with charging vessel additions

It is necessary to make additions of alloying materials and fluxes to the vessel during the decarburization process. There are three main reasons for this:-

(i) for "homing in" on the final aim composition range of the particular steel type being produced;

(ii) to provide coolant to maintain the temperature of the process within the desired operating range;

(iii) to ensure sufficient CaO and MgO in the slag for lining protection (against attack by SiO_2 in the slag) and desulphurization purposes.

When metallic additions (eg. charge chrome, ferro-manganese, ferro-molybdenum, mild steel scrap, nickel, etc.) are made, the mass balance for the k'th element in liquid metal is given by:-

$$N_{MET,k}(new) = N_{MET,k}(old)+(\sum_{j=1}^{n}(m_{ALOY,j}*\%M_{j,k}))/(100*M_k) \qquad (8.9)$$

where:-

$N_{MET,k}$ is the quantity (kgmol) of element k in the liquid metal;

$m_{ALOY,j}$ is the mass (kg) of the j'th alloying material charged;

$\%M_{j,k}$ is the concentration (%) of element k in the j'th alloying material;

M_k is the atomic mass (kg/kgmol) of the k'th element.

When fluxes (eg. lime or dolomitic lime) are added, the mass balance for the k'th oxide in the slag is given by:-

$$N_{SLG,k}(new) = N_{SLG,k}(old)+(\sum_{j=1}^{n}(m_{FLUX,j}*\%M^{\prime}_{j,k}))/(100*M_{MT,k}) \qquad (8.10)$$

where:-

$N_{SLG,k}$ is the quantity (kgmol) of the k'th oxide in the slag;

$m_{FLUX,j}$ is the mass (kg) of the j'th fluxing material charged;

$\%M^{\prime}_{j,k}$ is the concentration (%) of oxide k in the j'th fluxing material;

$M_{MT,k}$ is the molecular mass (kg/kgmol) of the k'th oxide.

8.3 Heat Balance

8.3.1 Heat balance during the decarburization process

The main sources of heat input to the liquid metal and slag in the vessel are as follows:-

(i) exothermic formation of carbon monoxide and metal oxides;

(ii) heat content of gases entering the vessel via the tuyeres (as an approximation, this can be ignored when the standard state for the relevant thermodynamic data is one atmosphere and 25°C);

(iii) conduction of heat from the lining (if the lining adjacent to the "hot face" is hotter than the vessel contents).

Simultaneously heat is lost from the liquid metal and slag in the vessel via:-

(i) conduction of heat into the vessel lining (if the lining adjacent to the "hot face" is colder than the vessel contents);

(ii) radiation of heat via the vessel mouth;

(iii) heat contained in the hot gases (and dust, which is ignored) leaving the vessel mouth.

Thus the rate of heat accumulation in the liquid metal and slag is given by:-

$$dH_{melt}(t)/dt = Q_R(t)+Q_{TUYERE}-Q_{HOTGAS}(t)-Q_{RAD}(t)-Q_{LINE}(t) \qquad (8.11)$$

where:-

$H_{melt}(t)$ is the heat content (kJ) of the liquid metal and slag in the vessel;

$Q_R(t)$ is the rate of heat generation (kJ/s) from the formation of carbon monoxide and the oxides of other metal phase elements and is given by:-

$$Q_R(t) = \sum_{M=A}^{n} (\dot{M}_{OX,M}(t)*\Delta H^o_R(T_S(t))) + \dot{M}'_{CO}(t)*\Delta H^o_{CO}(T_S(t)) \qquad (8.12)$$

where:-

$\Delta H^o_R(T_S(t))$ is the standard heat of formation of the 'th oxide M_xO_y. $T_S(t)$ is the temperature of the liquid metal and slag;

Q_{TUYERE} is the rate of heat input (kJ/s) by the gases entering the vessel through the tuyeres. For the model in its present form, Q_{TUYERE} is taken to be zero;

$Q_{HOTGAS}(t)$ is the rate of heat loss (kJ/s) via the hot gases leaving the vessel mouth and is given by:-

$$Q_{HOTGAS}(t) = \sum_{j=1}^{4} (\dot{N}'_{GAS,j}(t)*H_{GAS,j}(T_S(t))) \qquad (8.13)$$

where:-

$H_{mat,j}(T_s(t))$ is the standard heat content or enthalpy of the j'th gas leaving the vessel at a temperature $T_s(t)$.

$Q_{rad}(t)$ is the rate of heat loss (kJ/s) via radiation from the vessel mouth and is given by:-

$$Q_{rad}(t) = A_{mouth} F_v \sigma (T_s(t)^4 - T_{atm}^4) \qquad (8.14)$$

where:-

A_{mouth} is the cross sectional area of the vessel mouth;

F_v is an empirically determined "view factor". A true view factor cannot be easily evaluated because of difficult to quantify effects such as slag build-up in the vessel mouth, dense metal oxide fumes in the exhaust gases and back-radiation from the refractories lining the gas offtake hood:

σ is the Stephan-Boltzmann constant (5.67x10^{-11} kW/m^2/°K^4)

T_{atm} is the ambient temperature of the surroundings.

$Q_{lin}(t)$ is the rate of heat loss (kJ/s) via conduction into the vessel lining and is given by:-

$$Q_{lin}(t) = A_{lin} k_{T_{lin}} (T_s(t) - T_{T_{lin}}) / \Delta T \qquad (8.15)$$

The derivation of equation 8.15 and the definition of the symbols used is presented in section 7.2.3 (ie. equation 7.18).

Therefore, the relative heat content $H_{metal}(t+\Delta t)$ of the liquid metal and slag at time $t+\Delta t$ is given by:-

$$H_{metal}(t+\Delta t) = H_{metal}(t) + \int_{t}^{t+\Delta t} (Q_R(t) + Q_{thermal} - Q_{thermal}(t) - Q_{rad}(t) - Q_{lin}(t))dt \qquad (8.16)$$

The sensible heats of the component elements and oxides are used in a linearised form applicable over the temperature range 1450-1750°C (1723-2023°K) and are relative to a standard temperature of 25°C (298°K). The data was derived from tables presented in reference 16.

Therefore the temperature independent term CB_t of the overall heat capacity of the liquid metal and slag is given by:-

$$CB_t = \sum_j (N_{met,j}(t+\Delta t) HM_{t,j}) + \sum_j (N_{slag,j}(t+\Delta t) HO_{t,j}) \qquad (8.17)$$

and the temperature dependent term CB_2 is given by:-

$$CB_2 = \sum_j (N_{MET,j}(t+\Delta t)*HM_{2,j}) + \sum_k (N_{SLG,k}(t+\Delta t)*HO_{2,k}) \qquad (8.18)$$

where:-

$H_{MATM}(t)$ is the total relative heat content (kJ) of the liquid metal and slag at a temperature $T_B(t)$;

$N_{MET,j}(t)$ is the quantity (kgmol) of the j'th element in the liquid metal;

$HM_{1,j}$ is the temperature independent term of the sensible heat (kJ/kgmol) of the j'th element in the liquid metal;

$HM_{2,j}$ is the temperature dependent term of the sensible heat (kJ/kgmol/°K) of the j'th element in the liquid metal;

$N_{SLG,k}(t)$ is the quantity (kgmol) of the k'th oxide in the slag;

$HO_{1,k}$ is the temperature independent term of the sensible heat (kJ/kgmol) of the k'th oxide in the slag;

$HO_{2,k}$ is the temperature dependent term of the sensible heat (kJ/kgmol/°K) of the k'th oxide in the slag.

Therefore, $T_B(t+\Delta t)$, the new bath temperature at time $t+\Delta t$ is given by:-

$$T_B(t+\Delta t) = (H_{MATM}(t+\Delta t) - CB_1)/CB_2 \qquad (8.19)$$

8.3.2 Heat balance associated with the charging of vessel additions

When alloying materials and/or fluxes are charged to the vessel, there is an associated drop in temperature.

As an approximation, it is assumed that the heat or enthalpy of mixing is negligible and can be ignored. It is assumed that the relative heat contents of the liquid metal, slag, alloys and fluxes are the sums of the relative heat contents of the component elements and oxides in their pure states.

Therefore, the relative heat content (kJ) of the liquid metal and slag, before the additions are made, is given by:-

$$H_{MATM} = \sum_j (N_{MET,j}*(HM_{1,j}+T_B(t)*HM_{2,j})) + \sum_k (N_{SLG,k}*(HO_{1,k}+T_B \cdots HO_{2,k})) \qquad (8.20)$$

When additions are made, $N_{MET,j}$ and $N_{SLG,k}$ are updated as per equations 8.9 and 8.10. Since alloys and fluxes are normally added when they are at ambient temperature (approximately 25°C), their relative heat contents are taken to be zero. Therefore the total

relative heat content H_{new} of the liquid metal and slag remains unchanged.

The temperature independent term CB_1 of the overall heat capacity of the liquid metal and slag is given by:-

$$CB_1 = \sum_j (N_{MET,j}(new) * HM_{1,j}) + \sum_k (N_{M.O,k}(new) * HO_{1,k}) \qquad (8.21)$$

and the temperature dependent term CB_2 is given by:-

$$CB_2 = \sum_j (N_{MET,j}(new) * HM_{2,j}) + \sum_k (N_{M.O,k}(new) * HO_{2,k}) \qquad (8.22)$$

Therefore, after additions have been made, the new bath temperature T_{new} is given by:-

$$T_{new} = (H_{new} - CB_1)/CB_2 \qquad (8.23)$$

8.4 Numerical Solution of the Differential Mass and Energy Balances

8.4.1 Introduction

In order to predict the composition and temperature trajectories of the liquid metal and slag, it is necessary to simultaneously integrate equations 8.1, 8.3, 8.5, 8.7 and 8.11 with respect to process time. Unfortunately these are not simple functions of time and temperature that are amenable to an analytical solution. Therefore *numerical integration techniques* have to be used.

8.4.2 Initialization of variables at the start of the first process time step of a blowing stage

During a heat there are a number of blowing stages. A blowing stage is defined in this context as the period of time during which the vessel is blown with one of the following:-

(i) constant flowrates of one of the inert gas options and oxygen (ie. decarburization);

(ii) a constant flowrate of one of the inert gas options alone (ie. stirring).

A number of variables must be initialized at the start of the first process time step of a particular blowing stage. Some are merely passed on from the preceeding process stage and others require operator or user input. They include the following:-

(i) The masses, composition and temperature of the liquid metal and slag phases;

(ii) The metal volume, tuyere depth and pressure at the tuyeres. The calculation of these variables is discussed in detail in chapter 5;

(iii) The flowrates of the various gases to the tuyeres;

(iv) The maximum temperature or minimum carbon content limits required for the termination of the current decarburization stage.

A number of other variables are also initialized at the start of a blowing stage.-

$$n = 0 \qquad (8.24)$$

where n is the number of completed process time steps since the start of the current blowing stage.

$$t_{min} = 0 \qquad (8.25)$$

where:-

$t_{cum}=\sum t_z$ is the cumulative time elapsed since the start of the current blowing stage.

$N_{MET,i}(0)$ is the quantity (kgmol) of the i'th element in the liquid metal.

$N_{OLG,j}(0)$ is the quantity (kgmol) of the j'th oxide in the slag.

The relative heat content $H_{BATH}(0)$ (kJ) of the bath is given by:-

$$H_{BATH}(0) = \sum_i (N_{MET,i}(0)*(HM_{1,i}+T_B(0)*HM_{2,i}))+\sum_j (N_{SLG,j}(0)*(HO_{1,j}+T_B(0)*HO_{2,j})) \quad (8.26)$$

The definition of the symbols used is presented in section 8.3.1.

8.4.3 Numerical solution of the simultaneous differential equations defining the trajectories of the metal and slag heat content and composition

The basis of the procedure is the numerical integration of equations 8.2, 8.4, 8.6, 8.8 and 8.13 over successive discrete process time intervals of duration t_z ($=\Delta t$). A Runge-Kutta or Bulirsch-Stoer integration method with automatic integration step length control[18,19] can be used.

It is necessary to use a variable integration step length dt in order to overcome the instability problems associated with the numerical solution of "stiff" simultaneous differential equations.

The calculation of the derivatives as defined by equations 8.1, 8.3, 8.5, and 8.7 essentially boils down to the determination of the integrated flow rates $N'_{OX,i}(t)$, $N'_{CR}(t)$ and $N'_{HC}(t)$ (as defined in section 8.2.1). The calculation of these integrated flow rates is the objective of the tuyere reaction zone and rising bubble reaction models.

The calculation of the derivative as defined by equation 8.11 is presented in section 8.2.1.

The bath temperature $T_B(t)$ is calculated using equations analogous to 8.17, 8.18 and 8.19.

8.5 Results

8.5.1 Overall results

The results of simulating a plant scale 316 type heat are presented in figures 8.1 and 8.2.

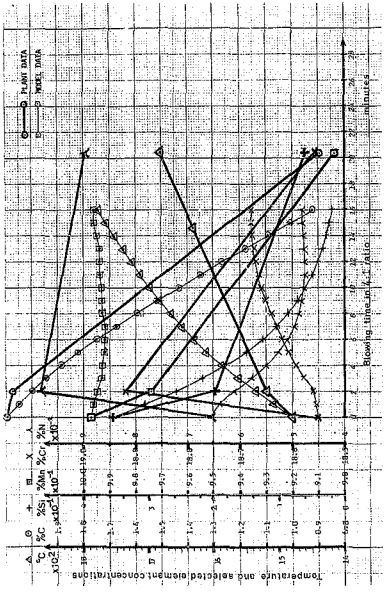


Figure 8.1: Comparison of computed composition and temperature trajectories with actual plant data for a 4:1 blowing step

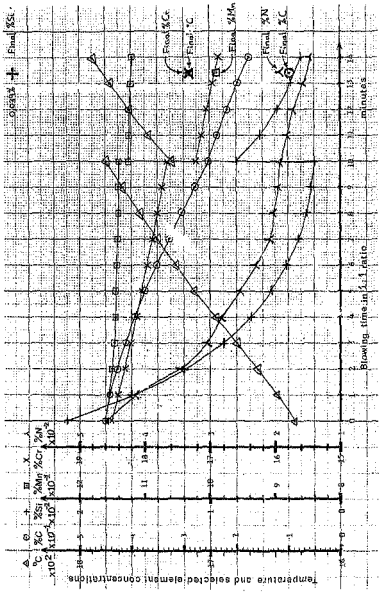


Figure 8.2: Comparison of computed composition and temperature trajectories with actual plant data for a 1:1 blowing step

It should be noted that the blowing time axis represents only that time when oxygen was being blown. The finite times at the start, during sampling and/or temperature measuring and when scrap was charged have not been included. This is because the subroutines for handling these situations (ie. blowing without oxygen) had not been developed at the time of writing. Apart from nitrogen concentration, bath composition and temperature is not expected to change very much except when coolants are charged.

Figure 8.1 is for a 4:1 (ie. $45m^3C_2min^{-1}:12m^3N_2min^{-1}$) blowing ratio. An initial 5mm diameter bubble at the tuyeres was selected. The elements C, Si, Mn and Cr were selected as participating elements. Thus Ni, Mo and Fe were effectively treated as being inert in the simulation (the inherent assumption being that any oxides of these elements forming at the tuyeres would immediately be reduced by more reactive Si, Mn and Cr).

Actual plant data is presented in table 8.1 below and is shown on figure 8.1 as indicated.

It will be seen from figure 8.1 that the simulation did not run the full time of just over 20 minutes. It was terminated after 16 minutes when the upper temperature limit that had been specified was exceeded.

TABLE 8.1: Plant data for 4:1 blowing step of Heat #79447

		Start of Blow	After 2 min Blowing	After 14,6 min Blowing	After 20,4 min Blowing
Metal mass	Kg	54590	N/A	N/A	N/A
Temperature	°C	1480	1920	1630	1683
Carbon	%	2,095	2,075	N/A	0,997
Silicon	%	0,357	0,198	N/A	0,060
Manganese	%	0,997	0,974	N/A	0,904
Molybdenum	%	1,945	1,917	N/A	1,934
Chromium	%	18,55	18,02	N/A	18,55
Nickel	%	7,33	7,23	N/A	7,46
Iron	%	68,64	68,43	N/A	69,78
Sulphur	%	0,014	0,011	N/A	0,016
Phosphorus	%	0,024	0,022	N/A	0,024
Nitrogen	%	0,065	0,098	N/A	0,076
Oxygen	%	0,016	0,006	N/A	0,032

Figure 8.2 is for a 1:1 (ie. $30m^3O_2min^{-1}:30m^3Ar\ min^{-1}$) blowing ratio. An initial 5mm diameter bubble at the tuyeres was selected and Si, Mo and Fe were not participating elements.

The discontinuity after 10 minutes blowing time represents an interuption in the decarburisation step when 1600 Kg mild steel scrap was charged as a coolant.

Actual plant data is presented in table 8.2 below and is shown on figure 8.2 as indicated.

TABLE 8.2: Plant data for 1:1 blowing step of Heat #70447

		Start of Blow	After 13,4 min Blowing
Metal mass	Kg	54500*	N/A
Temperature	°C	1635	1714
Carbon	%	0,452	0,097
Silicon	%	0,021	0,035
Manganese	%	1,100	0,990
Molybdenum	%	1,899	1,898
Chromium	%	15,53	17,31
Nickel	%	7,41	7,30
Iron	%	70,18	72,26
Sulphur	%	0,016	0,014
Phosphorus	%	0,025	0,025
Nitrogen	%	0,046	0,019
Oxygen	%	0,020	0,097

Apart from a few exceptions, it is evident that the model, in its present "untuned" form, does not accurately predict the temperature and composition trajectories observed on the plant. However, in most cases, the expected trends are correct. Individual trajectories are discussed below

8.5.2 Temperature

In both simulations it is evident that the predicted rate of temperature increase was much too high compared to plant data. Possible reasons for this are the following:-

(i) The heats of solution of the various elements were considered to be small enough to be neglected. This may be an over-simplification.

(ii) The heat of formation data used applies only to the formation of oxides in their pure states. The possibility of

subsequent endothermic (or exothermic !) reactions between the various oxides and the fluxes in the slag phase have not been considered.

(iii) The linearized (with respect to temperature) heat capacities of the various metal and slag phase components may need revision.

(iv) The simplification introduced by the concept of an equivalent lining thickness and hot face surface area of the refractory lining.

Similar problems have recently been experienced by Pauw[7] and, although the model could be tuned by using empirical correction factors, further analysis is needed to identify, understand and resolve the underlying problem.

8.5.3 Carbon

In the case of the 4:1 blow simulation the predicted decarburization rate was about 20% faster than the actual decarburization rate. To a large degree this can be attributed to the calculated high temperature rise rate. Basic thermodynamic considerations, confirmed by operating plant experience, dictate that high temperatures must significantly improve decarburization efficiency.

In the case of the 1:1 blow simulation, despite the calculated bath temperatures being higher than the actual ones, the calculated decarburization rate was about 74% slower than the actual decarburization rate. This deviation could be due to one or more of a number of possible factors:-

(i) The temperature dependence of the diffusivity of carbon (and the other elements) was not taken into account. Diffusivities applicable at the somewhat arbitrary temperature of 1650°C have been used. Increasing diffusivities with increasing temperature would significantly improve the predicted decarburization rate.

(ii) The temperature dependence of activity coefficients was not taken into account except in the case of nitrogen. Data used was taken from the paper by Deb Roy et.al.[8] and Making, Shaping and Treating of Steel[9].

(iii) Interaction parameter data for calculating activity coefficients is, strictly speaking, only applicable to dilute solutions of solutes in liquid iron. For lack of alternative data, some of the interaction parameters have been applied to fairly high concentrations of some of the solutes.

The Tayare and Rining Bubble Reactor models are, in general, fairly sensitive to the [illegible] of interaction

parameter data. Any inaccuracies in this respect could be expected to have a significant effect on the overall accuracy of the AOD Model.

(iv) An *arbitrary* bubble diameter of 5mm at the tuyere level was selected. Because of the strong dependence of the decarburization rate equation on bubble and oxide particle surface areas, the selection of a smaller initial bubble diameter would have the effect of improving the kinetics of decarburization.

Conversely, in situations of an unrealistically high decarburization rate, the rate could be slowed down by choosing a larger initial bubble size.

(iv) The AOD Model, in its present form, does not take into account slag/metal reactions at the interface between the bulk liquid metal and bulk slag phases.

By the time the 1:1 blow commences, there can be expected to be a significant accumulation of reducible oxides (ie. MnO, Cr_2O_3 and some FeO) in the bulk slag phase. Some secondary decarburization can be expected to take place at the interface between the bulk metal and slag phases which has not been taken into account by the model.

(v) The decision was taken (for the sake of integrator stability during the early stages of the model development) to make the somewhat crude approximation of coupling the decarburization reaction in a bubble to the reduction of oxides in an oxide particle. This may be a serious problem.

The alternative of calculating the oxygen concentration in the bulk liquid metal would be more realistic. This would be done via an oxygen balance that takes into account the oxygen depletion rate due to the decarburization reaction and the oxygen input rates from oxides dissociating in the oxide droplet and bulk slag phases.

(vi) The Tuyere Reaction Model has not been formulated in such a manner as to allow reduction of "unstable" oxides such as NiO, MoO_3 and FeO by elements with a greater affinity for oxygen such as C, Si, Mn or Cr.

As a result, if elements such as Ni, Mo or Fe are allowed to participate in the tuyere reaction model, droplets of an oxide mixture with a very high oxygen potential are produced. This high oxygen potential causes very high decarburization rates in the Rising Bubble Reaction Zone. This in turn gives rise to unrealistically high decarburization efficiencies in all ratios.

As in the case of the Tuyere Reaction Zone, the Rising Bubble Reaction Zone does not allow for the reduction of NiO, MoO_3 or FeO by Cr or Mn simultaneously with that by C

parameter data. Any inaccuracies in this respect could be expected to have a significant effect on the overall accuracy of the AOD Model.

(iv) An arbitrary bubble diameter of 5mm at the tuyere level was selected. Because of the strong dependance of the decarburization rate equation on bubble and oxide particle surface areas, the selection of a smaller initial bubble diameter would have the effect of improving the kinetics of decarburization.

Conversely, in situations of an unrealistically high decarburization rate, the rate could be slowed down by choosing a larger initial bubble size.

(iv) The AOD Model, in its present form, does not take into account slag/metal reactions at the interface between the bulk liquid metal and bulk slag phases.

By the time the 1:1 blow commences, there can be expected to be a significant accumulation of reducible oxides (ie. MnO, Cr_2O_3 and some FeO) in the bulk slag phase. Some secondary decarburization can be expected to take place at the interface between the bulk metal and slag phases which has not been taken into account by the model.

(v) The decision was taken (for the sake of integrator stability during the early stages of the model development) to make the somewhat crude approximation of coupling the decarburization reaction in a bubble to the reduction of oxides in an oxide particle. This may be a serious problem.

The alternative of calculating the oxygen concentration in the bulk liquid metal would be more realistic. This would be done via an oxygen balance that takes into account the oxygen depletion rate due to the decarburization reaction and the oxygen input rates from oxides dissociating in the oxide droplet and bulk slag phases.

(vi) The Tuyere Reaction Model has not been formulated in such a manner as to allow reduction of "unstable" oxides such as NiO, MoO_3 and FeO by elements with a greater affinity for oxygen such as C, Si, Mn or Cr.

As a result, if elements such as Ni, Mo or Fe are allowed to participate in the tuyere reaction model, droplets of an oxide mixture with a very high oxygen potential are produced. This high oxygen potential causes very high decarburization rates in the Rising Bubble Reaction Zone. This in turn gives rise to unrealistically high decarburization efficiencies in all ratios.

As in the case of the Tuyere Reaction Zone, the Rising Bubble Reaction Zone does not allow for the reduction of NiO, MoO_3 or FeO by Cr or Mn simultaneously with that by C

and Si.

The only way to reduce the oxygen potential of the oxide droplet phase entering the Rising Bubble Reaction Zone is to artificially completely suppress the participation of Si, Mn and Fe in the tuyere reaction zone model. The basis of this is the possibly unrealistic assumption that if these oxides are initially formed, they are immediately virtually completely reduced by the elements (such as Si, Mn and Cr) with a much greater thermodynamic affinity for oxygen.

The ideal model would be one that allows a certain degree of back reduction of MnO etc. This would allow the entry, into the rising bubble reaction zone, of oxide particles with limited but realistic levels of these oxides.

(vii) The model assumes that only one oxide droplet is produced per bubble leaving the tuyere reaction zone. The increased surface area effect of allowing a number of droplets to be produced per bubble would increase the decarburization rate.

Conversely, if oxide particles were allowed to coalesce, the decarburization rate would be reduced.

8.5.4 Silicon

In both cases, the silicon trajectory of the liquid metal followed the expected trend; an initial high desiliconization rate gradually tapering off as the silicon content of the metal became progressively depleted.

In figure 8.1 the actual desiliconization rate was faster than the calculated rate during the first two minutes of blowing time. Thereafter, the calculated rate appears to have overtaken the actual rate. In both simulations the calculated degree of desiliconization was higher than that actually observed by the end of the respective blow.

It should however be pointed out that the final %Si as analysed should be treated with some caution as the analytical technique used (X-Ray fluorescence) cannot distinguish between dissolved Si and Si in the form of SiO_2 containing inclusions suspended in the sample. At the low %Si levels under consideration, the background "noise" represented by minute suspended particles of SiO_2 containing material may be significant.

In general, many of the concepts discussed in section 8.5.3 are equally applicable in the case of silicon. Much tuning and/or modification of the models may be needed before really accurate predictions are achieved.

8.5.5 Manganese

In both figures 8.1 and 8.2, the calculated manganese trajectories of the liquid metal bore little resemblance to those observed in the plant scale heat. The main reason for the apparent "lack of reactivity" of manganese is suspected to lie in the choice of interaction parameters used for calculating the manganese activity coefficient.

Again, many of the concepts discussed in section 8.5.3 may also be relevant.

8.5.6 Chromium

The calculated chromium trajectory in figure 8.1 shows an initial increase followed by a levelling off of the chromium concentration in the liquid metal. Although chromium was being oxidised, there was a nett concentration effect because of the comparatively high removal rates of carbon and silicon from the bath. As the removal rates of these latter two elements decreased, the chromium removal rate increased to the extent that the concentration effect ceased.

There was an apparent very high initial increase in the actual chromium content in the first two minutes of the blow. This could have been, in part, due to the selection of the initial chromium analysis (input into the model) which may have been lower than the true value to start with. There was a wide scatter in the analyses (range 18,17% to 19,04%) of a number of samples taken at the same time and consequently an average value was used.

The other alternative could have been the carry-over of a high Cr_2O_3 content slag from the arc furnace which was subsequently partially reduced by carbon and silicon in a slag/metal reaction during the early stages of the blow.

The actual chromium level of the bath then dropped off from 18,94% to 18,55% during the subsequent twenty minutes of blowing time. Since the actual decarburization rate was not as fast as the predicted rate, the chromium removal rate was probably sufficient to drop the chromium concentration in the liquid metal. Again however, uncertainty in the average final analysis cannot be ignored altogether.

In the case of figure 8.2, the difference of 0,43% between the actual (17,31%) and predicted final (16,88%) chromium concentrations was largely due to the model predicting a poorer carbon removal efficiency than what was observed in practice. Thus the comments of section 8.5.3 above apply.

8.5.7 Nickel, Molybdenum and Iron

The comments of section 8.5.3(vi) above apply.

8.5.8 Nitrogen

In figure 8.1 the actual and predicted nitrogen concentration trajectories did not bear any resemblance to one another. This was because pure nitrogen alone was used to keep the tuyeres clear for the short period between turning off the oxygen flow and turning down the vessel for sampling and temperature measurement. These brief blowing periods with pure nitrogen were not taken into account in the simulation.

This problem can be resolved by the development of the subroutines needed to cater for the case of blowing an inert gas without oxygen.

In the case of figure 8.2 where the turn-down gas was argon, the predicted and actual final nitrogen concentrations were in reasonable agreement, being about 0,015% and 0,019% respectively

8.5.9 Oxygen

The need for an oxygen balance to determine the oxygen concentration of the bulk liquid metal phase has been discussed in section 8.5.3(v) above.

8.5.10 Computation Time

By the use of variable step length integrators[8,9], the problem of instability that plagued the early stages of the model development has been resolved. However this has been at a high cost in respect of computation time. In its present form when running the compiled and linked FORTRAN 77 source code on an 8MHz IBM compatible PC, the model is substantially slower than real process time.

However the first objective of any future work must remain the modification and tuning of the various model components so that it can accurately predict process temperature and composition trajectories.

9 CONCLUSIONS

9.1 Summary and conclusions

A model has been developed to describe the AOD decarburization process at Middelburg Steel and Alloys.

The model assumes that metal phase elements diffuse from the bulk metal through a metal phase boundary layer surrounding a rising bubble. They react with oxygen in the bubble at the metal/gas interface to form an oxide slag. This continues until the oxygen has been depleted.

The oxide slag is assumed to disengage from the bubble as an oxide droplet. The bubble and oxide droplet rise up together in a plume of bubbles and entrained oxide droplets and liquid metal. As they rise up, oxygen and carbon diffuse from the bulk metal through the metal phase boundary layer surrounding a bubble. They react at the gas/metal interface to form CO. Oxygen for the decarburization reaction is supplied by the dissociation of oxides in the oxide droplet.

Partially reduced oxide droplets are captured by the bulk slag phase floating on top of the bulk liquid metal. Further reactions at the bulk metal/slag interface are not considered at this stage although they are known to occur. The composition changes occuring with respect to time in the bulk metal and slag phases are taken into account with differential mass balances.

The change of the bath temperature with respect to time is taken into account with a differential heat balance. The latter incorporates a model for the unsteady state heat transfer through the vessel refractory lining.

The bath temperature and composition trajectories are determined by the simultaneous integration of the differential heat and mass balances.

Although most of the predicted trajectories follow the expected trend, they are not sufficiently accurate for the model to be used as a "live" process simulator in its present stage of development. Substantial tuning and modification of the component models are still required.

In particular, the computed temperature trajectory was found to rise too quickly compared to the actual plant unit.

At high carbon concentrations (>1%) excessively high carbon removal rates were predicted, particularly if elements such as nickel, molybdenum or iron were allowed to participate.

At lower carbon concentrations (<0,5%) the predicted carbon concentration trajectory indicated a lower than actually observed carbon removal rate.

The calculated silicon concentration trajectories were not too dissimilar from observed plant data.

The calculated manganese concentration trajectories showed little concentration change with respect to time. They deviated considerably from the plant data, indicating the possible use of incorrect interaction parameter data for calculating activity coefficients.

The calculated chromium concentration trajectories reflected the carbon removal rates in that a high carbon removal rate gave rise to a low chromium removal rate and vice versa.

The predicted nitrogen concentration trajectory looked promising in the case where nitrogen was not used as the inert gas for keeping the tuyeres unblocked during vessel turn-down operations. However a model to cater for blowing either inert gas in the absence of oxygen is needed.

It was concluded that the Rising Bubble Reaction Zone and AOD Models needed to be modified to incorporate an overall oxygen balance for the bulk liquid metal phase. The approach of directly coupling the reduction of an oxide particle with the decarburization reaction at the metal/gas interface of a bubble sidestepped the need to calculate the oxygen concentration in the bulk liquid phase directly. Whilst contributing to integrator stability, it was suspected of introducing other problems adversely affecting the accuracy of the model.

The likely reasons for observed deviations between predicted and actual results, together with possible solutions were discussed in some detail in the preceeding chapter. The solutions have been summarized in section 9.2

Despite the lack of accurate composition and temperature trajectory predictions by the model in its present "untuned" state, it provides the framework for potentially significant improvement, both by "parameter tuning", and by modifying and improving some of the component models.

The model provides a useful basis for the understanding of some of the fundamental physical and chemical principles underlying the AOD process.

9.2 Recommendations for Future Work

(i) Temperature dependent diffusion data needs to be built in to the model.

(ii) The Rising Bubble Reaction and Unified AOD models need to

be modified to allow for an oxygen balance for the bulk liquid metal. Thus the decarburization reaction at the metal/gas interface of a bubble could be de-coupled from the reduction of an oxide particle.

(iii) The heat balance needs to be investigated in depth and, where applicable, new or alternative data needs to be used. This includes taking into consideration heats of solution of metal phase elements and heats of formation of possible complex bulk slag phase compounds.

(iv) The concept of an equivalent lining thickness (used to transform the complex problem of unsteady state heat transfer through an irregularly shaped refractory lining into a simpler one involving unsteady state heat transfer through a parallel sided plate) may be an over-simplification in need of revision.

(v) A model catering for the reactions taking place at the bulk metal/slag interface needs to be developed and incorporated into the model.

(vi) The Tuyere Reaction Zone model needs to be modified to allow for the reduction of oxides such as NiO, MnO_2 and FeO by reactive elements such as C, Si, Mn and Cr.

(vii) The Rising Bubble Reaction Zone model needs to be modified to allow for the reduction of oxides such as NiO, MnO_2 and FeO by elements such as Mn and Cr in addition to C and Si.

(viii) The interaction parameters used for calculating activity coefficients need to be revised and better data used if available.

(ix) A model for inert gas stirring in the absence of oxygen needs to be developed.

(x) The models, in their present or modified forms, need to be tuned to fit observed plant data.

(xi) The immediate objective of the foregoing must be to develop the model to the state that it can accurately predict operating plant temperature and composition trajectories under all normally encountered plant circumstances. Thereafter the software needs to be refined to minimize computation time to a level that it is significantly less than real process time. Failing that, alternative hardware needs to be investigated.

(xii) Once a fast and accurate simulator is available, the development of an on-line process optimization and control system could proceed. Such a system would have to, amongst other things, be able to drive the oxygen:inert gas ratio setpoint on a continuous optimum basis. It would have to interface with existing plant measuring and control

hardware, as well as existing charge correction hardware and software.

APPENDIX A

DERIVATION OF THE DECARBURIZATION RATE EQUATION USED IN THE RISING BUBBLE REACTION MODEL

A.1 Introduction

In the Rising Bubble Reaction Model it is assumed that the rate of the decarburization reaction depends on the rate of diffusion of oxygen and carbon through the metal phase boundary layer surrounding the bubbles as they rise through the liquid metal. Because the decarburization reaction is coupled to the dissociation of oxides, the decarburization reaction rate is also dependent on the rate of diffusion of oxygen through the metal phase boundary layer surrounding the oxide particles.

The concentration gradients of carbon monoxide, carbon and oxygen are schematically represented in Figure A1 where:-

P_{CO} = Partial pressure of carbon monoxide in the bulk gas phase of a bubble.

P_{CO_i} = Partial pressure of carbon monoxide in the gas phase of the gas/metal interface of a bubble.

$C_{i,c}$ = Concentration of carbon in the metal phase of the metal/gas interface of a bubble.

$C_{b,c}$ = Concentration of carbon in the bulk metal phase.

$C_{i,o}$ = Concentration of oxygen in the metal phase of the metal/gas interface of a bubble.

$C_{b,o}$ = Concentration of oxygen in the bulk metal phase associated with the plume of bubbles.

$C_{ox,o}$ = Concentration of oxygen in the metal phase at the surface of an oxide particle.

APPENDIX A

DERIVATION OF THE DECARBURIZATION RATE EQUATION USED IN THE RISING BUBBLE REACTION MODEL

A.1 Introduction

In the Rising Bubble Reaction Model it is assumed that the rate of the decarburization reaction depends on the rate of diffusion of oxygen and carbon through the metal phase boundary layer surrounding the bubbles as they rise through the liquid metal. Because the decarburization reaction is coupled to the dissociation of oxides, the decarburization reaction rate is also dependant on the rate of diffusion of oxygen through the metal phase boundary layer surrounding the oxide particles.

The concentration gradients of carbon monoxide, carbon and oxygen are schematically represented in Figure A1 where:-

P_{CO} = Partial pressure of carbon monoxide in the bulk gas phase of a bubble.

P_{CO_i} = Partial pressure of carbon monoxide in the gas phase of the gas/metal interface of a bubble.

$C_{i,c}$ = Concentration of carbon in the metal phase of the metal/gas interface of a bubble.

$C_{b,c}$ = Concentration of carbon in the bulk metal phase.

$C_{i,o}$ = Concentration of oxygen in the metal phase of the metal/gas interface of a bubble.

C_r = Concentration of oxygen in the bulk metal phase associated with the plume of bubbles.

C_{ox} = Concentration of oxygen in the metal phase at the surface of an oxide particle.

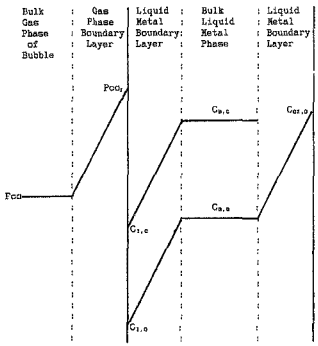


Figure A1: Schematic representation of concentration gradients in the boundary layers at the metal/gas interface of a bubble and the metal/oxide interface of an oxide particle

A.2 Derivation of the Decarburization Rate Equation

Considering the stoichiometry of the decarburization reaction:-

[C] + [O] -> CO (A.1)

it is evident that the fluxes of carbon, oxygen and CO to and from the metal/gas interface are equal.

Thus:-

$J(h) = J_C(h) = k_{MM,C}(h)*(C_{B,C}-C_{I,C}(h))$ (A.2)

$J(h) = J_O(h) = k_{MM,O}(h)*(C_{B,O}-C_{I,O}(h))$ (A.3)

$J(h) = J_{CO}(h) = k_R*(C_{I,C}(h)*C_{I,O}(h)-P_{CO_I}(h)/K^*)$ (A.4)

where..

$J(h)$ = Flux of C, O and CO at bubble height h above the tuyeres.

$k_{MM,C}(h)$ = Mass transfer coefficient for carbon through the metal phase boundary layer surrounding a bubble.

$k_{MM,O}(h)$ = Mass transfer coefficient for oxygen through the metal phase boundary layer surrounding a bubble.

k_R = Rate constant for the reaction (A.1).

K^* = Equilibrium constant for the reaction:-

[C] + [O] <=> CO (A.5)

at the metal/gas interface.

Thus:-

$K^* = P_{CO_I}(h)/(C_{I,C}(h)*C_{I,O}(h))$ (A.6)

where $C_{I,C}(h)$ and $C_{I,O}(h)$ are the concentrations of carbon and oxygen in equilibrium with carbon monoxide at the metal/gas interface.

The following assumptions are made:-

(i) $k_R >> k_{MM,C}(h)$ and $k_{MM,O}(h)$

(ii) the rate of reaction between C and O at the interface is extremely fast. Thus the equilibrium indicated by equation A.5 is assumed to exist at the interface.
Thus $C_{i,c}(h) \rightarrow C_{g,c}(h)$ and $C_{i,o}(h) \rightarrow C_{g,o}(h)$.

(iii) the mass transfer of CO through the gas phase boundary layer is not rate limiting.

Thus:-

$$P_{CO_i}(h) = P_{CO}(h) \qquad (A.7)$$

Therefore equation A.4 becomes:-

$$J(h) = J_{CO}(h) = k_g * (C_{i,c}(h) * C_{i,o}(h) - P_{CO}(h)/K^*) \qquad (A.8)$$

From item (ii) above and equation A.7:-

$$C_{i,c}(h) * C_{i,o}(h) = P_{CO_i}(h)/K^* = P_{CO}(h)/K^* \qquad (A.9)$$

Re-arranging A.2:-

$$J(h) = k_{MUS,c}(h) * C_{B,c} - k_{MUS,c}(h) * C_{i,c}(h) \qquad (A.10)$$

$$\Rightarrow C_{i,c}(h) = (k_{MUS,c}(h) * C_{B,c} - J(h))/k_{MUS,c}(h) \qquad (A.11)$$

Similarly:-

$$C_{i,o}(h) = (k_{MUS,o}(h) * C_{B,o} - J(h))/k_{MUS,o}(h) \qquad (A.12)$$

Multiplying A.11 and A.12:-

$$C_{i,c}(h) * C_{i,o}(h) = (k_{MUS,c}(h) * C_{B,c} - J(h)) * (k_{MUS,o}(h) * C_{B,o} - J(h)) / (k_{MUS,c}(h) * k_{MUS,o}(h)) \qquad (A.13)$$

Combining A.9 with A.13 gives:-

$$P_{CO}(h)/K^* = (k_{MUS,c}(h) * C_{B,c} - J(h)) * (k_{MUS,o}(h) * C_{B,o} - J(h)) / (k_{MUS,c}(h) * k_{MUS,o}(h)) \qquad (A.14)$$

$$\Rightarrow P_{CO}(h)/K^* = (-J(h) * k_{MUS,c}(h) * C_{B,c} + k_{MUS,c}(h) * k_{MUS,o}(h) * C_{B,o} * C_{B,c} - J(h) * k_{MUS,c}(h) * C_{B,o} + J(h)^2) / (k_{MUS,c}(h) * k_{MUS,o}(h))$$

$$\Rightarrow P_{CO}(h)/K^* = (J(h)^2 + J(h) * (-k_{MUS,c}(h) * C_{B,c} - k_{MUS,o}(h) * C_{B,o}) + k_{MUS,c}(h) * k_{MUS,o}(h) * C_{B,c} * C_{B,o}) / (k_{MUS,c}(h) * k_{MUS,o}(h))$$

$$\Rightarrow \emptyset = J(h)^2*J(h)*(-k_{mtc,c}*C_{g,c}-k_{mto,c}(h)*C_{g,o}) + k_{g-w,c}(h)*k_{mtb,c}(h)*C_{b,c}*C_{g,c}-k_{mto,c}(h)*k_{mtb,c}(l.)*Pco(h)/K^4 \quad (A.15)$$

Now $J(h) = \dot{r}_c(h)/(n_{mto}*A_{mto}(h))$ (A.16)

where:-

$\dot{r}_c(h)$ is the decarburization rate at a height h above the tuyeres;

n_{mto} is the flowrate of bubbles through the horizontal plane height h above the tuyeres;

$A_{mto}(h)$ is the surface area of a bubble at a height h above the tuyeree.

Also:-

$$\dot{r}_c(h) = n_{mto}*A_{ox}(h)*k_{ox,c}(h)*(C_{ox,c}(h)-C_{g,o}) \quad (A.17)$$

where:-

$A_{ox}(h)$ is the surface area of an oxide particle at a height h above the tuyeres;

$k_{ox,c}(h)$ is the mass transfer coefficient for the diffusion of oxygen through the metal phase boundary layer surrounding an oxide particle.

$$\Rightarrow \dot{r}_c(h)/(n_{mto}*A_{ox}(h)*k_{ox,c}(h)) = C_{ox,c}(h)-C_{g,c}$$

$$\Rightarrow C_{g,c} = C_{ox,c}(h)-\dot{r}_c(h)/(n_{mto}*A_{ox}(h)*k_{ox,c}(h)) \quad (A.18)$$

Therefore, substituting equations A.16 and A.18 for $J(h)$ and $C_{g,c}$ in equation A.15 we get:-

$$\emptyset = (\dot{r}_c(h)/(n_{mto}*A_{mto}(h)))^2*(\dot{r}_c(h)/(n_{mto}*A_{mto}(h))) *(-k_{mtw,c}(h)*k_{mtb,c}(h)-k_{gw,c}(h)*(C_{ox,c}(h)-\dot{r}_c(h)/(n_{mto}*A_{ox}(h)*k_{ox,c}(h)))) +k_{mto,c}(h)*k_{mtw,c}(h)*C_{g,c}*(C_{ox,c}(h)-\dot{r}_c(h)/(n_{mto}*A_{ox}(h)*k_{ox,c}(h))) -k_{mto,c}(h)*k_{mtb,c}(h)*Pco(h)/K^4 \quad (A.19)$$

This can be simplified to give a quadratic equation in $\dot{r}_c(h)$ of the form:-

$$\emptyset = A*\dot{r}_c(h)^2+B*\dot{r}_c(h)+C \quad (A.17)$$

where:-

$$A = 1/(n_{BUS}*A_{MOS}(h))^2*k_{BUS,S}(h)/(n_{MOS}^2*A_{MOS}(h)*A_{OX}(h)*K_{OX,S}(h)) \quad (A.18)$$

$$B = -((K_{BUS,S}(h)*C_{B,S}+k_{BUS,S}(h)*C_{OX,S}(h))/(n_{MOS}*A_{MOS}(h)) + k_{MOS,S}(h)*K_{BUS,S}(h)*C_{B,S}/(n_{MOS}*A_{OX}(h)*K_{OX,S}(h))) \quad (A.19)$$

$$C = k_{BUS,S}(h)*k_{BUS,S}(h)*(C_{B,S}*C_{OX,S}(h)-P_{CG}(h)/K^*) \quad (A.20)$$

Therefore:-

$$I_{TC}(h) = (-B \pm (B^2-4*A*C)^{1/2})/(2*A) \quad (A.21)$$

However, only one root is applicable.

Now:-

$$I_{TC}(h) = 0 \quad (A.22)$$

when:-

$$C_{B,S}*C_{OX,S}(h)-P_{CG}(h)/K^* = 0 \text{ (ie when C = 0)} \quad (A.23)$$

$$\Rightarrow 0 = (-B \pm (B^2)^{1/2})/(2*A) \quad (A.24)$$

Since -B and $(B^2)^{1/2}$ are both positive quantities, the real root of equation A.17 is given by inspection:-

$$I_{TC}(h) = (-B-(B^2-4*A*C)^{1/2})/(2*A) \quad (A.25)$$

DERIVATION OF THE EQUILIBRIUM CONSTANT USED IN THE DECARBURIZATION RATE EQUATION

For the equilibrium reactions:-

$C + 1/2\ O_2 \Leftrightarrow CO \qquad \Delta G^o = -26760-20,98*T$ cal/gmol (B.1)

$[\%C] \Leftrightarrow C \qquad \Delta G^o = -5100+10,0*T$ cal/gmol (B.2)

$[\%O] \Leftrightarrow 1/2\ O_2 \qquad \Delta G^o = 28000+0,69*T$ cal/gmol (B.3)

Therefore, by adding equations B.1 to B.3 inclusive:-

$[\%C] + [\%O] \Leftrightarrow CO \qquad \Delta G^o = -3860-10,29*T$ cal/gmol (B.4.1)
$= -16150-43,05*T$ kJ/kgmol (B.4.2)

For the equilibrium between carbon monoxide in the gas phase and carbon and oxygen dissolved (1% standard states) in liquid iron:-

$[\%C] + [\%O] \Leftrightarrow CO$ (B.5)

the equilibrium constant K is given by:-

$K = P_{co}/([\%C]*f_c*[\%O]*f_o)$ (B.6)

where:-

[%C] = Percent carbon dissolved in liquid iron.

[%O] = Percent oxygen dissolved in liquid iron.

f_c = Activity coefficient for carbon.

f_o = Activity coefficient for oxygen.

The calculation of the activity coefficients for carbon and oxygen is presented in appendix C.

Now, from equation B.6:-

$[\%C]*[\%O] = P_{co}/(f_c*f_o*K)$ (B.7)

For the equilibrium at the metal/gas interface as discussed in the preceding section, equation B.7 can be expressed as:-

$$[\%C_i][\%O_i] = P_{co}/(f_c * f_o * K) \qquad (B.8)$$

where $[\%C_i]$ *and* $[\%O_i]$ *are the weight percent concentrations of* carbon and oxygen in the metal phase at the metal/gas interface of a bubble.

K is calculated, as a function of temperature, from the free energy given by equation B.4.2:-

$$K = \exp((16150+43,05*T)/(R*T)) \qquad (B.9)$$

Now the molar concentrations of carbon and oxygen at the interface are related to the weight percent concentrations as follows:-:-

$$C_{i,c} = \rho[\%C_i]/1200 \text{ kgmol/m}^3 \qquad (B.10)$$

and:-

$$C_{i,o} = \rho[\%O_i]/1600 \text{ kgmol/m}^3 \qquad (B.11)$$

where ρ is the liquid metal density (kg/m³).

Combining equations B.8, B.10 and B.11:-

$$1200*(C_{i,c}/\rho)*1600*(C_{i,o}/\rho) = P_{co}/(f_c*f_o*K)$$

$$\Rightarrow C_{i,c}*C_{i,o} = P_{co}*\rho^2/(f_c*f_o*K*1,9226)$$

$$\Rightarrow C_{i,c}*C_{i,o} = P_{co}/K^* \qquad (B.12)$$

where:-

$$K^* = f_c*f_o*K*1,9226/\rho^2 \qquad (B.13)$$

Substituting equation B.9 for K in equation B.13:-

$$K^* = \rho^2\exp((16150+43,05*T)/(RT))*f_c*f_o*1,9226/\rho^2 \qquad (B.14)$$

Now, the equilibrium constant K_{co} as defined by equation 1.26 in section 4.2.1 of the rising bubble reaction model is:-

$$K_{co} = 1/K^* \qquad (B.15)$$

Therefore:-

$K_{co} = p^2/(Hxp((15150+43,05xT_s)/(RxT_s))xf_cxf_ax1,92E5)$ (B.16)

where the liquid metal temperature T_s is equivalent to T in equation B.14 above.

CALCULATION OF ACTIVITY COEFFICIENTS

Since liquid stainless steel is a complex multi-component solution, it is necessary to take into account the interaction effects of the various elements on the activities of individual elements.

The Henrian activity coefficient for the j'th element is given by:-

$$f_j = 10^{**}\left(\sum_{k=1}^{n}(\%M_k e_{j,k})\right) \qquad (C.1)$$

where:-

$e_{j,k}$ is the first order parameter for the interaction of element k on element j in liquid iron.

$\%M_k$ is the weight percent of the k'th element in the liquid metal.

There appears to be some discrepancy between the interaction parameters quoted by different authors. Values for $e_{j,k}$ listed in the paper by Deb Roy et. al.* and are presented in Table C.1 below:-

	k	1	2	3	4	6	14
J	Element	C	Si	Mn	Cr	Ni	O
1	C	+0,19	+0,088	-0,002	-0,02	+0,012	-0,24
2	Si	+0,13	+0,11	0	0	+0,005	-0,23
3	Mn	-0,009	0	0	0	0	-0,063
4	Cr	-0,103	0	0	-0,0003	0	-0,133
14	O	-0,45	-0,131	-0,021	-0,04	+0,006	-0,2

Table C.1: First Order Henrian Interaction Parameters (ex Deb Roy et.al.*)

Values of $e_{j,k}$ listed in the paper by Sigworth and Elliott[1] are presented in Table C.2. Values that are temperature dependent are presented in the form:-

$$e_{j,k} = A + B/T \qquad (C.2)$$

Note that interaction parameters for which no data is reported in the reference are taken to be zero (ie. ideal Henrian behaviour is assumed).

	k	1	2	3	4	5	6	7
j	Element	C	Si	Mn	Cr	Mo	Ni	Fe
1	C	+0,0561 +135/T	-0,066 +162/T	+0,0079	+0,110	-0,0083	0	0
2	Si	-0,023 +330/T	+0,069 +34,5/T	+0,010	+0,090	0	0	0
3	Mn	-0,070	0	0	0	0	0	0
4	Cr	-0,120	-0,0043	0	-0,0003	+0,0018	+0,0002	0
5	Mo	-0,097	0	0	-0,0003	0	0	0
6	Ni	-0,042	+0,0027	-0,0023	-0,0003	0	+0,0009	0
14	O	-0,450	-0,131	-0,021	-0,040	+0,0035	0,006	0

Table C.2: First Order Henrian Interaction Parameters (ex Sigworth and Elliott[1])

	k	6	9	10	11	12	13	14
j	Element	Ti	Al	Cu	S	P	N	O
1	C	0	+0,043	+0,016	+0,046	+0,051	+0,110	-0,340
2	Si	0	+0,056	+0,014	+0,056	+0,110	+0,090	-0,230
3	Mn	0	0	0	-0,048	-0,0035	-0,091	-0,063
4	Cr	+0,059	0	+0,016	+0,062 -153/T	-0,053	-0,190	-0,140
5	Mo	0	0	0	-0,0005	0	-0,100	-0,0007
6	Ni	0	0	0	-0,0037	-0,0035	+0,010	+0,010
14	O	-0,600	+7,15-20000/T	-0,013	-0,133	+0,070	+0,057	+0,734 -1750/T

Table C.2 (continued): First Order Henrian Interaction Parameters

In the case of nitrogen, the Henrian activity coefficient f_N is given by[7]:-

$$f_N = 10^{x((3280/T)-0,75)x(\sum_{j=1}^{n}(\%M_j e_{N,j}))+0,0001\%\%Cr\%\%2} \qquad (C.3)$$

where:-

$e_{N,j}$ is the first order parameter for the interaction of element j on nitrogen in liquid iron. Values for $e_{N,j}$ are presented in Table C.3 on the following page.

j	Element	First Order Interaction Parameter $e_{N,j}$	Second Order Interaction Parameter $R_{N,j}$
1	C	+0,13	
2	Si	+0,047	
3	Mn	-0,023	
4	Cr	-0,047	+0,00017
5	Mo	-0,011	
6	Ni	+0,01	
7	Fe	0	
8	Ti	-0,53	
9	Al	-0,028	
10	Cu	+0,009	
11	S	+0,007	
12	P	+0,045	
13	W	0	
14	O	+0,05	
	As	+0,018	
	B	+0,094	
	Co	+0,011	
	Nb	-0,06	
	Sb	+0,0066	
	Se	+0,006	
	Sn	+0,007	
	Ta	-0,032	
	Te	+0,07	
	V	-0,093	
	W	-0,0015	
	Zr	-0,63	

Table C.9: Interaction Parameters for Nitrogen in Liquid Iron (data taken from the paper by S K Mahlman[14])

REFERENCES

1 I Matsuki et. al. : A Decarburization Reaction Model for the Optimum Operation in AOD Process, Proc. Second International AOD Conference, 16-17 September 1982, San Francisco, CA.

2 T Tohge, T Watanabe : Analysis of Decarburization Reaction in AOD by Mathematical Model, 34-3, p1384, Proc. 7th ICVM, 1982, Tokyo, Japan.

3 T Tohge : UK Patent Application GB 2136830 A 21 March 1983.

4 R J Fruehan : Reaction Model for the AOD Process, p153, Iron Making and Steelmaking, 1976, No 3.

5 J Szekely, N J Themelis : Rate Phenomena in Process Metallurgy, p427-429, Wiley-Interscience, 1971.

6 O Levenspiel : Chemical Reaction Engineering, 2nd Edit., p412, John Wiley and Sons, 1972.

7 United States Steel : The Making, Shaping and Treating of Steel, 9th Edit., p616, 1971.

8 J Szekely, N J Themelis : Rate Phenomena in Process Metallurgy, p[illegible] Wiley-Interscience, 1971.

9 T Deb Roy, D G C Robertson : Mathematical Model for Stainless Steelmaking [illegible], Vol 5, p198, Ironmaking and Steelmaking, 1978, No 5.

10 S K Mahlman : The Use of Nitrogen in Argon Oxygen Decarburization, Confidential Communication, Union Carbide Corporation, November 1977.

REFERENCES

1	I Matsuki et. al.	: A Decarburization Reaction Model for the Optimum Operation in AOD Process, Proc. Second International AOD Conference, 15-17 September 1980, San Francisco, CA.
2	T Tohge, T Watanabe	: Analysis of Decarburization Reaction in AOD by Mathematical Model, 34-3, p1364, Proc. 7th ICVM, 1982, Tokyo, Japan.
3	T Tohge	: UK Patent Application GB 2136830 A 21 March 1983.
4	R J Fruehan	: Reaction Model for the AOD Process, p153, Iron Making and Steelmaking, 1976, No 3.
5	J Szekely, N J Themelis	: Rate Phenomena in Process Metallurgy, p427-429, Wiley-Interscience, 1971.
6	O Levenspiel	: Chemical Reaction Engineering, 2nd Edit., p413, John Wiley and Sons, 1972.
7	United States Steel	: The Making, Shaping and Treating of Steel, 9th Edit., p330, 1971.
8	J Szekely, N J Themelis	: Rate Phenomena in Process Metallurgy, p689, Wiley-Interscience, 1971.
9	T Deb Roy, D G C Robertson	: Mathematical Model for Stainless Steelmaking: Parts 1 and 2, p198, Ironmaking and Steelmaking, 1976, No 5.
10	S K Kehlman	: The Use of Nitrogen in Argon Oxygen Decarburization, Confidential Communication, Union Carbide Corporation, November 1977.

11 G K Sigworth, J F Elliot : The Thermodynamics of Liquid Dilute Iron Alloys, Metal Science, 1974, Vol. 8.

12 J C Henry : Private communication, Refractory *Superintendent*, NUKA, 1986.

13 Eric A Brandes - Editor : Smithell's Metals Reference Book, 6th Edition.

14 G H Geigner, D R Poirier : Transport Phenomena in Metallurgy, Addison-Wesley, 1973.

15 J Szekely, S Asai : Decarburization of Stainless Steel: Part I. A Mathematical Model for Laboratory Scale Results, Metallurgical Transactions, Vol. 5, March 1974.

16 J Szekely, S Asai : Decarburization of Stainless Steel: Part II. Mathematical Model and a Process optimization for *Industrial* Scale Systems, Metallurgical Transactions, Vol. 5, March 1974.

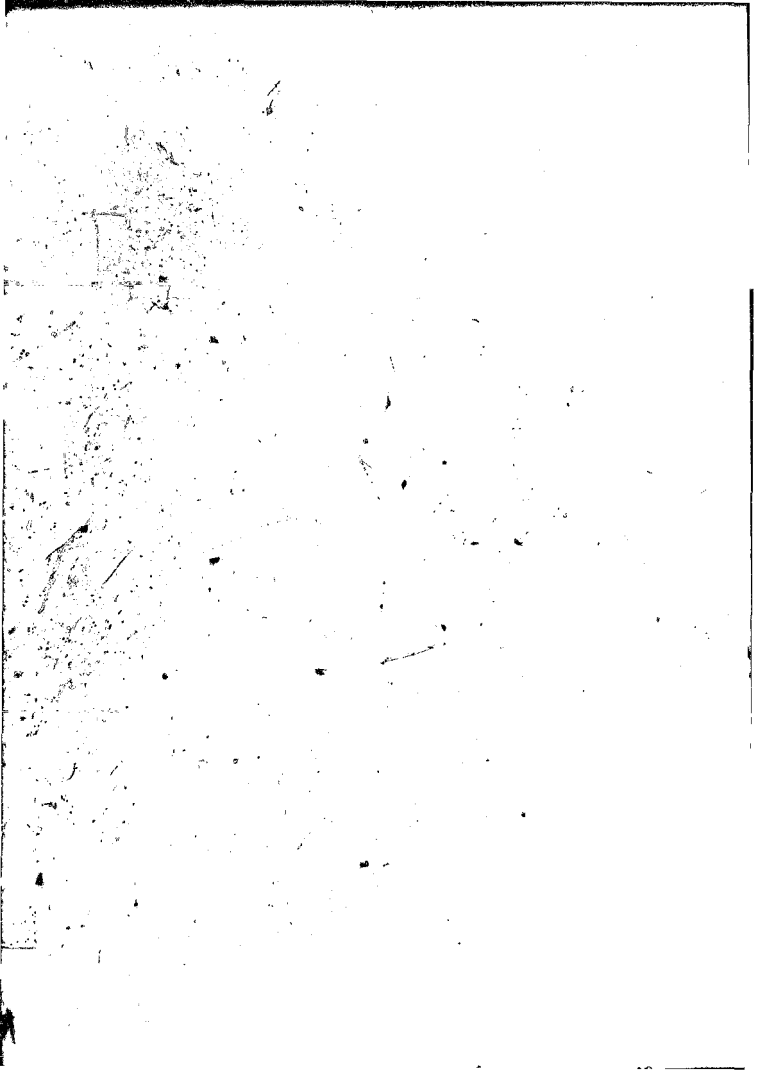
17 C G Pauw : A Kinetic-Equilibrium Model of the Argon-Oxygen Decarburization (AOD) Process, MINTEK Measurement and Control Division Confidential Communication No. C 49YM, 7 November 1985.

18 W H Press et. al. : Numerical Recipes - The Art of Scientific Computing, Cambridge University Press, 1986.

19 J van Hearden : Numeriese Oplossing van Stelsels Gewone Differensiaalvergelykings, *UKOR-319(C)*, Uranium Enrichment Corporation of South Africa, Limited, Pretoria, April 1980.

20 *Metallurgical Soc. AIMé* : Handbook on Material and Energy Balance Calculations in Metallurgical Processes, TMS-AIME Book Publishing Committee, 1979.

21 Union Carbide Corporation : A Manual for the Union Carbide Argon Oxygen Decarburization Computer Programs, Business Confidential, Union Carbide Corporation, Linde Division-Gas Products, Tarrytown, New York, May 1976.





Author Burrow Andrew Charles
Name of thesis A Model Of The Argon Oxygen Decarburization Process For Refining Stainless Stell And Alloys. 1988

PUBLISHER:
University of the Witwatersrand, Johannesburg
©2013

LEGAL NOTICES:

Copyright Notice: All materials on the University of the Witwatersrand, Johannesburg Library website are protected by South African copyright law and may not be distributed, transmitted, displayed, or otherwise published in any format, without the prior written permission of the copyright owner.

Disclaimer and Terms of Use: Provided that you maintain all copyright and other notices contained therein, you may download material (one machine readable copy and one print copy per page) for your personal and/or educational non-commercial use only.

The University of the Witwatersrand, Johannesburg, is not responsible for any errors or omissions and excludes any and all liability for any errors in or omissions from the information on the Library website.